Laboratory and numerical modelling of natural clays

A dissertation submitted for the
Degree of Master of Philosophy

David Mašín

September 2004

City University, London
School of Engineering and Mathematical Sciences
Geotechnical Engineering Research Centre

Contents

List of Tables

List of Figures

Acknowledgements

My research has been carried out at Geotechnical Engineering Research Centre at City University, London, under the supervison of Dr. Sarah Stallebrass. I would like to thank her for enabling me to perform this research project. I am indebted for her support and great leading of my research and also for her patience at that frequent occasions, when my stubborn character made the supervision very difficult.

Further, I am particularly grateful to Prof. John Atkinson, for his introduction to the equipment in the soil mechanics laboratory at City University, for pointing out important details, which make up the real soil mechanics laboratory research, and importantly, for his availability to spend his time in discussions, which were very valuable for me.

Among the other colleagues at Geotechnical Engineering Research Centre, my thanks belong to Prof. Neil Taylor, which was always prepared to provide anything from his comprehensive library and, jointly with Dr. Andrew McNamara, for their help in designing special laboratory equipment required for the research project. My special thanks go to other research students I met at City, particularly to Emilio Bilotta, for they friendship and sharing happiness and anxiety of the student live. Importantly, I would also like to thank to the technical staff, to Keith Osbourne and particularly to Lloyd Martyka, without whom the laboratory part of the research would not be possible.

Last, but not least, my thanks go to Prof. Ivo Herle, who originated my research stay at City University. I must mention numerous e–mails we exchanged during my stay at City, which supported me both scientifcally and personally.

Declaration

I grant powers of discretion to the University Librarian to allow this dissertation to be copied in whole or in part without further reference to me. This permission covers only single copies made for study purposes, subject to normal conditions of acknowledgement.

Abstract

As investigated in previous research projects at City University, the role of structure in natural clay is very significant and must be considered when natural clays are to be modelled numerically. Previous research (Ingram, 2000) has shown the significance of correctly assigned initial state before simulation of the behaviour of a geotechnical structure. Investigation of the initial state in the ground is often difficult. Therefore, the initial conditions may be best identified by simulation of the geological history of a clay stratum using a suitable constitutive model. To perform this task however, the constitutive model must be capable of predicting K_0 loading, unloading and reloading conditions and the way in which natural structure develops must be known. Fulfilling these two points is the main objective of the research reported in this dissertation.

The first part of the project concerns the development of a constitutive model, which would be capable of predicting K_0 states but also the majority of the other significant features of the behaviour of fine–grained soils. It should also be possible to enhance the model using the sensitivity framework (Cotecchia and Chandler, 2000), which enables natural structured clays to be modelled. Such a model has been developed as a modification of the three surface kinematic hardening model, developed at City University during previous research (Stallebrass, 1990). The model has been evaluated by simulating laboratory element tests on reconstituted clays, as well as finite element modelling of boundary value problems in reconstituted clay (centrifuge model tests).

To study the development of natural sedimentation structure, special laboratory equipment has been devised and specimens of clay have been prepared under controlled conditions by slow sedimentation. These specimens have been tested in well–equiped triaxial apparatuses and results compared with tests on reconstituted specimens. The influence of the pore–water chemistry has also been studied. This testing programme clarified the influence of structure on clay behaviour and the approach used for numerical modelling of the development of sedimentation structure in natural clay.

Finally, the research enabled a simulation of a geotechnical problem in natural structured clay to be performed. A significant improvement in predictions compared to predictions obtained by simpler constitutive model and by a kinematic hardeding model, not enhanced by the sensitivity framework, has been demonstrated.

Chapter 1

Introduction

This research is a part of a larger research project, which should lead to an improvement in numerical techniques for predictions of ground movements in natural clays. This project deals with natural clays with stable structure.

1.1 Background to the project

The development in numerical techniques to predict the behaviour of geotechnical structures in natural clays have in recent years emphasized the role of different aspects of soil behaviour, which were not recognised when the classical critical state soil mechanics (Roscoe and Burland, 1968) was developed. Among these belong non–linearity of soil behaviour and high small–strain stiffness (e.g., Jardine et al., 1984), the influence of recent history (Atkinson et al., 1990) and the influence of structure (Leroueil and Vaugham, 1990; Burland, 1990). Finite element simulations of well–instrumented field or model boundary value problems (among many see, e.g., Addenbrooke et al., 1997, Grant et al., 1996 and Ingram, 2000) revealed that the use of constitutive models which take these aspects into account leads to more accurate predictions, thus allowing more economic and safe design. The influence of the last aspect, structure, may be incorporated into suitable constitutive models developed for reconstituted fine–grained soils using the integrated behavioural framework for natural clays (sensitivity framework; Cotecchia and Chandler, 2000), as demonstrated by Ingram (2000) and Baudet and Stallebrass (2004) with the three surface kinematic hardening model (Stallebrass, 1990).

The advanced constitutive model, which realistically predicts the soil behaviour, must necessarily consider a number of history (state) variables, which specify the current state

of a soil element. They are, in addition to the Cauchy stress ($\boldsymbol{\sigma}$), specific volume (v), sensitivity as a measure of soil structure (S_t, defined in Chapter 6.1) and tensorial state variables specifying the influence of recent history. Any analysis of a field geotechnical problem is then complicated by the fact that values of these variables are difficult (or impossible) to measure in the ground and it is thus difficult to assign initial conditions before simulation of a boundary value problem. The way to overcome this problem is the simulation of the whole geological history of a soil deposit. Ingram (2000) has, however, demonstrated that also this approach is complicated by uncertainties. While focusing on the value of sensitivity S_t, he has shown that different scenarios for the development of structure in the soil deposit lead to different predictions of ground movements. The way in which the structure in natural clays develops is, however, usually not clear, thus it introduces uncertainties into the whole finite element simulation of a geotechnical problem.

1.2 Aims and objectives of the research

The main objectives of the project are:

- To overcome difficulties caused by uncertainty in the stress history of the soil deposit by preparing clay specimens in the laboratory such that they have a structure similar to the structure of natural clay. Differences between the behaviour of sedimented and reconstituted clay should be studied, a literature review of previous attempts to create a natural sedimentation structure in the laboratory should be performed.
- To identify shortcomings of the 3-SKH model (Stallebrass, 1990). Because one of the known shortcomings of the model are incorrect predictions of the K_0 stress states, which are important for the modelling of the geological history of the clay deposit, the 3–SKH model should be modified to improve simulations of anisotropic states (present in the ground). This modified model would be used to model natural clays using the sensitivity framework.
- To enhance the modified model using the sensitivity framework and to demonstrate its applicability to simulate laboratory experiments performed on clay with a sedimentation structure.
- Finally, to simulate a boundary value problem in natural strutured clay using the proposed constitutive model, enhanced by the sensitivity framework. The geological history and development of structure in a clay stratum should be simulated with smaler uncertainty, using results from laboratory experiments.

1.3 Description of the dissertation

This dissertation is divided into ten chapters. The first chapter comprises introduction, summary of aims and objectives and a description of the structure of the thesis.

The second chapter presents a literature review of some aspects of the behaviour of anisotropic clays. Mainly the features of the behaviour, which can not be modelled properly by the current numerical model, are defined and discussed. A conceptual model for the behaviour of one–dimensionally consolidated clays is developed in this chapter.

Conclusions from the second chapter are used to modify the current numerical model. This model is formulated in the third chapter.

One of the main modifications to the current constitutive model, the different flow rule, is defined without introducing an additional model parameter by a simple requirement to correctly predict the K_0 stress state for normally consolidated soil. The aim of the fourth chapter is to present evidence that this modification leads to an improvement in the predictions of data from a large range of different laboratory tests in triaxial and 3D stress state.

To fulfil the aims of the project it is essential to have the numerical model implemented in a finite element program. The fifth chapter describes the implementation of the modified constitutive model into a finite element program. One of the aims of this chapter is to illustrate accuracy of solution. Finally, a boundary value problem in anisotropic reconstituted clay is simulated to demonstrate the capability of the modified model to predict the response of geotechnical structures.

Previous chapters described the development and evaluation of the constitutive model for reconstituted anisotropic clays. This model may be used for modelling natural clays using the sensitivity framework, which is summarised in the sixth chapter. Previous research at City University encountered several problems when this framework was to be applied to model natural clays. To eliminate these problems, it was decided to create artificial structured clays in the laboratory. Previous work on this topic is reviewed and the factors which have the most significant influence on the development of structure in clays are discussed and summarised.

The seventh chapter presents laboratory experiments on the artificial sedimented and reconstituted clays. Results of these experiments are used to develop and evaluate numerical techniques for modelling natural clays.

In the eight chapter, the proposed constitutive model, enhanced by the sensitivity frame-

work, is used to simulate the behaviour of reconstituted and sedimented London Clay.

The ninth chapter fulfills the main aim of the research project. The results of the previous phases of the project enabled the behaviour of a geotechnical structure in natural clay to be modelled, including the stress history and development of structure of a clay stratum. Significant improvements in predictions is demonstrated.

The tenth chapter presents summary and conclusions from the research.

Chapter 2

Some aspects of the behaviour of K_0 consolidated clays

The aim of this chapter is to characterise the mechanical behaviour of clays in order to modify a current constitutive model to predict anisotropic states. Since the area of interest covered in this chapter is very wide, the extent of the dissertation obviously does not allow to include all available literature on clay behaviour in this review. Therefore, the chapter includes topics which are necessary for the modification of the 3–SKH model to predict correctly K_0 conditions and anisotropic states. Moreover, the experimental data concerning the shape of the state boundary surface of anisotropic clays, both in triaxial and octahedral plane, are discussed.

Topics, which are encompassed in this dissertation and lead to the modification of the constitutive model are:

- The shape of the state boundary surface
  - In triaxial stress space (the difference between isotropically and anisotropically consolidated clay)
  - In the octahedral plane
- Direction of the strain increment vector

On the other hand, some features of the existing numerical model remain unchanged and therefore it is not necessary to discuss these topics.

- General critical state soil mechanics behavioural framework

- Influence of recent stress history
- Elastic (quasi–elastic) small strain modulus

2.1 The shape of the state boundary surface

The state boundary surface is a fundamental feature of the critical state concept (Schofield and Wroth, 1968). This surface is defined in stress/volumetric space as the boundary of all possible states of a soil.

2.1.1 The shape of the state boundary surface for anisotropically consolidated clays

When speaking about the shape of the state boundary surface, it is very necessary to emphasize the method, which has been used to define this shape. In general, two particularly different methods are used throughout the literature. Both methods may lead to significantly different results. The assumption used for the sensitivity framework (outlined in Chapter 6) that the state boundary surfaces for natural and reconstituted clay have different sizes but the same shape, is used in this section to enable a comparison between the shape of the state boundary surfaces for anisotropic (natural or reconstituted K_0 consolidated clay) and isotropically consolidated reconstituted clay.

Bilinear methods to define the shape of the state boundary surface

This method, used since the 1960's, is based on the assumption that the behaviour inside the state boundary surface is purely elastic and hence that the yield surface coincides with the state boundary surface.

Methods used to define the shape of the yield envelopes are summarised in Graham et al. (1988). Usually it is common to plot a series of graphs such as σ'_1 versus ϵ_1, p' versus ϵ_v, q versus ϵ_s or σ_3 versus ϵ_3. Yield values obtained from different graphs are usually remarkably similar (Graham et al., 1983). The behaviour of the clay is non–linear except at very small strains and therefore a degree of judgement must be exercised in selecting a yield stresses when using these methods. Various geometrical methods have been proposed to define yield points. The simplest method uses bilinear straight line extrapolations of pre–yield and post–yield portions of the curves, which have different slopes (Parry and Nadarajah, 1973). This technique is depicted in Fig. 2.1 (Callisto and Calabresi, 1998).

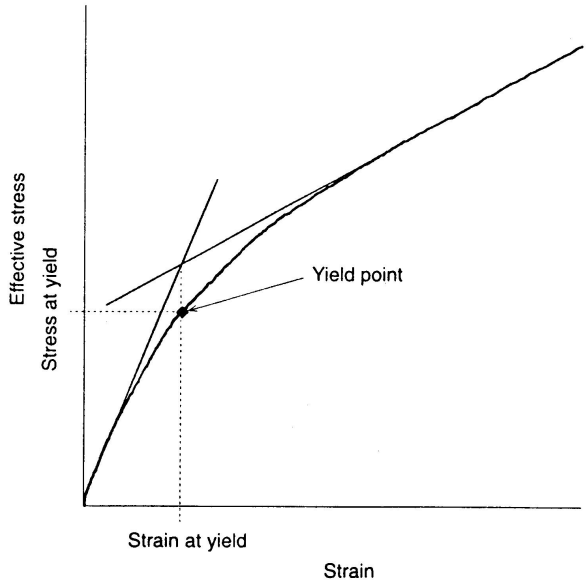

Figure 2.1: *Bilinear method to find the location of yield points (Callisto and Callabresi, 1998)*

Clausen et al. (1984) performed triaxial tests on undisturbed specimens of soft, highly sensitive clay from Norway. Various triaxial stress paths were followed. The resultant yield points and estimated yield locus are shown in p'/q space in Figure 2.2.

An extensive laboratory study of Champlain Clay from St-Alban in Canada is presented in Tavenas and Leroueil (1977). The St-Alban clay is a shoreline deposit of low plasticity, low pore–water salinity and medium to high sensitivity. At least 7 CIU tests and 4 CID tests were performed on triaxial specimens trimmed from a large clay sample and therefore scatter in the results caused by the natural variability of the clay could be reduced to a minimum. The volumetric yield locus was defined using the bilinear method on t/ϵ_v curves (where $t = (\sigma_1 - \sigma_3)/2$). The yield locus is presented in Figure 2.3.

Other researchers, who have used these methods to define the yield locus for anisotropically consolidated clays were, for example, Mitchell (1970), Parry and Nadarajah (1973) and Callisto and Callabresi (1998).

Tavenas et al. (1979) noted that these methods to define the yield surface can not be used systematically. If, for example, a p'/ϵ_v curve is used to define the yield surface, some triaxial stress path will always exist, where ϵ_v is equal to zero. Then some other graph (e.g. q/ϵ_s) must be used. In order to avoid these difficulties and to develop a unique definition of the yield surface they proposed an additional method to define the yield surface. Graphs

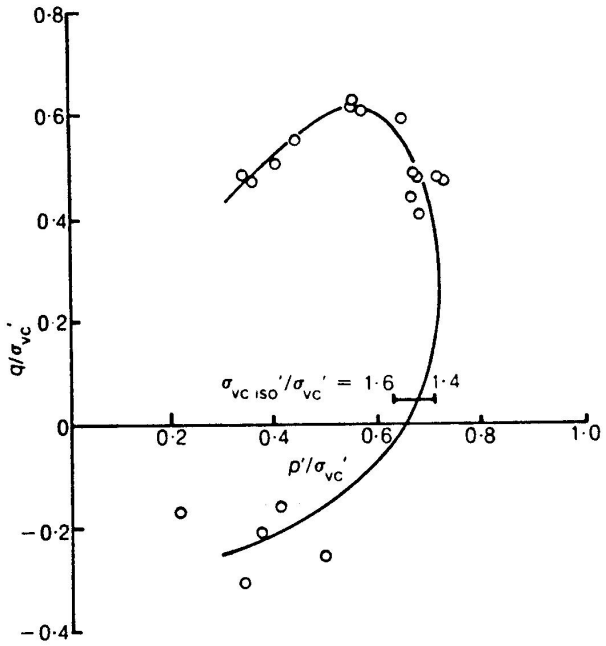

Figure 2.2: *Yield locus after Clausen et al. (1984)*

of the specific strain energy W versus p' and q were used to define the yield points, again using the bilinear method. Specific strain energy is defined as

$$W = \int (\sigma_1 d\epsilon_1 + \sigma_2 d\epsilon_2 + \sigma_3 d\epsilon_3) \tag{2.1}$$

The yield curve defined by this method is shown in Figure 2.4.

It may be seen from Figures 2.2, 2.3 and 2.4 that the yield envelopes for these clays appear to have a very different shape from the yield locus predicted by the Modified Cam Clay model (Roscoe and Burland, 1968). The yield loci appears to have a more or less elliptical shape, but the ellipse is not centered about the isotropic axis but rather about a line close to the K_0 line of the normally consolidated clay.

More recent research on the small strain stiffness behaviour (e.g., Atkinson, 1973; Jardine et al., 1984; Stallebrass, 1990; Viggiani, 1992; Viggiani and Atkinson, 1995) shows that the stress–strain response of clays is nonlinear except at very small strains. Therefore, the bilinear methods used to define the 'yield' points need a large amount of subjectivity. The only objective method, which seemed to confirm the rotated shape of the 'yield' surface was suggested in Crooks and Graham (1976). They realised that contours of equal specific strain energy have a very similar shape to the yield locus defined by the bilinear methods.

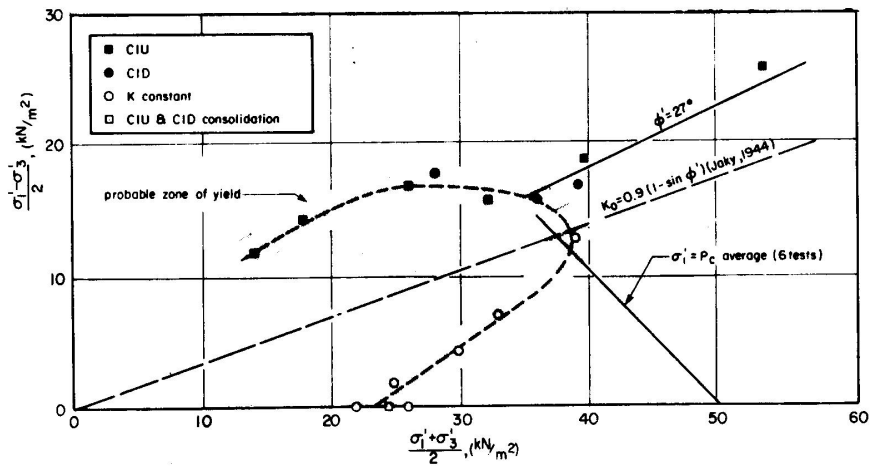

Figure 2.3: *Yield locus after Tavenas et al. (1977)*

This idea was further investigated by Tavenas et al. (1979) and also Callisto and Calabresi (1998). A comparison between the yield locus determined by bilinear methods and the shape of contours of equal specific strain energy from Tavenas et al. (1979) is shown in Fig. 2.4. Although it was found that the yield locus does not correspond exactly with one of the contours of the equal specific strain energy, the shape is roughly similar.

The shape of the state boundary surface found by normalization with respect to specific volume

The second method used to find the shape of the state boundary surface is not based on the assumption that the behaviour inside the state boundary surface is elastic but directly on the definition of the state boundary surface itself. It is common practice to normalise data with respect to specific volume in order to define a constant volume section through the state boundary surface (Graham et al., 1988). For a large set of data, this section through the state boundary surface is the envelope of all normalised stress paths. When data from tests on normally consolidated clay with stress paths along the state boundary surface are normalised, the constant volume section through this surface can be obtained directly (Cotecchia and Chandler, 2000).

The most common practice in soil mechanics is to normalise data with respect to the current value of the equivalent pressure on the isotropic normal compression line of the reconstituted clay p_e^* (where p_e^* is the value of p' on the isotropic normal compression line

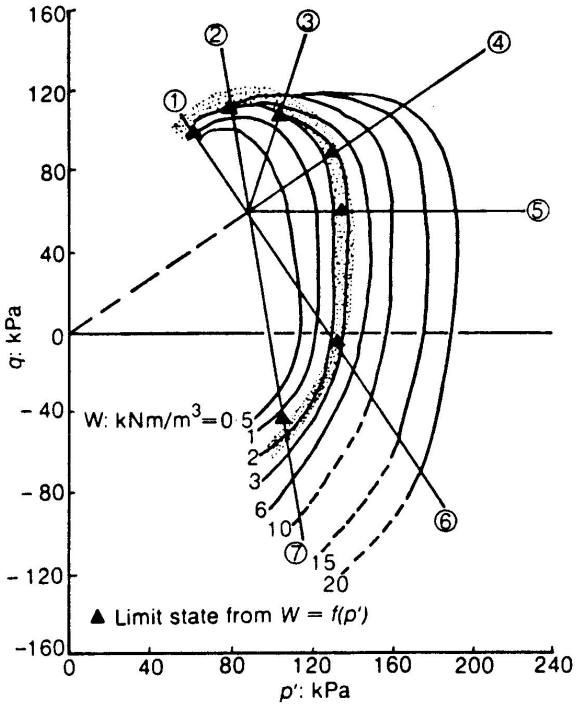

Figure 2.4: *Yield locus defined by the bilinear method and contours of equal specific strain energy. Tavenas et al. (1979)*

(NCL) at the same specific volume as the current specific volume).

$$p_e^* = \exp\left\{\frac{N - \ln(1+e)}{\lambda^*}\right\} \tag{2.2}$$

Pickles (1989) performed a number of laboratory tests designed to define the shape of the state boundary surface for isotropically and K_0 consolidated reconstituted clay. Soft organic silty clay from an alluvial floodplain on the north bank of the River Thames at Beckton, London was used throughout his research.

Two methods were adopted to investigate this problem: "Type 2 probing" with stress paths directed into the SBS (with bilinear method used to define yield points) and "type 1 probing" with stress paths directed along the state boundary surface (with the initial state on the SBS). The stress paths are designed to produce only small plastic strains, thereby keeping disturbance of the soil structure to a minimum. Normalisation with respect to specific volume was then used to find the shape of the state boundary surface.

A limited number of "type 2 probing" tests showed that the location of the yield points

using the bilinear method is very subjective and that the yield points fall well inside the yield curve defined by means of normalisation.

Normalised stress paths from undrained compression tests, drained extension tests with stress paths directed along the state boundary surface and undrained extension tests are plotted in Figure 2.5. The normalised stress paths for the undrained compression and drained extension tests fall close to and are of a similar shape to the Modified Cam Clay state boundary surface, whereas the normalised stress paths for the undrained extension tests have plotted inside this state boundary surface.

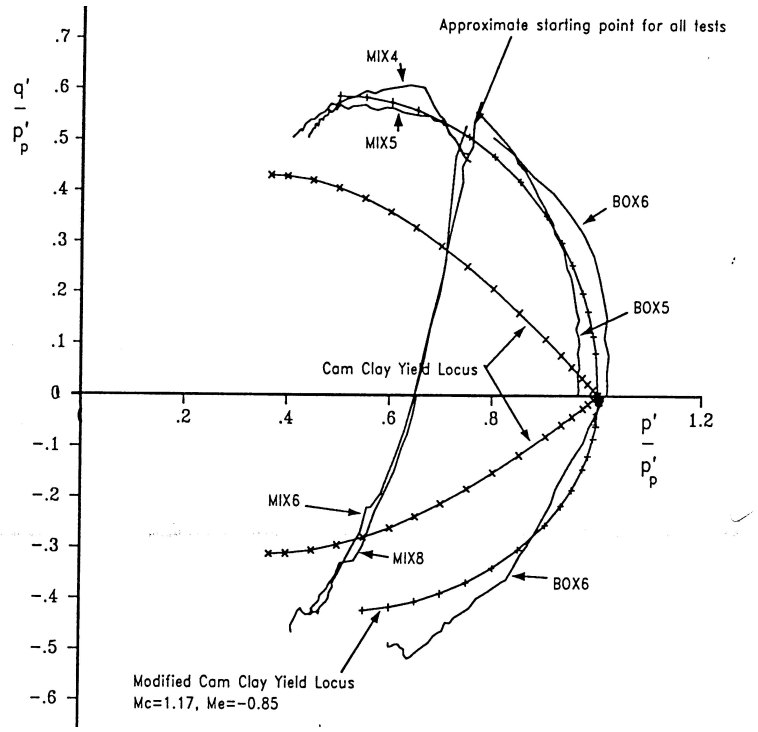

Figure 2.5: *Stress paths for K_0 normally compressed samples normalised with respect to p_e^* (Pickles, 1989)*

The results of the investigation of Pickles (1989) show that there is no apparent difference between the shape of the state boundary surface of the isotropically and one–dimensionally consolidated reconstituted clay, provided the shape of the state boundary surface is found by normalisation.

An extensive laboratory study on pleistocene Pappadai Clay from the Montemesola Basin, Italy, was performed by Cotecchia (1996) and is described in Cotecchia and Chandler (1997) and summarised together with investigations on other natural and reconstituted

clays (Bothkennar, Saint Alban, Sibary, London, Thames Alluvium and Winnipeg clay) in Cotecchia and Chandler (2000).

The shape of the state boundary surface of natural and reconstituted clays were plotted in normalised stress space. Apart from normalization with respect to specific volume, several other normalizing factors were proposed in order to compare the shape of the state boundary surface for clays with different composition and structure. Stress paths normalized with respect to the specific volume and structure of the Pappadai Clay are shown in Fig. 2.6 and 2.7. Figure 2.6 illustrates that when stress paths of tests on normally consolidated clay are normalised they reveal directly the shape of the state boundary surface. If stress paths of tests on overconsolidated clay are normalised, than the state boundary surface is their envelope (Fig. 2.7).

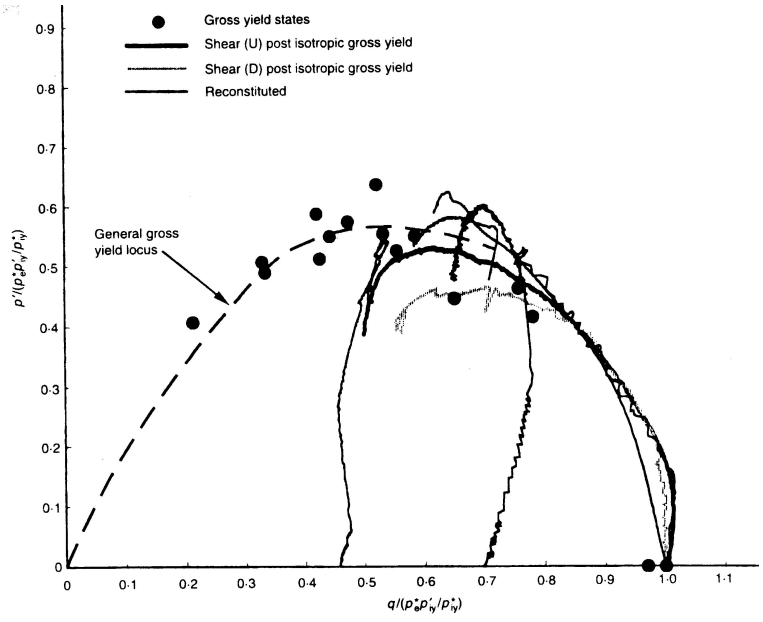

Figure 2.6: *Stress paths of tests on Pappadai clay normalised for both volume and structure (Cotecchia and Chandler, 2000)*

Cotecchia and Chandler (2000) concluded that there appears to be a unique shape of the state boundary surface for a large number of clays studied. This shape is more vertically elongated than the shape predicted by the Modified Cam Clay model. There is no evidence for a rotated state boundary surface for natural (anisotropic) samples.

Triaxial tests on the soft clay beneath the tower of Pisa are described in Rampello and Callisto (1998). A high quality sampling technique was used in order to exclude any significant disturbance of the soil structure. Normalised stress paths for the tests on the

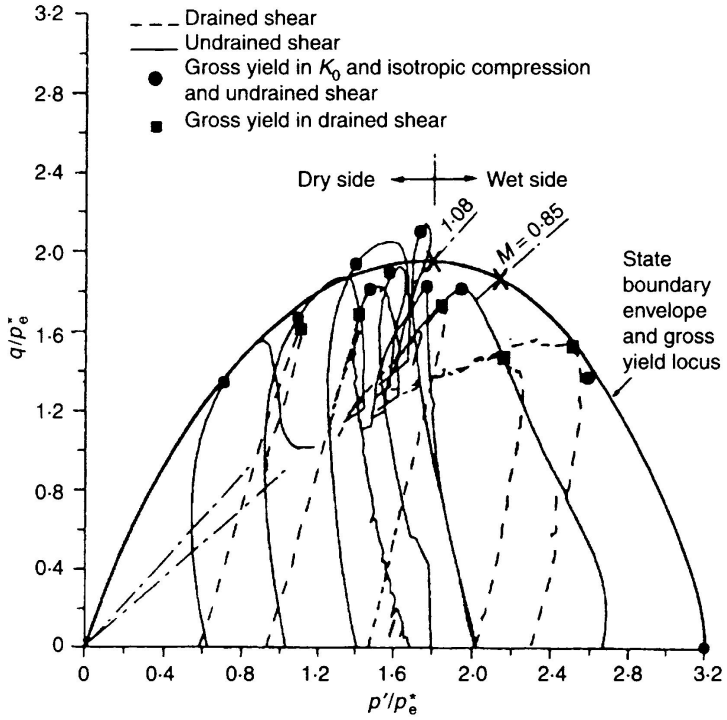

Figure 2.7: *Stress paths of tests on natural Pappadai clay consolidated isotropically for* $OCR > 1$ *(Cotecchia and Chandler, 2000)*

Upper Clay, layer B1, are shown in Figure 2.8. Although, as the authors note, the samples were isotropically consolidated, which may have somewhat obscured the effects of the anisotropic stress history, the shape of the SBS is clearly similar to the Modified Cam Clay SBS without any apparent rotation.

The concept of a rotated yield surface, based on the bi–linear method, is widely used in numerical modelling of the behaviour of anisotropic clay. The use of this concept is reasonable for simple numerical models, where the yield curve coincides with the state boundary surface. Such models are described in, e.g., Davies and Newson (1993), Banerjee and Yousif (1986) and Wheeler (1997). Also in the case of natural soft clays, where the behaviour is more complicated, models with a rotated yield curve may lead to the development of a constitutive model without additional assumptions about the size of the state boundary surface (Karstunen et al., 2001).

On the other hand, numerical models with an elasto–plastic behaviour inside the state boundary surface should predict the shape of the SBS based on the normalisation method. Although it has been shown that the shape of the SBS defined in this way appears to be

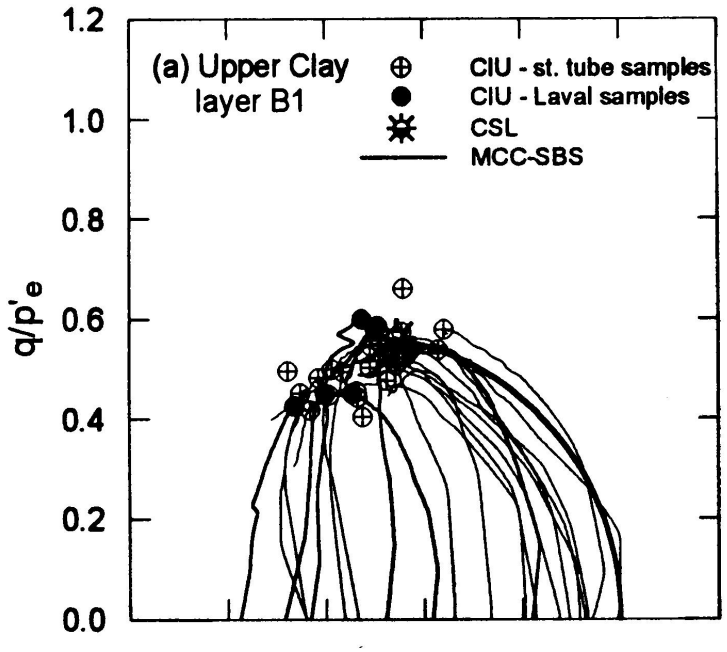

Figure 2.8: *Normalised undrained stress paths, obtained from the triaxial compression tests on undisturbed high quality samples of Upper Pisa Clay, layer B1 (Rampello and Callisto, 1998) (Horizontal axis p'/p_e^*) Points are failure states defined by the bilinear method*

non–rotated, constitutive models with rotated state boundary surface are being developed. Such models were proposed, e.g., by Anandarajah and Daffalias (1986), Whittle (1993), Mróz (1979) and Gajo and Wood (2001). The reason is that models based on the Modified Cam–Clay state boundary surface can not describe the behaviour of anisotropic clays accurately. Nevertheless, as will be shown later (Section 2.2) it is possible to achieve significant improvement of predictions by retaining the non–rotated shape of the state boundary surface and assuming a non–associated flow rule.

2.1.2 The shape of the state boundary surface in the octahedral plane

Numerical models, which are to be used for finite element analysis of geotechnical structures, must be formulated in a three dimensional stress space. The problems concerning the method used to define the shape of the state boundary surface in triaxial stress space, which were discussed in the last section, apply also to the three dimensional stress space.

All data presented to define the shape of the SBS in the octahedral plane (plane in the 3D stress space with constant p') were processed by the bilinear method. Nevertheless, they

will show some features of the behaviour of clays in 3D stress space.

Kirkgard and Lade (1993) performed true triaxial tests on soil from San Francisco Bay, known as San Francisco Bay Mud. This soil contains about 45 % clay particles and 55 % silt particles. Isotropically consolidated undisturbed cubical samples were studied at a constant p' stress state with varying value of lode angle. The yield points were defined using the bilinear method. The yield points, compared with the Mohr–Coulomb and Lade (1977) yield criterion are shown in Figure 2.9. A slightly anisotropic yield envelope is observed. Mohr–Coulomb failure criterion fits reasonably well in triaxial compression and extension, nevertheless the actual yield surface is curved and circumscribes the Mohr–Coulomb failure criterion. Kirkgard and Lade (1993) noted that similar results were found by Shibata and Karube (1965) and Yong and McKyes (1967). On the other hand, Wu et al. (1963) observed a failure envelope similar to the Mohr–Coulomb failure criterion and Vaid and Campanella (1974) a curved failure surface located outside Mohr–Coulomb surface.

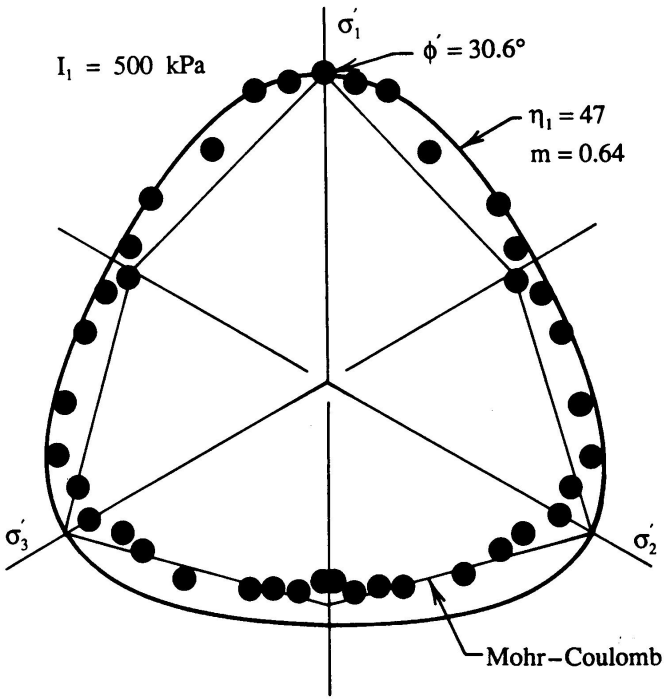

Figure 2.9: *Trace of failure surface for San Francisco Bay Mud in octahedral plane (Kirkgard and Lade, 1993)*

True triaxial tests on the clay from the upper clayey deposit below the Tower of Pisa in the depth range 10.4–20.8 are described in Callisto and Calabresi (1998) and Rampello and Callisto (1998). Similar procedures as in the case of Kirkgard and Lade (1993) were

followed, only the soil tested was anisotropically consolidated in the true triaxial apparatus. The resultant failure envelope for reconstituted clay is shown in Fig. 2.10 and for natural clay in Fig. 2.11. Figure 2.11 also shows the stress–strain curves and assumed yield stresses, from which the subjectivity necessary to define the yield points by the bilinear method is clear.

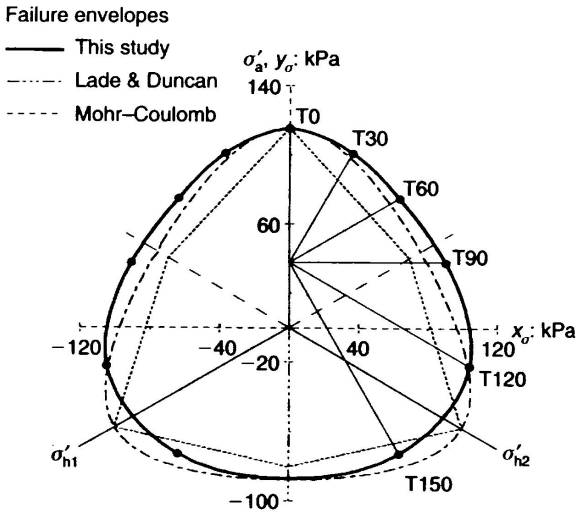

Figure 2.10: *Failure envelope determined from tests in the true triaxial apparatus for reconstituted Upper Pisa Clay*

Pearce (1970) in Wood (1974) performed five constant p' shearing tests on isotropically normally consolidated kaolin in a manually controlled true triaxial apparatus with different values of the lode angle. He reported failure points, which lie only slightly outside the Mohr–Coulomb failure criterion (see Fig. 2.12).

Wood (1974) performed a large number of true triaxial tests on isotropically consolidated Spesstone kaolin. The failure points are shown in Figure 2.13. Wood concludes that the results of certain tests are consistent with a Mohr–Coulomb failure criterion for $\phi = 23°$. Nevertheless, when all yield points are summarised, no clear conclusions may be drawn. Wood notes that the failure points of certain tests were probably influenced by the stress paths which led to failure, especially in the case of a very long tests with a large number of cycles.

Nakai et al. (1986) in Bardet (1990) performed tests on normally consolidated Fujinomori clay in the true triaxial apparatus. Constant p' shearing tests with five different values of lode angles were performed. Failure points, compared with various mathematical expressions for 'lode dependences' (Bardet, 1990) are shown in Figure 2.14. Failure points

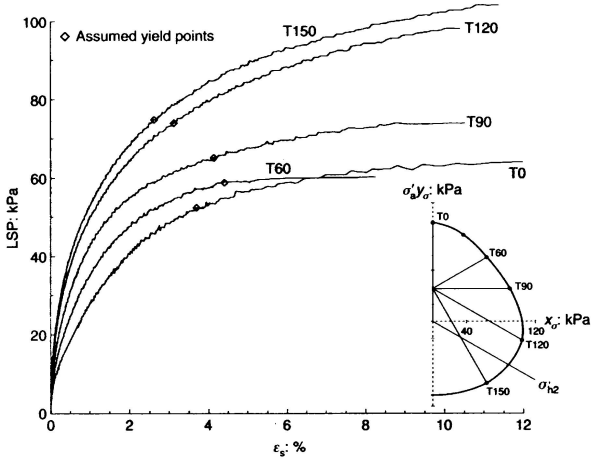

Figure 2.11: *Stress–strain curves, assumed yield points and failure envelope obtained in true triaxial tests on undisturbed Upper Pisa Clay samples*

lie outside the Mohr–Coulomb failure criterion, but coincide with it for the values of lode angle $-30°$ and $30°$, thus confirming the results of Kirkgard and Lade (1993) and others.

The investigation of behaviour of natural clay (Pietrafitta clay from central Italy) in a true triaxial apparatus has been performed by Callisto and Rampello (2002). They reported the shape of the failure surface defined by the bilinear method to be cross–anisotropic with higher friction angle in triaxial extension and in a direction of σ_{22} and σ_{33} axes compared to the Mohr–Coulomb and Lade and Duncan (1975) equations. Although the small–strain stiffness can be predicted accurately by the cross–anisotropic elasticity, the large strain stiffness is smaller and its degradation is more gradual in direction σ_{22}, σ_{33} and triaxial extension, than in direction σ_{11}. The shape of the failure surface and shear strain contours are shown in Figure 2.15.

Most experimental data show the curved shape of the failure surface circumscribing the Mohr–Coulomb failure criterion. Some researchers report the same friction angle in triaxial compression and extension, some report slightly higher friction angles in the triaxial extension. Various mathematical formulae to describe this shape have been proposed in the literature. Some of them are summarised in Bardet (1990). Two types of expressions have been proposed – first with one parameter, friction angle ϕ (or stress ratio M=q/p) in triaxial compression. In the case of these formulations the ratio of M in triaxial compression (M_c) and extension (M_e) is fixed. A different friction angle in triaxial extension is assumed in the case of failure criterion of Lade and Duncan (1975) and the most recent simple convex surface by Hashiguchi (2002). Matsuoka and Nakai (1974) and, obviously,

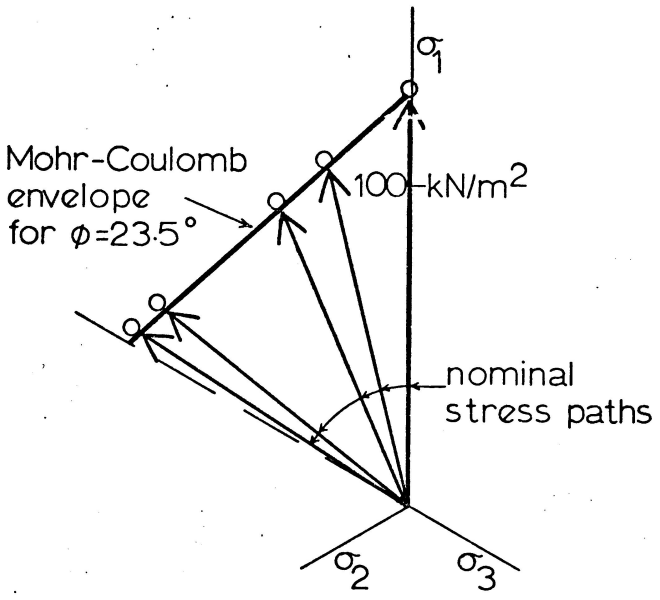

Figure 2.12: *Failure points obtained by Pearce (1970) on Spesstone kaolin in the true triaxial apparatus (Wood, 1974)*

Mohr–Coulomb predict $\phi_e = \phi_c$. The second type of formulas require two parameters, M_c and the ratio $\xi = M_e/M_c$. Between these expressions belong the elliptical 'lode dependence' after William and Warnkle (1975), Argyris (1974), Eekelen (1980) (with one additional shape parameter) and LMN dependence after Bardet (1990). The important feature of these expressions is that they should be convex (Lin and Bažant, 1986). Simpler expressions lose their convexity for parameter ξ smaller than some critical value. Elliptical and LMN dependence are convex for all possible values of ξ (between 0.5 and 1). In the literature on the numerical modelling of clays the popular equation of Argyris (1974) is non–convex for $\xi < 7/9$.

For given values of the parameter ξ the shapes of the presented lode dependences are usually very similar. The similarity (Fig. 2.14) is usually higher than the uncertainty of the derivation of the shape of the SBS from the experimental data (Fig. 2.11). Therefore, only mathematical reasons need to be employed to decide which dependence is suitable for a constitutive model.

It is important to note that no experimental data are available, which would allow the shape of the SBS to be studied by means of normalisation with respect to specific volume. This lack of knowledge must be remembered when numerical models are developed and evaluated.

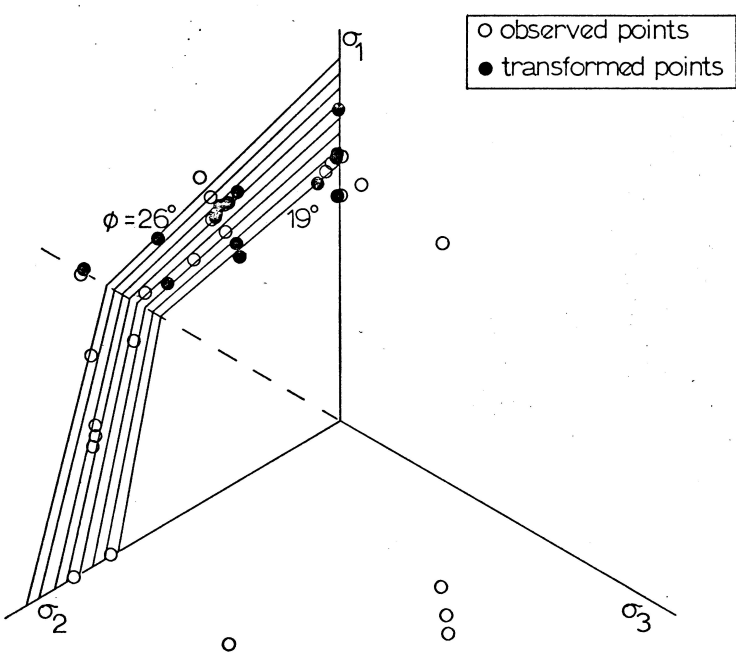

Figure 2.13: *Failure points of all tests performed by Wood, 1974*

2.2 Direction of the strain increment vector

The literature review in section 2.1.1 has shown that the shape of the state boundary surface for anisotropically consolidated clays seems to be symmetric along the isotropic axis. However, the numerical models with the shape of the state boundary surface based on the Modified Cam Clay ellipse are not capable of predicting accurately the behaviour of an anisotropically consolidated clay (see section 4). For example, the K_0 stress state of a normally consolidated clay is usually highly overpredicted (e.g. Gajo and Wood, 2001). It is possible to achieve significant improvement of predictions by retaining the non–rotated shape of the yield surface and assuming a non–associated flow rule. This idea is developed in this section.

This work is based on the assumption that the shape of the plastic potential surface is constant regardless of the stress path undertaken. This assumption is usually accepted, although some research (Cotecchia and Chandler, 2000), based on experimental data, suggest different flow rules for different stress paths.

One of the important states, which may help to define the flow rule, is the K_{0NC} stress state. Several theoretical and empirical relationships for K_{0NC} have been postulated for

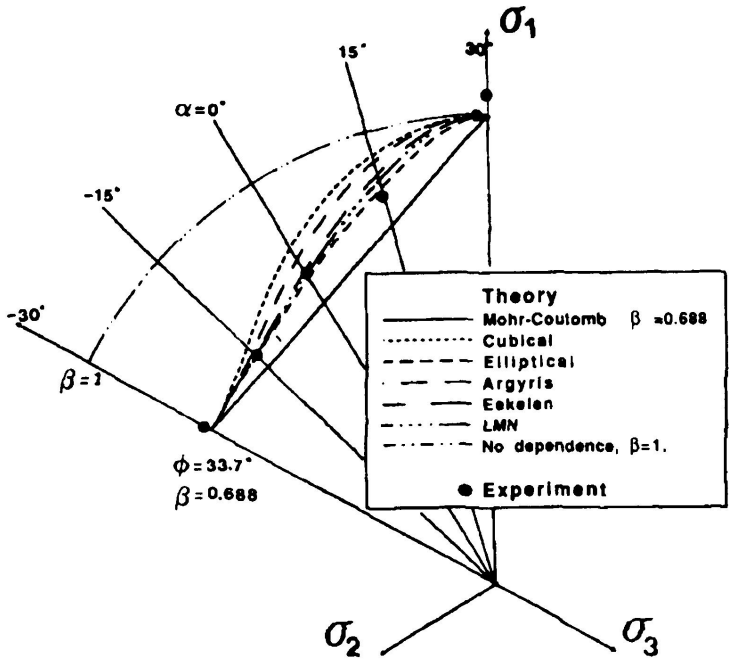

Figure 2.14: *Failure stress in octahedral stress plane for true triaxial tests on Fujinomori Clay (after Nakai et al., 1986) and various mathematical expressions for lode dependences (Bardet, 1990)*

normally–consolidated clays.

Campanella and Vaid (1972) developed a new type of triaxial apparatus, which allowed K_0 conditions to be imposed without side friction, which is the disadvantage of classical oedometer tests. They observed that the value of K_0 is generally constant with consolidation stress, compared to potential variations with ϕ.

Probably the simplest and most widely known is the approximation to the theoretical formula by Jáky (1944) and (1948).

$$K_{0NC} = 1 - \sin\phi \tag{2.3}$$

Several modified versions of this relationship have been published throughout the years (as noted by Cotecchia, 1996). For example:

$$K_{0NC} = 0.95 - \sin\phi \qquad \text{(Brooker and Ireland, 1965)} \tag{2.4}$$

$$K_{0NC} = 1 - 1.2\sin\phi \qquad \text{(Schmidt, 1966)} \tag{2.5}$$

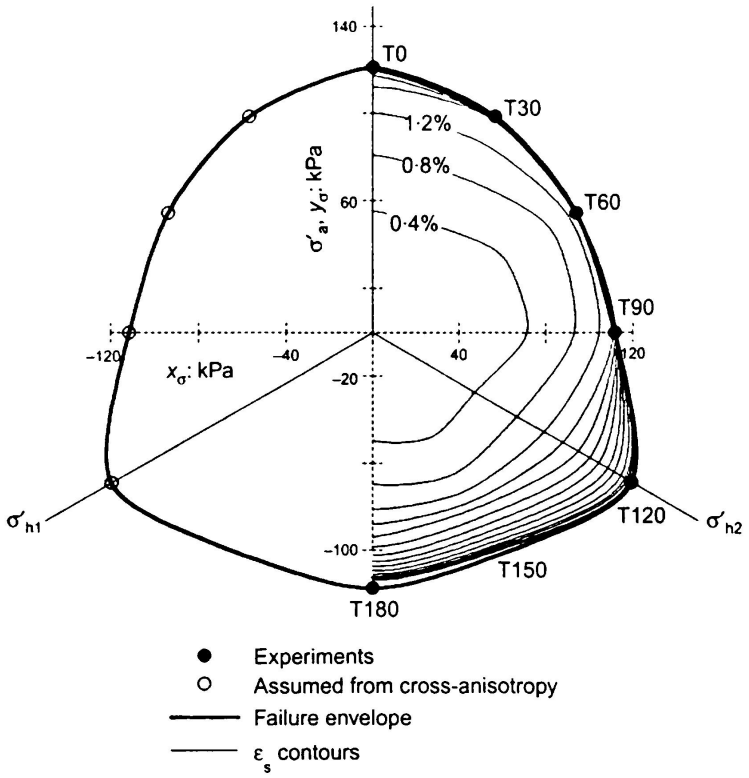

Figure 2.15: *Failure envelope and shear strain contours in the octahedral plane for the natural Pietrafitta clay (Callisto and Rampello, 2002)*

Ladd et al. (1977) collected experimental data from the literature to investigate the relationship between ϕ and K_{0NC}. He studied data for both undisturbed and remoulded clay. The relationship between ϕ and K_{0NC} is shown in Figure 2.16. The majority of the data fall within a band defined by

$$K_{0NC} = (1 - \sin\phi) \pm 0.05 \qquad \text{(Ladd et al., 1977)} \tag{2.6}$$

thus confirming the general validity of Jáky's formula.

Probably the most comprehensive study on the earth coefficient at rest was presented by Mayne and Kulhawy (1982). Their study includes data compiled from 81 different fine–grained soils tested and reported by many researchers. A plot of the relationship relating $\sin\phi$ and K_{0NC} is shown in Figure 2.17. The best fit of the least square method with

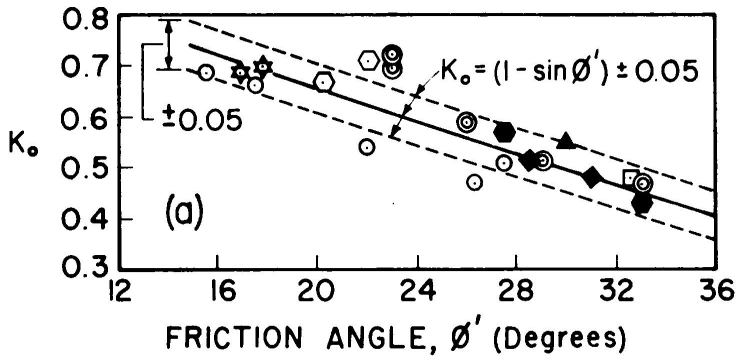

Figure 2.16: *K_0 for normally consolidated clays versus friction angle (Lade et al., 1977)*

intercept 1 on the K_{0NC} axis gives relationship

$$K_{0NC} = 1 - 0.998 \sin \phi \qquad \text{(Mayne and Kulhawy, 1982)} \tag{2.7}$$

which again confirms Jáky's formula for the K_{0NC} stress state.

Ting et al. (1994) performed tests on one–dimensionally consolidated kaolin. The specimens were prepared by sedimentation from a dilute slurry and by remoulding, both in a distilled and sea water. A special consolidometer equipped with horizontal stress transducers was developed for this research. They observed that the empirical relationships for K_{0NC} work well for stresses higher than approximately 70 kPa. However, if the variation of ϕ with the stress is taken into account, the relationships may be valid for even smaller stresses.

If the plastic potential surface should lead to a correct prediction of the K_0 normally consolidated stress state according to Jáky's formula, the critical state should be achieved at the apex of the state boundary surface and an elliptical shape in triaxial stress space is assumed, then this ellipse has a higher ratio of the vertical to horizontal axis than the yield surface (M_{fl} in section 3).

Such a shape is confirmed by the tests performed by Richardson (1988). He performed anisotropic and isotropic compression tests on reconstituted London clay from Bell Common in Essex with five different values of ratio $\eta = q/p$ (0.75, 0.575, 0.25, 0, -0.408). Measured directions of the strain increment (4) and values predicted by the Modified Cam Clay model with an associated flow rule (2) are shown in Figure 2.18. Measured strain increments are total strain increments, but in the case of plastic loading the size of the elastic part of the strain increment may be assumed to be not significant. The Modified

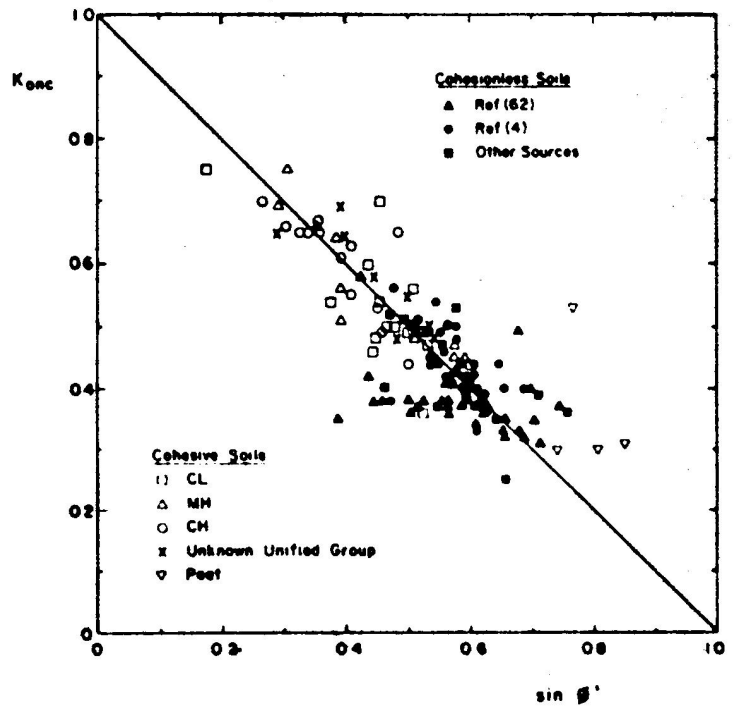

Figure 2.17: *Observed relationship between K_{0NC} and $\sin\phi$ for fine grained and coarse grained soils (Mayne and Kulhawy, 1982)*

Cam Clay model systematically overpredicts the magnitude of shear strains in triaxial loading/compression. On the extension side ($\eta = -0.408$) the predictions are much closer to the measured data. Similar results were found by Dafalias, et al. (1986). In their bounding surface plasticity model they assumed an unusually vertically elongated shape for the state boundary surface in triaxial compression/loading in order to ensure good predictions of the K_{0NC} stress state for the associated flow rule.

Wood (1974) performed true triaxial tests with complicated stress paths. These tests have shown (see Chapter 4) that the best predictions for isotropically consolidated clays require a plastic potential surface with a circular cross–section in the octahedral plane. Similar results were observed by Bardet (1990), who achieved the best predictions with elliptical and LMN lode dependence, together with a non–associated flow rule with a circular cross–section of the plastic potential surface in the octahedral plane.

Similar results, which confirm radial direction for the strain increment in octahedral plane, were presented by Kirkgard and Lade (1993), who performed true triaxial tests on isotropically consolidated natural San Francisco Bay Mud. Vectors of strain increment are shown

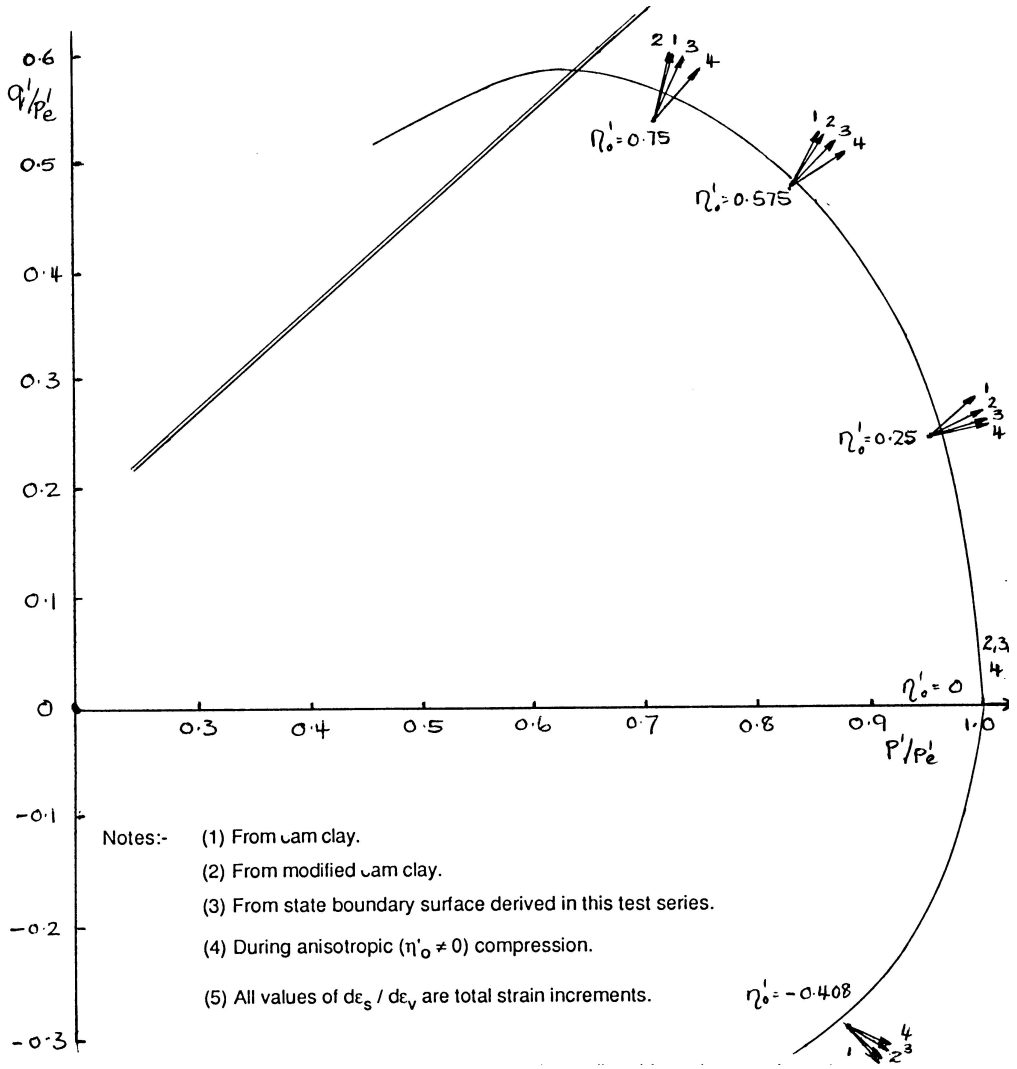

Figure 2.18: *Values of the total strain increment ratio predicted from the state boundary surface and that observed during anisotropic compression for reconstituted London Clay (Richardson, 1988)*

in Figure 2.19.

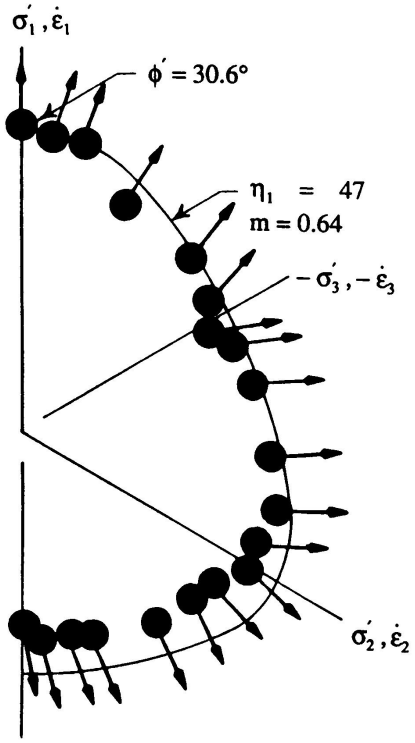

Figure 2.19: *Directions of strain increment vectors in octahedral plane for San Francisco Bay Mud (Kirkgard and Lade, 1993)*

Callisto and Calabresi (1998) performed true triaxial tests on the Upper Pisa clay and plotted directions of the strain increment vectors in octahedral plane at yield (defined by the bi–linear method) and at failure (Fig. 2.20). Although some scatter in experimental data is present (mainly for the test T60), the hypothesis of a circular cross–section of the plastic potential surface in the octahedral plane seems to be confirmed.

2.3 Summary

The literature review has shown that:

- There seems to be no evidence for a rotated shape of the state boundary surface if it is defined by normalising with respect to specific volume. If the shape is defined by the bi–linear method it is apparently rotated in the direction of the K_{0NC} stress path and this shape is similar to the shape of contours of equal specific strain energy.

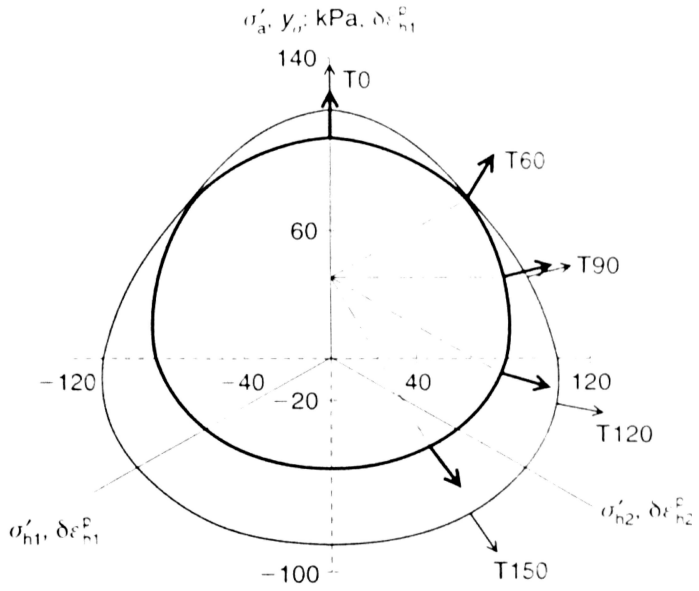

Figure 2.20: *Directions of strain increment vectors in octahedral plane for the Upper Pisa clay at yield (bold arrows) and at failure (thin arrows) (Callisto and Calabresi, 1998).*

- The state boundary surface in the octahedral plane has a shape which circumscribes the Mohr–Coulomb failure envelope. This shape is such that the critical state friction angle is either the same in triaxial compression and extension, or the friction angle in triaxial extension is slightly higher than in compression. The actual shape is far from the shape obtained if the friction coefficient, M, is constant.

- Results of anisotropic compression tests (Fig. 2.18) have shown that the plastic potential surface in triaxial compression is such that it should predict less shear strains, than the plastic potential surface associated with the yield surface. In the triaxial extension the shape of the plastic potential surface is closer to the shape that would be assumed if the flow rule was associated.

- The true triaxial tests on natural clays show that the flow rule should predict radial direction of the plastic strain increment in the octahedral plane (ie., a circular cross–section through the plastic potential surface in the octahedral plane).

Chapter 3

Formulation of the 3-SKH model for anisotropic states (AI3-SKH)

3.1 Introduction

This chapter introduces a new version of the 3-SKH model (Stallebrass, 1990; Stallebrass and Taylor, 1997). This model, developed originally to model behaviour of reconstituted clays, has been extended for natural stiff clays with stable structure (Ingram, 2000) and also soft clays with unstable structure (Baudet, 2000; Baudet and Stallebrass, 2001).

The 3-SKH model is based on the theory of incremental, rate–independent elasto–plasticity and critical state concepts. The model is an extension of the kinematic hardening model proposed by Al-Tabbaa and Wood (1989). The 3-SKH model introduces a second kinematic surface in order to simulate the influence of a recent stress history. Other features of the Al Tabbaa model (the shape of the state boundary surface and plastic potential surface) were preserved. The 3-SKH model uses an elliptical state boundary surface, the same as the Modified Cam Clay model (Roscoe and Burland, 1968), which is generalised to 3D stress states in a simple way which doesn't introduce dependence of the critical state stress ratio M on Lode angle. Associated plasticity is used. Although the model can describe the behaviour of fine grained soils generally well, several shortcomings were defined, which are important for the current research project. The modified model uses a non–rotated state boundary surface with a Matsuoka–Nakai like octahedral cross–section and a non–associated flow rule, developed according to the experimental evidence outlined in Chapter 2.

All equations necessary to define the modified model (called AI3-SKH, because it was developed to describe AnIsotropic states) in general stress space are presented in this section. The elasto–plastic stiffness matrix is calculated analytically. Numerical techniques to evaluate the consistency condition would be computationally more efficient, but the analytical solution ensures that no additional error is introduced to the numerical time integration of the model.

3.2 Basic definitions

The proposed model is based on the theory of incremental, rate–independent elasto–plasticity and critical state concepts. All stresses are effective stresses (the primes have been dropped for simplicity). The geotechnical sign convention was adopted, so the stresses and strains are positive in compression. All tensor quantities are denoted by bold–faced characters. The effective stress tensor will be denoted by $\boldsymbol{\sigma}$ and $\boldsymbol{\epsilon}$ will denote the strain tensor. The symbol ':' between two tensor quantities denotes the double index contraction of their product, e.g. in Cartesian axes between two second–order tensors $\boldsymbol{a} : \boldsymbol{b} = a_{ij}b_{ij}$ (i.e. the inner product), between one fourth and one second–order tensor $(\boldsymbol{D} : \boldsymbol{a})_{ij} = D_{ijkl}a_{kl}$ and finally between two fourth–order tensors $(\boldsymbol{D} : \boldsymbol{K})_{ijmn} = D_{ijkl}K_{klmn}$. The summation convention over repeated indices is employed. The symbol '$\otimes$' stands for the dyadic product between two second–order tensors $\boldsymbol{a}$ and $\boldsymbol{b}$, e.g. the fourth–order tensor $\boldsymbol{a} \otimes \boldsymbol{b}$ such that $(\boldsymbol{a} \otimes \boldsymbol{b}) : \boldsymbol{x} = (\boldsymbol{b} : \boldsymbol{x})\boldsymbol{a}$ for every second–order tensor $\boldsymbol{x}$. The same symbol '$\otimes$' stands for the dyadic product between two vectors. A superposed dot will mean time derivative (and hence an increment in rate–independent formulation) and a comma followed by a subscript variable will imply partial differentiation with respect to that variable (after Gajo and Wood, 2001).

The constitutive model is defined using the stress invariants I, J and θ, where θ is lode angle.

$$I = \boldsymbol{\sigma} : \boldsymbol{\delta} \tag{3.1}$$

$$J = \sqrt{\frac{1}{2}\boldsymbol{s} : \boldsymbol{s}} \tag{3.2}$$

$$\theta = \frac{1}{3}\sin^{-1}\left[\frac{3\sqrt{3}S^3}{2J^3}\right] \tag{3.3}$$

$\boldsymbol{\delta}$ is Kronecker delta.

$$\begin{cases} \delta_{ij} = 1 & \text{for} \quad i = j \\ \delta_{ij} = 0 & \text{for} \quad i \neq j \end{cases} \tag{3.4}$$

Use will also be made of the fourth–order identity tensor $\boldsymbol{I}$, with components:

$$(\boldsymbol{I})_{ijkl} := \frac{1}{2}\left(\delta_{ik}\delta_{jl} + \delta_{il}\delta_{jk}\right) \tag{3.5}$$

The deviator stress is

$$\boldsymbol{s} = \boldsymbol{\sigma} - \frac{I}{3}\boldsymbol{\delta} \tag{3.6}$$

and the third stress invariant S is

$$S = \sqrt[3]{\frac{1}{3}s_{ij}s_{jk}s_{ki}} \tag{3.7}$$

'Triaxial' stress invariants p and q are defined as

$$p = \frac{1}{3}(\sigma_{11} + 2\sigma_{33}) \quad q = \sigma_{11} - \sigma_{33} \tag{3.8}$$

are at triaxial conditions related to I, J and θ by

$$p = \frac{I}{3} \tag{3.9}$$

$$\begin{cases} q = \sqrt{3}J & \text{if} \quad \theta = \frac{\pi}{6} \\ q = -\sqrt{3}J & \text{if} \quad \theta = -\frac{\pi}{6} \end{cases} \tag{3.10}$$

3.3 Incremental stress–strain relationship

According to the basic elasto–plastic assumption, the strain rate $\dot{\boldsymbol{\epsilon}}$ is decomposed into elastic and plastic parts, $\dot{\boldsymbol{\epsilon}}^e$ and $\dot{\boldsymbol{\epsilon}}^p$ respectively.

$$\dot{\boldsymbol{\epsilon}} = \dot{\boldsymbol{\epsilon}}^e + \dot{\boldsymbol{\epsilon}}^p \tag{3.11}$$

The stress increment $\dot{\boldsymbol{\sigma}}$ is related to the elastic strain increment $\dot{\boldsymbol{\epsilon}}^e$ by the fourth–order tensor $\boldsymbol{D^e}$, elastic stiffness matrix.

$$\dot{\boldsymbol{\sigma}} = \boldsymbol{D^e} : \dot{\boldsymbol{\epsilon}}^e \tag{3.12}$$

Elasto–plastic stiffness matrix $\boldsymbol{D^{ep}}$ relates the stress increment $\dot{\boldsymbol{\sigma}}$ and the total strain increment $\dot{\boldsymbol{\epsilon}}$

$$\dot{\boldsymbol{\sigma}} = \boldsymbol{D^{ep}} : \dot{\boldsymbol{\epsilon}} \tag{3.13}$$

The consistency condition, which requires that the stress state after a time increment remains on the yield surface, implies that

$$\boldsymbol{D^{ep}} = \boldsymbol{D^{e}} - \frac{(\boldsymbol{D^{e}} : \boldsymbol{g}_{,\boldsymbol{\sigma}}) \otimes (\boldsymbol{f}_{,\boldsymbol{\sigma}} : \boldsymbol{D^{e}})}{H + \boldsymbol{f}_{,\boldsymbol{\sigma}} : \boldsymbol{D^{e}} : \boldsymbol{g}_{,\boldsymbol{\sigma}}} \tag{3.14}$$

where f, g and H are the yield surface, plastic potential surface and hardening modulus respectively and are defined later in the text.

As for the rate–independent elasto–plastic models in general, the behaviour is assumed to be elasto–plastic, if

$$f = 0 \quad \wedge \quad \boldsymbol{f}_{,\boldsymbol{\sigma}} : \dot{\boldsymbol{\sigma}}^{e} > 0 \tag{3.15}$$

where $\dot{\boldsymbol{\sigma}}^{e}$ is trial stress rate

$$\dot{\boldsymbol{\sigma}}^{e} = \boldsymbol{D^{e}} : \dot{\boldsymbol{\epsilon}} \tag{3.16}$$

If conjunction 3.15 is not fulfilled, the behaviour is elastic (after Herle, 2001).

3.4 Elasticity

Isotropic elasticity is assumed for simplicity, although it was shown that the elastic shear stiffness of one–dimensionally consolidated soils is actually cross–anisotropic (Jovičić, 1997). Cross–anisotropic elasticity, which requires one additional parameter α (Graham and Houlsby, 1983) has already been implemented into the 3-SKH model (Jovičić, 1997) and should be used for modelling highly overconsolidated clays, where the assumptions defining the elastic behaviour make significant differences to model predictions (Ingram, 2000).

The elastic stiffness matrix $\boldsymbol{D^{e}}$ is here defined in terms of young modulus E and Poisson's ratio ν, which may be calculated from model parameters.

$$\frac{G_e}{p_r} = A \left(\frac{p}{p_r} \right)^{n} {R_0}^{m} \tag{3.17}$$

G_e is elastic shear modulus calculated according to the equation after Viggiani and Atkinson (1995), $p = I/3$, p_r is a reference stress 1 kPa, R_0 is the overconsolidation ratio $R_0 = I/(2I_0)$ (I_0 is defined later) and A, n and m are model parameters.

The elasto–plastic stiffness matrix $\boldsymbol{D^e}$ in its general form is

$$\boldsymbol{D^e} = \left(K_e - \frac{2}{3}G_e\right)\,\boldsymbol{\delta}\otimes\boldsymbol{\delta} + 2G_e\,\boldsymbol{I} \tag{3.18}$$

with the elastic bulk modulus K_e

$$K_e = \frac{p}{\kappa^*} \tag{3.19}$$

3.5 Characteristic surfaces

The AI3-SKH model is an extended and generalised version of the 3-SKH model (Stallebrass, 1990) and it preserves all important features of this model. It is developed in the framework of kinematic hardening bounding surface plasticity, with a unique non–rotated bounding surface ($F = 0$), a kinematic yield surface ($f = 0$), which defines the boundary of purely elastic behaviour and a history surface ($f_h = 0$), which defines the boundary of the influence of the recent stress history on soil behaviour. The AI3-SKH model is developed for numerical modelling of natural clays with stable structure. Implementation of the additional isotropic hardening rule defined by Baudet (2001) for the 3-SKH model, which requires only two additional model parameters, would enable soft natural clays to be modelled. The shape of the bounding surface is elliptical and is derived from the yield surface of the Modified Cam Clay model (Roscoe and Burland, 1968). In contrast to the 3-SKH model, the AI3-SKH model does not degrade to the Modified Cam Clay model for any set of parameters. In order to prevent numerical difficulties, the shapes of the yield and history surfaces are geometrically similar to the bounding surface. The characteristic surfaces are defined as follows:

$$f = \frac{1}{2}\left[3\left(\frac{\overline{J}_b}{M\rho_{(\overline{\theta}_b,\xi)}}\right)^2 + \left(\frac{\overline{I}_b}{3}\right)^2 - T^2S^2\left(\frac{I_0}{3}\right)^2\right] \tag{3.20}$$

$$f_h = \frac{1}{2}\left[3\left(\frac{\overline{J}_a}{M\rho_{(\overline{\theta}_a,\xi)}}\right)^2 + \left(\frac{\overline{I}_a}{3}\right)^2 - T^2\left(\frac{I_0}{3}\right)^2\right] \tag{3.21}$$

$$F = \frac{1}{2}\left[3\left(\frac{J}{M\rho_{(\theta,\xi)}}\right)^2 + \frac{I}{9}(I - 2I_0)\right] \tag{3.22}$$

M, T and S are the model parameters. The AI3-SKH model is defined in 'normalised' stress space in the sense outlined by Gajo and Wood (2001). The centre of the yield surface is

$\boldsymbol{\sigma}_b$. The 'normalised' stress tensor with respect to the centre of the yield surface is defined as

$$\overline{\boldsymbol{\sigma}}_b = \boldsymbol{\sigma} - \boldsymbol{\sigma}_b \tag{3.23}$$

$\overline{J}_b$, $\overline{I}_b$ and $\overline{\theta}_b$ are the invariants of the normalised stress tensor $\overline{\boldsymbol{\sigma}}_b$ calculated according to equations 3.1, 3.2 and 3.3 respectively. The same applies to the centre of the history surface $\boldsymbol{\sigma}_a$. I_0 is the centre of the bounding surface (the centre of the bounding surface is on an isotropic axis).

$\rho_{(\theta,\xi)}$ is the function, which introduces dependence of the size of the surfaces on lode angle. This function is sometimes called Lode dependence (after Bardet, 1990). Lode dependence has two parameters – lode angle θ and parameter ξ, which is defined as the ratio of the critical state stress ratio q/p in triaxial extension (M_e) and compression (M_c).

$$\xi = \frac{M_e}{M_c} \tag{3.24}$$

As described in Section 2, Lode dependences should satisfy three requirements: Requirement for aspect ratio, requirement for differentiability and requirement for convexity. The different Lode dependences available usually satisfy the first two requirements. Lode dependences with simple mathematical expressions usually do not satisfy the requirement for convexity for small values of parameter ξ. Because small values of parameter ξ are necessary for the formulation of the plastic potential surface for the AI3-SKH model, a more complex elliptical expression for $\rho_{(\theta,\xi)}$ after William and Warnkle (1975) was adopted.

$$\rho_{(\theta,\xi)} = \frac{2(1-\xi^2)\cos(\pi/6+\theta) + (2\xi-1)\sqrt{4(1-\xi^2)\cos^2(\pi/6+\theta) + \xi(5\xi-4)}}{4(1-\xi^2)\cos^2(\pi/6+\theta) + (2\xi-1)^2} \tag{3.25}$$

ξ is not an additional model parameter, but is derived from existing model parameters in a way, which ensures that the critical state friction angles in triaxial compression and extension are equal.

$$\xi = \frac{3}{3+M} \tag{3.26}$$

This formulation leads to a shape of the yield surface which is close to that of the Mohr–Coulomb failure criterion in an octahedral cross–section, as may be seen in Figure 3.1.

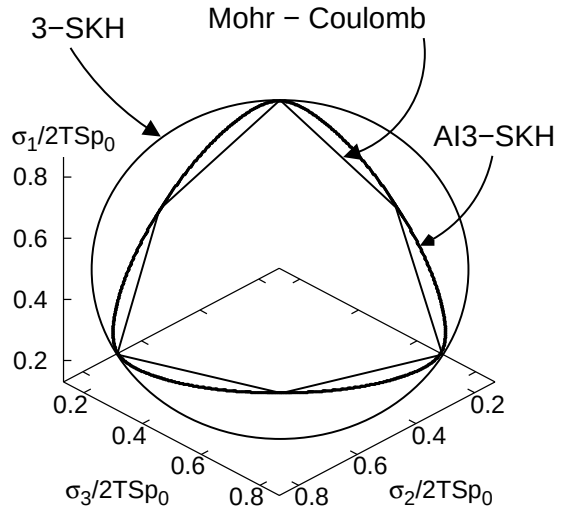

Figure 3.1: *Comparison of deviatoric cross–section through the yield surface of the AI3-SKH model with the 3-SKH model and Mohr–Coulomb failure criterion*

3.5.1 Flow rule

The AI3-SKH model uses a non–associated flow rule and, as shown later, the plastic potential surface can not be explicitly formulated. It is however related to the function:

$$g = \frac{1}{2}\left[3\left(\frac{\overline{J}_b}{M_{fltc}\rho_{\left(\overline{\theta}_b,\xi_{fl}\right)}}\right)^2 + \left(\frac{\overline{I}_b}{3}\right)^2 - T^2S^2\left(\frac{I_0}{3}\right)^2\right] \tag{3.27}$$

This surface consist of ellipses with different ratios between the major and minor axes compared to the yield surface (M_{fltc}). In order not to introduce additional model parameters without clear physical meaning, the value of ratio M_{fltc} in triaxial compression is calculated in order to ensure that the model predicts K_0 normally consolidated states according the equation proposed by Jáky (1948). Imposing this condition leads to the following equation:

$$K_0 = 1 - \sin\phi \tag{3.28}$$

$$M_{fltc} = 3(6-M)\sqrt{\frac{M(1-2\nu)(\lambda-\kappa)}{\left[(1-2\nu)(6-M)\lambda - M\kappa(1+\nu)\right]\left[(6-M)^2-9\right]}} \tag{3.29}$$

The value of the ratio ξ_{fl} is calculated such that the ratio of the major to minor axes of the function g in triaxial extension is equal to the parameter M (it has been shown that

the shape of the plastic potential surface of the 3-SKH model in triaxial extension leads to predictions in good agreement with the experiment):

$$\xi_{fl} = \frac{M}{M_{fltc}} \tag{3.30}$$

A schematic geometrical explanation of the way, in which the function g for the AI3-SKH model is calculated is given in Figure 3.2 (Note non–realistic sizes of surfaces and that the depicted approach does not take into account elastic strains).

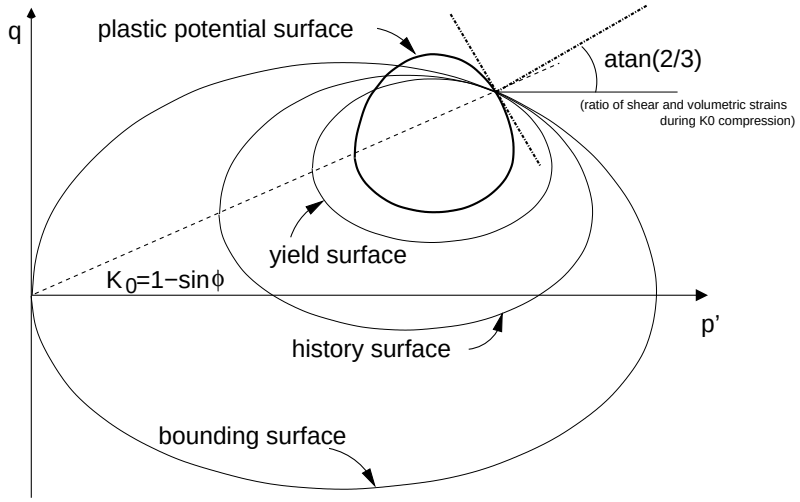

Figure 3.2: *Sketch with the construction of the plastic potential surface for the AI3-SKH model*

The direction of the strain increment vector $\boldsymbol{m}$ is however not calculated as $\boldsymbol{g}_{,\boldsymbol{\sigma}}$, as the term related to the lode–angle dependency is omitted.

$$\boldsymbol{m} = g_{,\overline{J}_b}\overline{\boldsymbol{J}}_{b,\overline{\boldsymbol{\sigma}}_b} + g_{,\overline{I}_b}\overline{\boldsymbol{I}}_{b,\overline{\boldsymbol{\sigma}}_b} \tag{3.31}$$

In this way it is possible to achieve predictions of radial direction of plastic strain increments in the octahedral plane, which are in agreement with experimental data (Sec. 2.2).

3.6 Hardening functions

The AI3-SKH model follows the concept of a unique bounding surface and no rotation or translation of the bounding surface is necessary to improve predictions for K_0 consolidated

soil. The hardening functions are exactly the same as the hardening functions used in the 3-SKH model, generalised into 3D stress space.

3.6.1 Isotropic hardening

Following the Cam Clay tradition, changes in the size of the bounding surface are assumed to depend only on plastic volumetric strains.

$$\dot{I}_0 = \frac{I_0}{\lambda - \kappa} \dot{\epsilon}_v^p \tag{3.32}$$

ϵ_v^p are plastic volumetric strains calculated from

$$\epsilon_v^p = \boldsymbol{\epsilon}^p : \boldsymbol{\delta} \tag{3.33}$$

The same volumetric hardening relationship applies to the centres of the yield and history surfaces.

$$\dot{\boldsymbol{\sigma}}_{bisotr} = \frac{\boldsymbol{\sigma}_b}{\lambda - \kappa} \dot{\epsilon}_v^p \tag{3.34}$$

$$\dot{\boldsymbol{\sigma}}_{aisotr} = \frac{\boldsymbol{\sigma}_a}{\lambda - \kappa} \dot{\epsilon}_v^p \tag{3.35}$$

The isotropic component of the $\dot{\boldsymbol{\sigma}}_b$ is incorporated in the kinematic hardening relationship in equation 3.39, so $\dot{\boldsymbol{\sigma}}_b$ is calculated according to equation 3.39 only. The same applies for $\dot{\boldsymbol{\sigma}}_a$.

3.6.2 Kinematic hardening

The kinematic hardening relationships describe the movement of the yield and history surfaces in stress space. It is necessary to consider three possibilities in the mathematical formulation of the model:

1. The yield surface is not in touch with the history surface
2. The yield surface is in touch with the history surface and not the bounding surface
3. Both yield surface and history surfaces are touching the bounding surface

The kinematic hardening relationship must be formulated separately for these possibilities. The translation rules ensure that the surfaces do not intersect, but meet tangentially

with a common outward normal and maintain contact on subsequent loading. The translation rules also allow for the expansion and contraction of the surfaces caused by plastic volumetric strains.

1. The yield surface is not in touch with the history surface

$$f = 0 \quad \wedge \quad f_h < 0 \quad \wedge \quad F < 0 \quad \wedge \quad \boldsymbol{f}_{,\boldsymbol{\sigma}} : \dot{\boldsymbol{\sigma}}^e > 0 \tag{3.36}$$

In this case only the translation rule for the yield surface must be defined. The yield surface translates along a tensor $\boldsymbol{\gamma}$, which joins the current stress and the conjugate stress on the history surface ($\boldsymbol{\sigma}_{ch}$).

$$\boldsymbol{\sigma}_{ch} = \frac{\overline{\boldsymbol{\sigma}}_b}{S} + \boldsymbol{\sigma}_a \tag{3.37}$$

$$\boldsymbol{\gamma} = \boldsymbol{\sigma}_{ch} - \boldsymbol{\sigma} \tag{3.38}$$

The translation rule for the yield surface is of the form

$$\dot{\boldsymbol{\sigma}}_b = \frac{\dot{I}_0}{I_0}\boldsymbol{\sigma}_b + Z_s\boldsymbol{\gamma} \tag{3.39}$$

where $\dot{I}_0\boldsymbol{\sigma}_b/I_0$ stands for the isotropic component. The expression for Z_s is derived by applying the consistency condition at the yield surface. This gives

$$\boldsymbol{f}_{,\boldsymbol{\sigma}_b} : \dot{\boldsymbol{\sigma}}_b + \boldsymbol{f}_{,\boldsymbol{\sigma}} : \dot{\boldsymbol{\sigma}} + f_{,I_0}\dot{I}_0 = 0 \tag{3.40}$$

Combining equations 3.39 and 3.40 leads eventually to

$$Z_s = \frac{\boldsymbol{f}_{,\boldsymbol{\sigma}} : (\dot{\boldsymbol{\sigma}} - \frac{\dot{I}_0}{I_0}\boldsymbol{\sigma}_b) + f_{,I_0}\dot{I}_0}{\boldsymbol{f}_{,\boldsymbol{\sigma}} : \boldsymbol{\gamma}} \tag{3.41}$$

From equation 3.20

$$f_{,I_0} = \frac{-T^2S^2I_0}{9} \tag{3.42}$$

From equation 3.32

$$\frac{\dot{I}_0}{I_0} = \frac{\dot{\epsilon}_v^p}{\lambda - \kappa} \tag{3.43}$$

From equation 3.23

$$\boldsymbol{f}_{,\boldsymbol{\sigma}} = \boldsymbol{f}_{,\overline{\boldsymbol{\sigma}}_b} \tag{3.44}$$

Adopting the chain rule on equation 3.20 leads to

$$\boldsymbol{f}_{,\overline{\boldsymbol{\sigma}}_b} = f_{,\overline{J}_b}\overline{\boldsymbol{J}}_{b,\overline{\boldsymbol{\sigma}}_b} + f_{,\overline{I}_b}\overline{\boldsymbol{I}}_{b,\overline{\boldsymbol{\sigma}}_b} + f_{,\rho_{\left(\overline{\theta}_b,\xi\right)}}\rho_{\left(\overline{\theta}_b,\xi\right),\overline{\theta}_b}\overline{\boldsymbol{\theta}}_{b,\overline{\boldsymbol{\sigma}}_b} \tag{3.45}$$

From equation 3.20

$$f_{,\overline{I}_b} = \frac{\overline{I}_b}{9} \tag{3.46}$$

$$f_{,\overline{J}_b} = \frac{3\overline{J}_b}{M^2\rho^2_{\left(\overline{\theta}_b,\xi\right)}} \tag{3.47}$$

$$f_{,\rho_{\left(\overline{\theta}_b,\xi\right)}} = \frac{-3\overline{J}_b{}^2}{M^2\rho^3_{\left(\overline{\theta}_b,\xi\right)}} \tag{3.48}$$

If the numerator in equation 3.25 is u and the denominator is v (equation 3.25 is $\rho_{(\theta,\xi)} = u/v$), then obviously

$$\rho_{(\theta,\xi),\theta} = \frac{u_{,\theta}v - v_{,\theta}u}{v^2} \tag{3.49}$$

Here (from 3.25)

$$u_{,\theta} = 2(1-\xi^2)\sin\left(\frac{\pi}{6}+\theta\right) + \frac{2\left(2\xi-1\right)\left(1-\xi^2\right)\sin\left(\frac{\pi}{3}+2\theta\right)}{\sqrt{4\left(1-\xi^2\right)\cos^2\left(\frac{\pi}{6}+\theta\right)+\xi\left(5\xi-4\right)}} \tag{3.50}$$

$$v_{,\theta} = 4\left(1-\xi^2\right)\sin\left(\frac{\pi}{3}+2\theta\right) \tag{3.51}$$

Only derivatives of stress invariants I, J and θ with respect to stress are now necessary in order to calculate $\boldsymbol{f}_{,\boldsymbol{\sigma}}$ and Z_s.

$$\boldsymbol{I}_{,\boldsymbol{\sigma}} = \boldsymbol{\delta} \tag{3.52}$$

$$\boldsymbol{J}_{,\boldsymbol{\sigma}} = \frac{\boldsymbol{s}}{2J} \tag{3.53}$$

$$\boldsymbol{\theta}_{,\boldsymbol{\sigma}} = \frac{1}{J\cos 3\theta}\left(-\frac{\sqrt{3}\boldsymbol{\delta}}{3} - \frac{\boldsymbol{s}}{2J}\sin 3\theta + \sqrt{3}\frac{s_{ik}s_{kj}}{2J^2}\right) \tag{3.54}$$

Derivative $\overline{\boldsymbol{I}}_{b,\overline{\boldsymbol{\sigma}}_b}$ is calculated according to equation 3.52 replacing $\boldsymbol{I}_{,\boldsymbol{\sigma}}$ by $\overline{\boldsymbol{I}}_{b,\overline{\boldsymbol{\sigma}}_b}$ and $\boldsymbol{\sigma}$ by $\overline{\boldsymbol{\sigma}}_b$. The same applies for all other terms, which are not specified directly.

2. The yield surface is in touch with the history surface and not with the bounding surface

$$f = 0 \quad \wedge \quad f_h = 0 \quad \wedge \quad F < 0 \quad \wedge \quad \boldsymbol{f}_{,\boldsymbol{\sigma}} : \dot{\boldsymbol{\sigma}}^e > 0 \tag{3.55}$$

In the 'standard' definition of the 3-SKH model the translation rule for both yield and history surfaces are defined in this case. Nevertheless, it is only necessary to define the translation rule for the history surface. The position of the yield surface is then calculated in order to touch the history surface at the conjugate point. This simplifies the mathematical formulation of the model.

The centre of the yield surface is

$$\boldsymbol{\sigma}_b = \boldsymbol{\sigma} - S(\boldsymbol{\sigma} - \boldsymbol{\sigma}_a) \tag{3.56}$$

The translation rule for the history surface is of the same form as the translation rule for the yield surface. The history surface moves along a tensor $\boldsymbol{\beta}$, defined as:

$$\boldsymbol{\beta} = \frac{\boldsymbol{\sigma} - \boldsymbol{\sigma}_b}{TS} + \boldsymbol{\sigma}_0 - \frac{\boldsymbol{\sigma} - \boldsymbol{\sigma}_b}{S} - \boldsymbol{\sigma}_a \tag{3.57}$$

where $\boldsymbol{\sigma}_0$ is the centre of the bounding surface. The translation rule for the history surface is

$$\dot{\boldsymbol{\sigma}_a} = \frac{\dot{I}_0}{I_0}\boldsymbol{\sigma}_a + W_s\boldsymbol{\beta} \tag{3.58}$$

here W_s is derived from consistency condition in the same way as Z_s

$$W_s = \frac{\boldsymbol{f}_{h,\boldsymbol{\sigma}} : (\dot{\boldsymbol{\sigma}} - \frac{\dot{I}_0}{I_0}\boldsymbol{\sigma}_a) + f_{,I_0}\dot{I}_0}{\boldsymbol{f}_{h,\boldsymbol{\sigma}} : \boldsymbol{\beta}} \tag{3.59}$$

where $\boldsymbol{f}_{h,\boldsymbol{\sigma}}$ may be calculated from the $\boldsymbol{f}_{,\boldsymbol{\sigma}}$

$$\boldsymbol{f}_{h,\boldsymbol{\sigma}} = \frac{\boldsymbol{f}_{,\boldsymbol{\sigma}}}{S} \tag{3.60}$$

3. Both yield surface and history surfaces are touching bounding surface

$$f = 0 \quad \wedge \quad f_h = 0 \quad \wedge \quad F = 0 \quad \wedge \quad \boldsymbol{f}_{,\boldsymbol{\sigma}} : \dot{\boldsymbol{\sigma}}^e > 0 \tag{3.61}$$

In this case only isotropic hardening (equation 3.32) applies to the centre of the bounding surface. The centre of the yield and history surfaces are calculated according to equations

$$\boldsymbol{\sigma}_b = \boldsymbol{\sigma} - TS(\boldsymbol{\sigma} - \boldsymbol{\sigma}_0) \tag{3.62}$$

$$\boldsymbol{\sigma}_a = \boldsymbol{\sigma} - T(\boldsymbol{\sigma} - \boldsymbol{\sigma}_0) \tag{3.63}$$

3.7 Plasticity modulus H

The expression for the plastic modulus H is the same as for the 3-SKH model, only generalised in order to take account of the variation in soil properties with the lode angle. As in the 3-SKH model

$$H = h_0 + H_1 + H_2 \tag{3.64}$$

where h_0 is the plastic modulus at the conjugate point on the bounding surface and terms H_1 and H_2 are parts of the 'mapping rule', which relates the plastic modulus H to the degree of approach of the history surface to the bounding surface and the yield surface to the history surface respectively.

$$h_0 = -\boldsymbol{m} : \boldsymbol{f}_{,\boldsymbol{\epsilon}^p} \tag{3.65}$$

$\boldsymbol{m}$ was defined in Equation 3.31 and

$$\boldsymbol{f}_{,\boldsymbol{\epsilon}^p} = \frac{\boldsymbol{\delta}}{\lambda - \kappa}\left[f_{,I_0} I_0 - \left(f_{,\overline{J}_b}\overline{\boldsymbol{J}}_{b,\overline{\boldsymbol{\sigma}}_b} + f_{,\overline{I}_b}\overline{\boldsymbol{I}}_{b,\overline{\boldsymbol{\sigma}}_b} + f_{,\rho_{\left(\overline{\theta}_b,\xi\right)}}\rho_{\left(\overline{\theta}_b,\xi\right),\overline{\theta}_b}\overline{\boldsymbol{\theta}}_{b,\overline{\boldsymbol{\sigma}}_b}\right) : \boldsymbol{\sigma}_b\right] \tag{3.66}$$

All terms in equation 3.66 have already been specified. Terms H_1 and H_2 are expressed by

$$H_1 = S^2\left(\frac{b_1}{b_{1max}}\right)^{\psi}\frac{1}{\lambda-\kappa}\left(\frac{I_0}{3}\right)^3 \tag{3.67}$$

$$H_2 = \left(\frac{Tb_2}{b_{2max}}\right)^{\psi}\frac{1}{\lambda-\kappa}\left(\frac{I_0}{3}\right)^3 \tag{3.68}$$

b_1 is the measure of the distance between conjugate points on the history surface and the bounding surface, defined as the scalar product of the tensor $\boldsymbol{\beta}$ and the normal to the history surface $\boldsymbol{f}_{h,\boldsymbol{\sigma}}$ divided by a measure of the size of the history surface $TI_0/3$ and it is normalised by its maximum value b_{1max}. b_2 is defined in the same way for the yield surface.

$$b_1 = \frac{3}{TI_0}\left(\boldsymbol{\beta} : \boldsymbol{f}_{h,\boldsymbol{\sigma}}\right) \tag{3.69}$$

$$b_2 = \frac{3}{TSI_0}\left(\boldsymbol{\gamma} : \boldsymbol{f}_{,\boldsymbol{\sigma}}\right) \tag{3.70}$$

and

$$b_{1max} = \frac{2}{3}I_0(1-T) \tag{3.71}$$

$$b_{2max} = \frac{2}{3}TI_0(1-S) \tag{3.72}$$

The 3-SKH model may be obtained by setting $M_{fltc} = M$ and $\rho_{(\theta,\xi)} = 1$.

Chapter 4

Single element evaluation of the AI3-SKH model

The applicability of the proposed approach to the numerical modelling of clays is demonstrated in this chapter. It is shown that the non-associated flow rule formulation of the model can describe the behaviour of clays with improved agreement with experimental data without introducing a number of extra model parameters.

4.1 Modelling triaxial tests on reconstituted Boom clay

Laboratory element tests on reconstituted Boom clay are summarised in Coop et al. (1995) and are reported in detail in Zeniou (1993), Argyrou (1992) and Agah (1996).

The tertiary formation, known as the Boom clay, is the youngest argillaceous unit of a sequence of marine clays and sands, which were deposited in the northern European sedimentary province during Middle Oligocene (Rupelian) some 30 million years ago. The Boom clay is present in the NE of Belgium, partly in the region known Campine. It outcrops to the south of this region and dips gently to the NNE, under a cover of Miocene and Pliocene sandy deposits – Horsemann et al. (1987) in Zeniou (1993).

In the vicinity of the experimental site at Mol, the clay lies at about 160 m below ground surface and has a thickness of about 110 m. It is overlain by the Antwerp sands, which constitute a major industrial aquifer. The clay is rich in pyrite and marcasite. Near the surface, the clay is described as a "stiff, fissured and layered clay". The degree of fissuring decreases markedly with increasing depth of burial. The samples tested were recovered

during the site investigation from a borehole at a depth of 220 m (Zeniou, 1993).

4.1.1 Preparation of reconstituted Boom clay samples

The reconstituted Boom clay samples were prepared by mixing a dried, powdered sample of the clay with deaired distilled water, at a water content of about 88 %. The slurry was then deaired and placed into a consolidometer tube and consolidated for three weeks. Then the samples were removed from the consolidometer and placed into a triaxial apparatus, where they were consolidated under either K_0 or isotropic conditions and then sheared along various stress paths.

4.1.2 Determination of the model parameters

The determination of values for the parameters used in the 3–SKH model for the Boom Clay is described in Ingram (2000). For the single element simulations in this chapter parameters derived by Ingram (2000) have been used. Only the value of the coefficient of friction M is re–determined (the AI3-SKH model allows for different values of M in triaxial compression and extension).

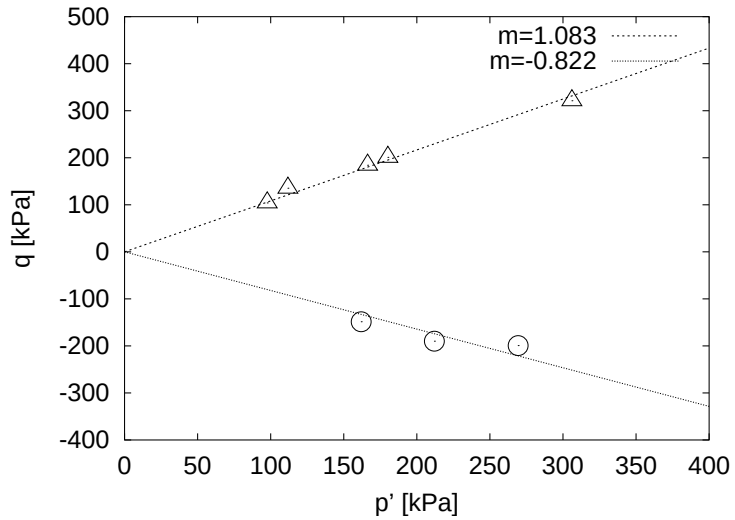

Figure 4.1: *Critical state points and friction envelopes determined from the tests on reconstituted Boom clay samples (test data after Coop et. al (1995))*

The critical state points of the available tests are shown in Figure 4.1. The values of M in compression and extension were found by fitting linear critical state envelopes through these points using the least squares method.

According to equation 3.26 a value of $M_c = 1.083$ leads to $M_e = -0.796$ due to the requirement for the same friction angle in triaxial compression and extension. This value is close to the experimental value -0.822. In order to fit both the extension and compression data with similar accuracy, a value of $M = 1.1$ was adopted. This value leads to $M_e = -0.805$. The values of parameters used for the 3-SKH and AI3-SKH model for the calculations reported in this dissertation are summarised in Table 4.1.

model	A	n	m	M	κ	λ	T	S	ψ	N
3-SKH	180	0.97	0.2	1.03	0.004	0.0984	0.2	0.04	1.6	1.282
AI3-SKH	180	0.97	0.2	1.1	0.004	0.0984	0.2	0.04	1.6	1.282

Table 4.1: *AI3-SKH and 3-SKH model parameters in the simulation of the tests on the reconstituted Boom clay samples.*

The shape of the yield surface of the AI3-SKH model for these parameters is shown in the three dimensional view in principal stress space in Fig. 4.2.

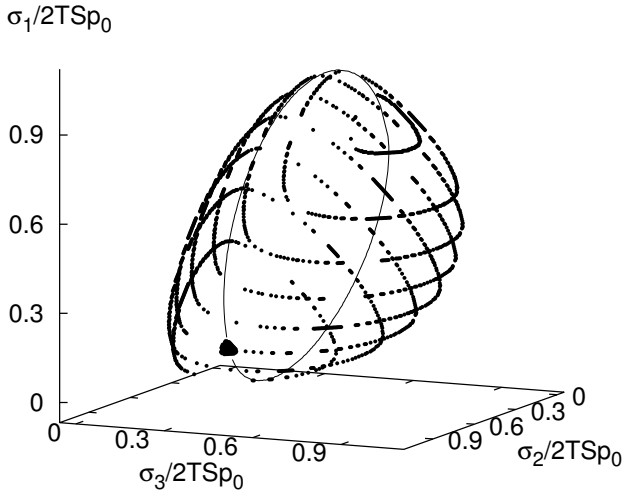

Figure 4.2: *The shape of the yield surface of the AI3-SKH model in principal stress space for the Boom Clay parameters*

4.1.3 Modelling the stress history of the samples

The stress history of the sample is modelled by starting with the stresses imposed by placing the slurry into a consolidometer, when only very small pressures act on the soil. In the numerical model the initial isotropic stress is 0.01 kPa, and this is also the initial position of the centre of the bounding surface. Yield and history surfaces are centred on the initial stress point.

When the 'sample' (slurry) is placed into the consolidometer, K_0 conditions apply and the sample is compressed one–dimensionally to a certain axial stress. When the sample is removed from the consolidometer, it is assumed that under undrained conditions it reaches an isotropic stress state and then it swells isotropically until the initial stress state applied in the triaxial apparatus is achieved. After placing the specimen into the triaxial apparatus its subsequent stress history is clear, since detailed experimental data are available. Description of all calculation stages of the laboratory tests modelled is given in Table 4.2.

4.1.4 Results of simulations

Triaxial K_0 tests

A typical simulation of a K_0 compression and swelling test (boom10) is shown in q/p' space in Figure 4.3. The stress path of the subsequent shearing stage and the positions of kinematic surfaces are also shown.

The results from the AI3-SKH model are closer to experiment with respect to the 3-SKH model. The 3-SKH model overpredicts K_0 conditions. Also the results of K_0 swelling are predicted very well by the AI3-SKH model. This indicates that the flow rule of the AI3-SKH model in triaxial extension is also suitable.

Shear stages of tests modelled

In these simulations the initial states before the shearing stage for simulations by the 3-SKH model are exactly the same as the initial states in the AI3-SKH model simulations (the stress history before shear is not modelled by the 3-SKH model). This offers direct comparison between the 3-SKH and AI3-SKH model response for shear stages.

The q/ϵ_s response for the shearing stages of all laboratory tests modelled are shown in Figures 4.4 and 4.5. For all compression tests on anisotropically consolidated specimens

test number	stage	test type for given stage	final condition
boom7	1	K_0 compression	$p' = 86.7$ kPa
	2	undrained extension	$q = 0$ kPa
	3	isotropic swelling	$p' = 20$ kPa
	4	K_0 compression	$p' = 277$ kPa
	5	constant p' compression	$\epsilon_s = 1.7$ %
	6	constant p' extension	$q = 0$ kPa
	7	constant p' compression	$\epsilon_s = -13$ %
boom8	1	K_0 compression	$p' = 220$ kPa
	2	undrained extension	$q = 0$ kPa
	3	isotropic swelling	$p' = 15$ kPa
	4	K_0 compression	$\sigma_{ax} = 110$ kPa
	5	const. direction in q/p' space	$p' = 112.5$ kPa, $q = 0$ kPa
	6	constant p' compression	$\epsilon_s = 28$ %
boom10	1	K_0 compression	$p' = 170$ kPa
	2	undrained extension	$q = 0$ kPa
	3	isotropic swelling	$p' = 62$ kPa
	4	K_0 compression	$\sigma_{ax} = 350$ kPa
	5	K_0 swelling	$p' = 167$ kPa
	6	constant p' extension	$q = 46$ kPa
	7	constant p' compression	$\epsilon_s = 25$ %
boom11	1	K_0 compression	$p' = 170$ kPa
	2	undrained extension	$q = 0$ kPa
	3	isotropic swelling	$p' = 40$ kPa
	4	K_0 compression	$\sigma_{ax} = 350$ kPa
	5	K_0 swelling	$p' = 162$ kPa
	6	constant p' extension	$\epsilon_s = -20$ %

Table 4.2: *Details of presented simulations of laboratory tests on reconstituted Boom Clay samples.*

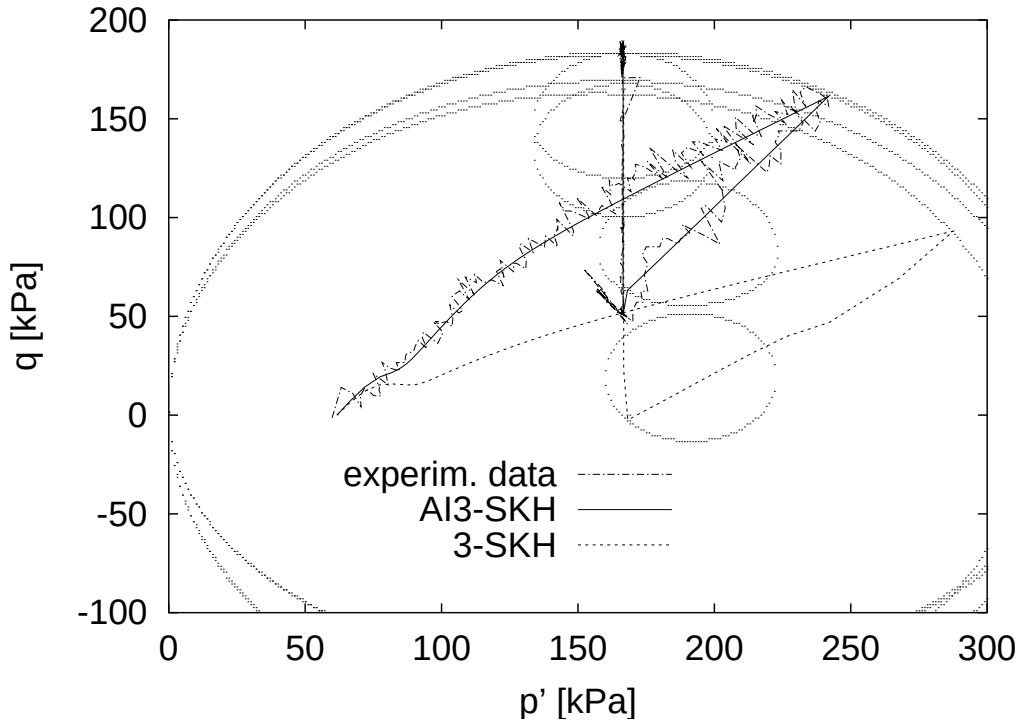

Figure 4.3: *Stress path of the test boom10 and simulation with AI3-SKH and 3-SKH model (test data after Coop et al. (1995)).*

the response is more accurate for the simulations by the AI3-SKH model. The AI3-SKH model predicts, in accordance with experimental data, stiffer large strain behaviour and faster decay of stiffness in extension.

The volumetric/shear graphs are shown in Figure 4.6. For tests on normally consolidated soil (boom7 and boom8) the response of the AI3-SKH model is close to the laboratory data, while the 3-SKH model underpredicts volumetric strains. For shearing stages from the K_0 overconsolidated states the predictions of both the 3-SKH and AI3-SKH models are not accurate. Experimental data show positive volumetric strains, while predicted volumetric strains are negligible.

A typical plot of small strain tangent shear stiffness plotted as $G/log\epsilon_s$ (test boom10) is given in Figure 4.7. The influence of the formulation of the AI3-SKH model on small strain stiffness is in this case rather small and predictions are in good agreement with the experiment.

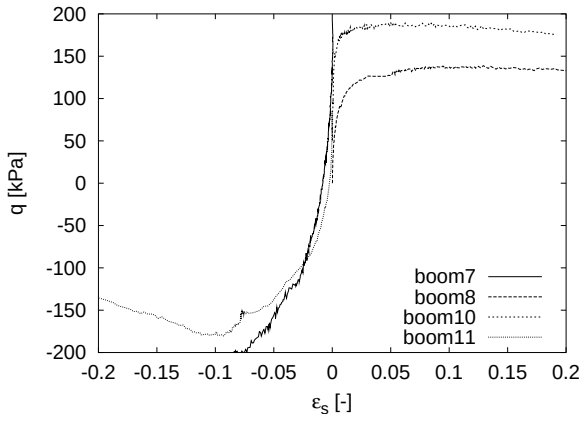

Figure 4.4: *q/ϵ_s graph of the simulated tests on reconstituted Boom Clay samples, experimental data (data after Coop et al. (1995)).*

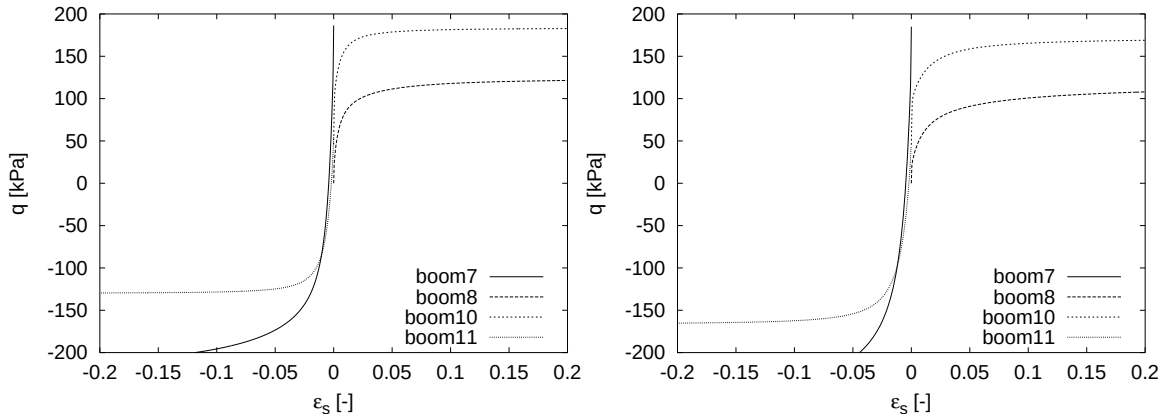

Figure 4.5: *q/ϵ_s graph of the simulated tests on reconstituted Boom Clay samples, AI3-SKH model (left) and 3-SKH model (right).*

4.2 Modelling triaxial tests on reconstituted Pisa clay

The Pisa Clay tested is the Upper Clay, often named Pancone Clay, of the subsoil underneath the Tower of Pisa, Central Italy. Sub–layers B1 and B3 will be examined particularly. The clay was deposited in a shallow brackish-water lagoon environment, about 5000 years BC, at an average rate of deposition of the soil of 2.5 mm/year (Skempton, 1970 in Baudet, 2001). Some erosion of about 50 kPa occurred, which caused the clay to be overconsolidated to a ratio around 1.7 in sub–layer B1 and 1.3 in sub–layer B3. The clay fraction is high, at 60 %, the liquid limit is about 80 % and the plastic limit is approximately constant and equal to 25 %. Consequently, the plasticity index has a value varying between 40 and 50 %. The principal clay minerals in Pisa Clay are illite, vermiculite and some kaolinite.

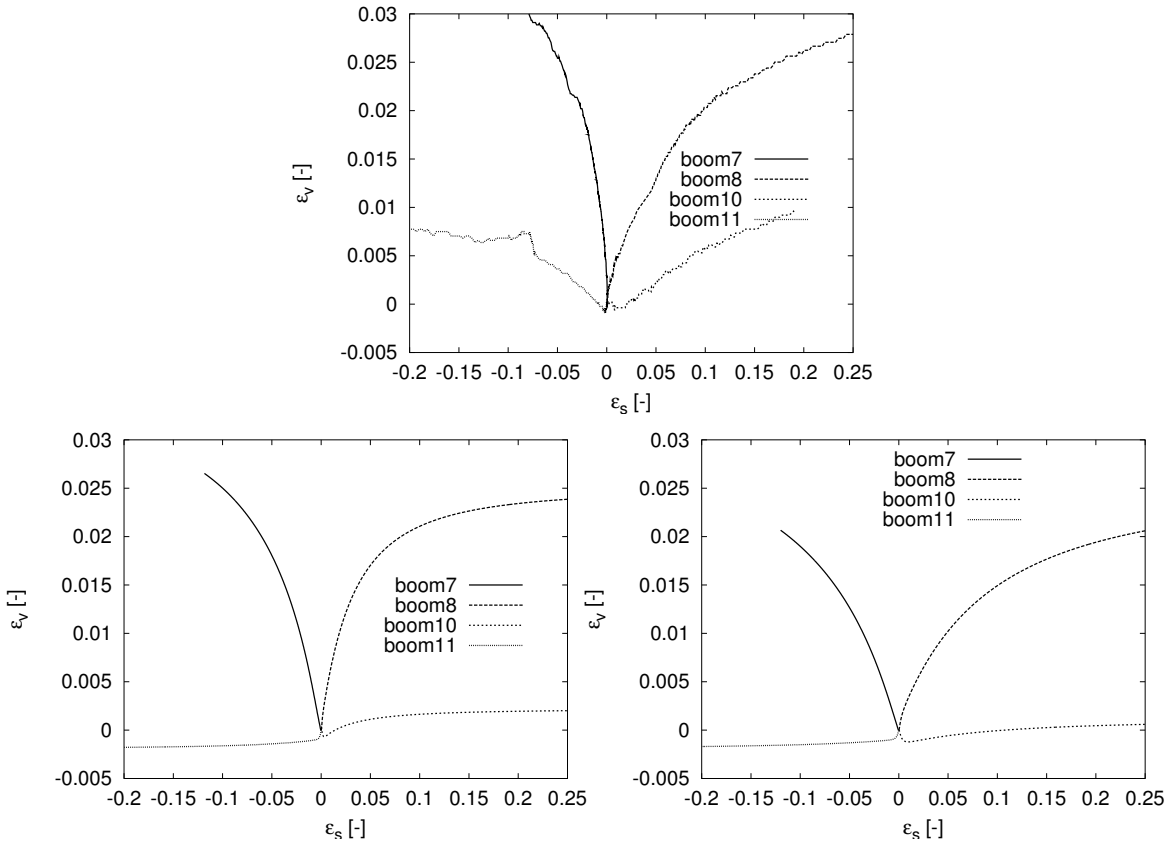

Figure 4.6: ϵ_s/ϵ_v *response of the simulated tests on reconstituted Boom Clay samples, experiment (top) after Coop et al. (1995), AI3-SKH model (left), 3-SKH model (right)*

The calcium carbonate content is about 10 %. The sensitivity of Pisa Clay is usually measured as 5 in the vane shear apparatus, and can be considered constant throughout the homogeneous sublayers B1 and B3 (Baudet, 2001).

4.2.1 Stress history of reconstituted Pisa Clay specimens

The consolidation procedure followed by Callisto (1996) consisted of compressing the reconstituted specimens one–dimensionally to a preconsolidation pressure $\sigma_{ax} = 200$ kPa in an oedometer. The samples were then unloaded to an estimated *in situ* stress ($p' = 88.2$ kPa), in order to simulate the expected stress history of the clay deposit.

Then the sample was removed from the oedometer and was placed into the triaxial apparatus. This procedure is modelled by undrained swelling to an isotropic stress state and then isotropic swelling to a certain isotropic pressure. This pressure was not exactly known.

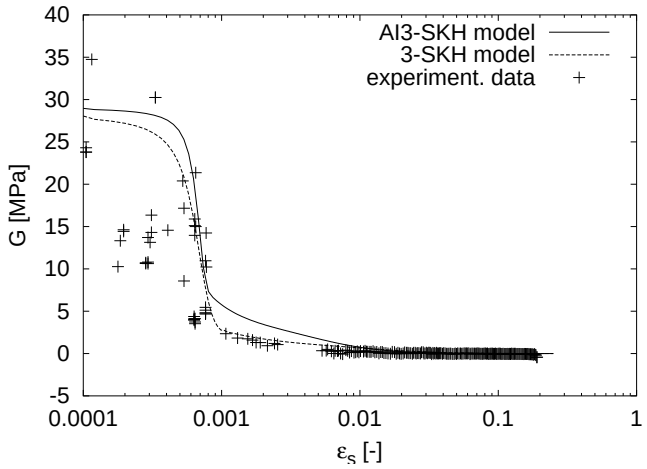

Figure 4.7: *Results of the test boom10 in the G/ϵ_s space.*

Baudet (2001) assumed in her analyses that this pressure is the same as that measured in natural samples of Pisa Clay ($p' = 55$ kPa).

After the specimen was placed into the triaxial apparatus, it was first isotropically compressed to p'=76 kPa and then drained compressed with constant radial stress to the stress level that is expected to be in the ground (p'=88.2 kPa). These conditions were initial states for the tests with constant stress path direction in q/p' space.

4.2.2 Modeling the stress history and determination of the model parameters

Values for the parameters used in the 3-SKH model were derived by Baudet (2001). Baudet derived the majority of parameters from experimental data from tests on reconstituted Pisa Clay. The value of the critical state stress ratio M and the values of parameters which Baudet (2001) derived only on a basis of the parametric study are re–examined in this dissertation (T, S and ψ).

Critical state stress ratio M

The value of the critical state stress ratio M was derived by Callisto (1996) from two drained compression tests, which reached failure. Because the AI3-SKH model uses a different value of M in compression and extension and no extension data are available for the reconstituted Pisa Clay, the value $M = 0.78$ was changed to $M = 0.85$. This value is

given in Rampello and Callisto (1998) for the layer B3 underneath the Tower of Pisa.

Parameters T and S

Baudet (2001) derived the values of parameters T and S on the basis of a parametric study. The value of T is much larger (T=0.5) than the value for this parameter for most soils (T=0.2). Baudet (2001) had to use such a high value in order to ensure realistic predictions of the shear stiffness. The formulation of the AI3-SKH model however allows for higher shear stiffness predicted, compared to the 3-SKH model, therefore a standard value of parameter T, which seems to be more appropriate, is used for the simulations.

The value of the parameter ψ

This value was derived on the basis of the test R30.

Graphs of q/ϵ_s, $G/log\epsilon_s$, p/ϵ_v, $K/log\epsilon_v$ and ϵ_v/ϵ_s for the test R30 are given in Figure 4.8. respectively. Experimental data (Callisto, 1996) and simulations with three different values of parameter ψ (1, 1.5 and 2) are included. It can be seen that the large strain behaviour (q/ϵ_s, p'/ϵ_v, and ϵ_v/ϵ_s plots) is influenced by the value of the parameter ψ only slightly. This behaviour is influenced rather more by the size and shape of the bounding and the plastic potential surface. The large strain behaviour is generally predicted well with all values chosen for the parameter ψ.

The parameter ψ significantly influences the small strain stiffness predictions, both bulk modulus and shear modulus. The value of $\psi = 1.5$ has been adopted on the basis of simulations given in the Fig. 4.8.

The values of the parameters used in the AI3-SKH and the 3-SKH models for the simulations that follow are summarised in Table 4.3.

	A	n	m	M	κ	λ	T	S	ψ	N
AI3-SKH	560	0.82	0.36	0.85	0.0052	0.14	0.2	0.1	1.5	1.575
3-SKH, set 1	560	0.82	0.36	0.78	0.0052	0.14	0.5	0.1	2	1.575
3-SKH, set 2	560	0.82	0.36	0.78	0.0052	0.14	0.2	0.1	1.5	1.575

Table 4.3: *Values for the AI3-SKH and the 3-SKH model parameters used in the simulation of tests on reconstituted Pisa clay samples. set 1 – Simulations by Baudet (2001), set 2 – The 3-SKH model with the initial conditions calculated by the AI3-SKH.*

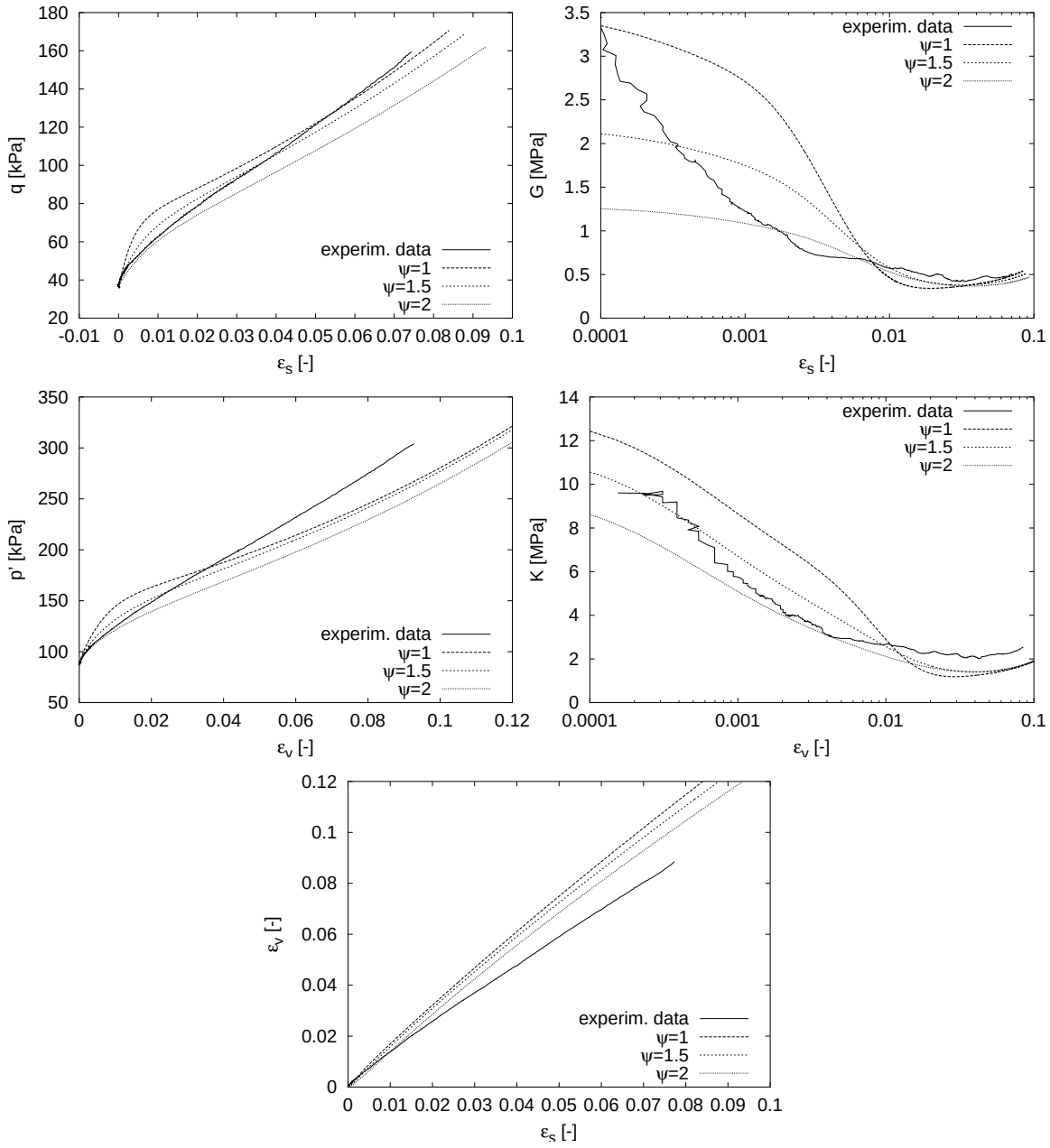

Figure 4.8: *Simulations of the test R30 by the AI3-SKH model with different values of parameter ψ (experimental data after Callisto, 1996)*

Modelling the stress history

The stress history was modelled from the beginning of the preparation of the sample. The stress path modelled by the AI3-SKH model is shown in Fig. 4.9. The initial state is assumed to be $p' = p_0 = p_a = p_b = 0.01$ kPa and $q = q_a = q_b = 0$ kPa (A in in Fig. 4.9). The simulation comprises of the compression under K_0 conditions to $\sigma'_{ax} = 200$ kPa (B) and swelling to to $p' = 88.2$ kPa (C). Then, when the sample is removed from the oedometer, it reaches the isotropic stress state (D) under undrained conditions and then it swells isotropically to a certain isotropic pressure (E). In the simulations this pressure assumed $u_0 = -55$ kPa (as in Baudet (2001)). After the specimen is placed into the triaxial apparatus, the isotropic compression to $p' = 75.87$ kPa (F) and then the drained compression to the expected stress state in the ground ($p' = 88.2$ kPa, $q = 38$ kPa (state G)) is modelled.

4.2.3 Results of simulations

Tests which started from the same initial state with stress probes in a fixed direction in q/p' space were simulated. The tests are named R0 to R315, where the number described the direction of the stress path measured anti–clockwise from the p' axis in degrees. Stress paths of all simulated tests, together with the simulation of the stress history and the position of the surfaces prior to shearing are shown in Figure 4.9.

Three sets of results are compared. (i) Simulations by the AI3-SKH model, (ii) simulations by the 3-SKH model performed by Baudet (2001) with a large value of the parameter T and a stress history which starts when the sample is removed from the consolidometer (run 1). (iii) Simulations using the 3-SKH model, with the initial conditions for the shear stage (the size and position of the surfaces) predicted by the AI3-SKH model (run 2).

The large strain behaviour

q/ϵ_s plots are given in Figure 4.10 and ϵ_v/ϵ_s plots in Figure 4.11. It may be seen that the AI3-SKH model predictions are better compared to the 3-SKH model. Generally, the AI3-SKH model correctly decreases the ratio of the shear to volumetric strain increment, whereas volumetric strains, which are predicted rather correctly by the 3-SKH model, remain unchanged (Figure 4.12).

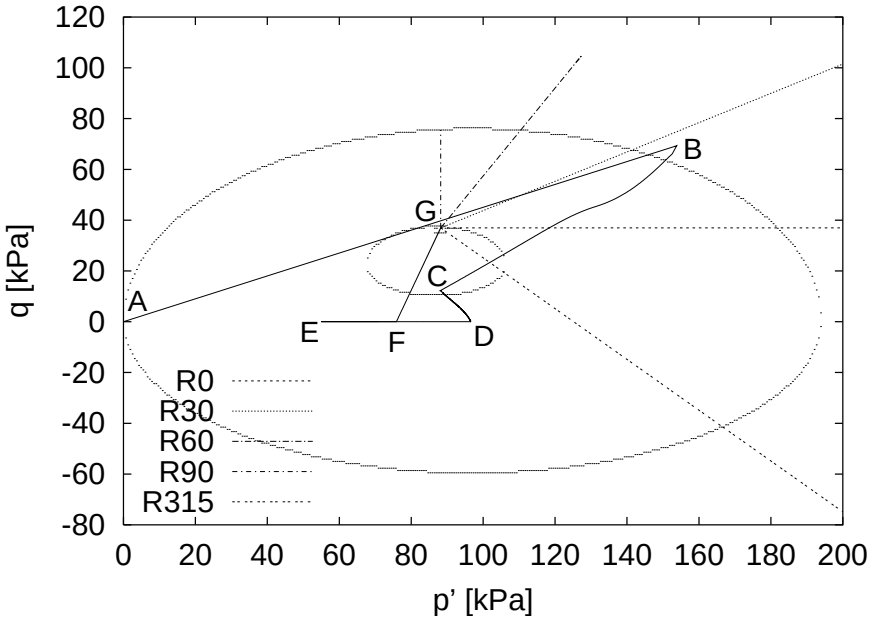

Figure 4.9: *Stress paths of simulated tests on reconstituted Pisa Clay*

The small strain behaviour

The values of the shear and volumetric stiffness measured and predicted for test R30 are shown in Figure 4.13.

It may be seen that the 3-SKH model, run 1, slightly overpredicts the value of the bulk modulus, while the AI3-SKH slightly underpredicts the initial shear stiffness. The quality of both predictions is similar and generally good. The order of magnitude of the initial stiffness and degradation of stiffness is predicted quite well. The AI3-SKH model significantly improves predictions of the shear stiffness compared to the 3-SKH model, run 2. The difference is caused by the non–associated flow rule assumed in the AI3-SKH model. It can be seen that in this case the non–associated flow rule formulation for the AI3-SKH model has a significant effect on the predicted shear stiffness and a small effect on the bulk stiffness.

Predictions of the test in triaxial extension, R315, are shown in Fig. 4.14. The results of the AI3-SKH model and the 3-SKH, run 2, are almost the same. These results are expected, because the shape of the plastic potential surface in extension is similar for both model formulations. The 3-SKH model, run 1, gives results of bulk stiffness close to the experiment and significantly underpredicts the shear stiffness.

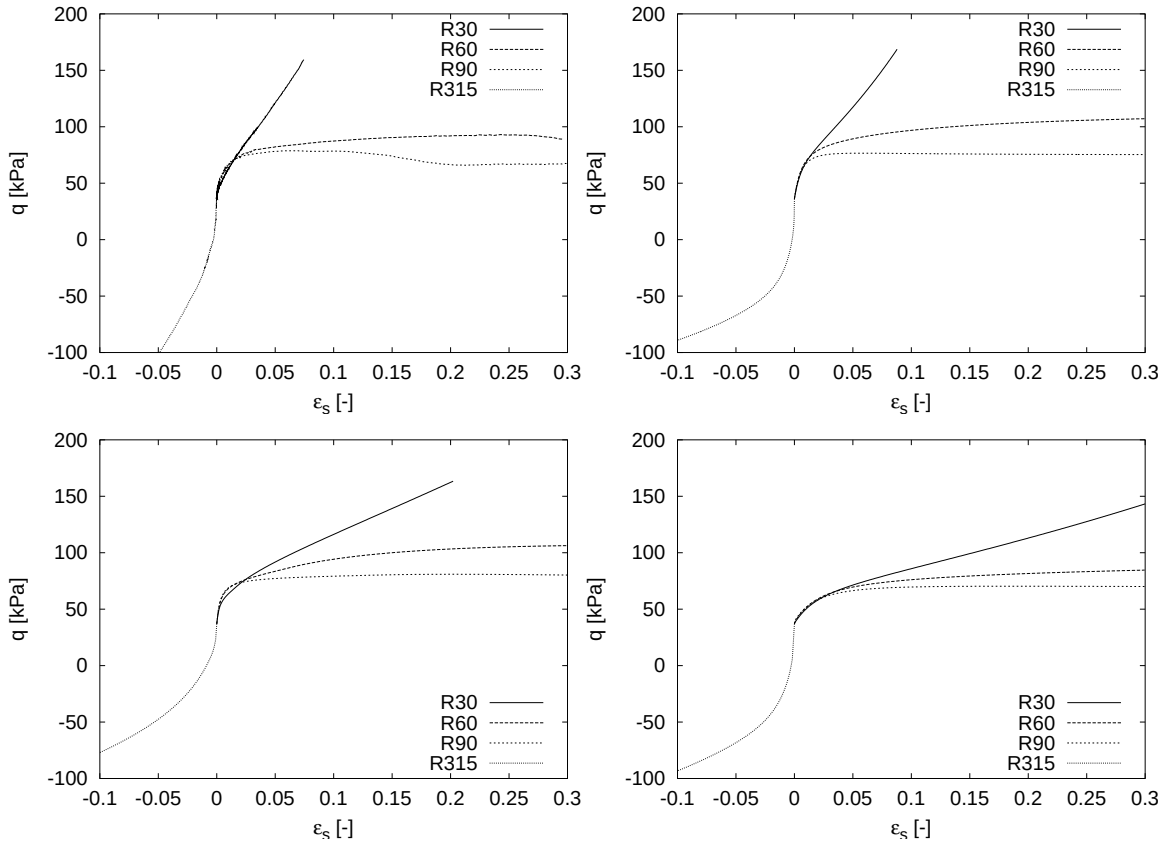

Figure 4.10: *Experimental data after Callisto, 1996 (top left), AI3-SKH model predictions (top right), 3-SKG model run 1 after Baudet, 2001 (bottom left) and 3-SKH model run 2 (bottom right)*

4.2.4 Specific strain energy

The use of specific strain energy as a 'yield' criterion was described in section 2. The contours of equal specific strain energy were plotted for experimental data from tests on reconstituted Pisa Clay (Fig. 4.15) and for the simulation using the AI3-SKH model (Fig. 4.16).

Predictions using the AI3-SKH model are close to the experimental data and the 'rotated' shape of the contours of equal specific strain energy in the direction of the K_0 line is predicted well. These results clearly show that the AI3-SKH model is capable of predicting this phenomenon without introducing rotation of the bounding surface. The predictions by the 3-SKH model, which are not presented here, are very close to the predictions by the AI3-SKH model.

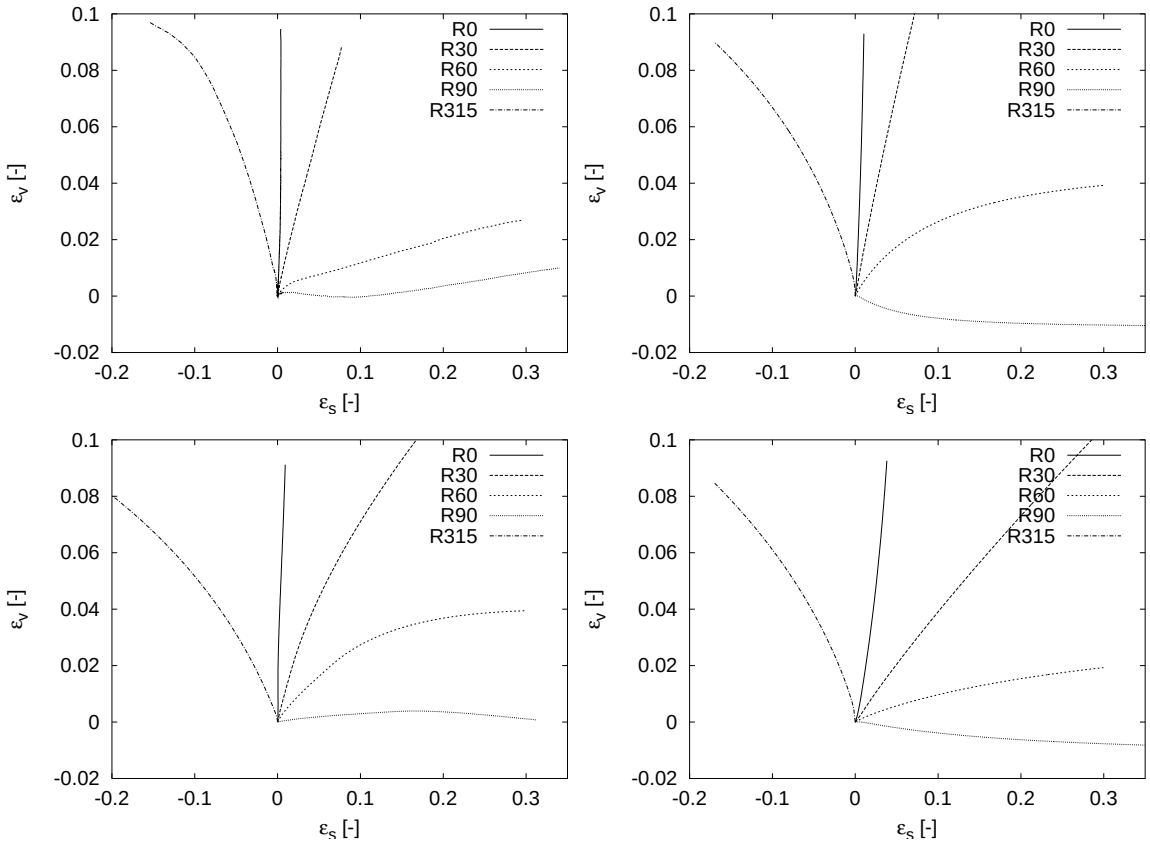

Figure 4.11: *Experimental data after Callisto, 1996 (top left), AI3-SKH model predictions (top right), 3-SKH model run 1 after Baudet, 2001 (bottom left) and 3-SKH model run 2 (bottom right)*

4.3 AI3-SKH model parameters for Speswhite kaolin

In order to perform a finite element study of centrifuge model tests on one–dimensionally consolidated Speswhite kaolin and to make an evaluation of the model on the basis of true–triaxial tests on Spestone kaolin, model parameters were derived. All the parameters derived for the 3-SKH model may be used, except parameter ψ. This parameter has been derived using the same tests as parameters for the 3-SKH model – tests on Speswhite kaolin with different recent stress history performed by Stallebrass (1990). A detailed description of these tests is given in Stallebrass (1990). These are constant p' tests with a stress path rotation of 0° and 180° and an isotropic compression test with a stress path rotation 0° and 180°. Simulations of these tests are shown in Fig. 4.17. The results of simulations are not in perfect agreement with the experiment, however the parameter $\psi = 2.75$ seems to provide the best fit for the experimental data. This value will be used for all subsequent

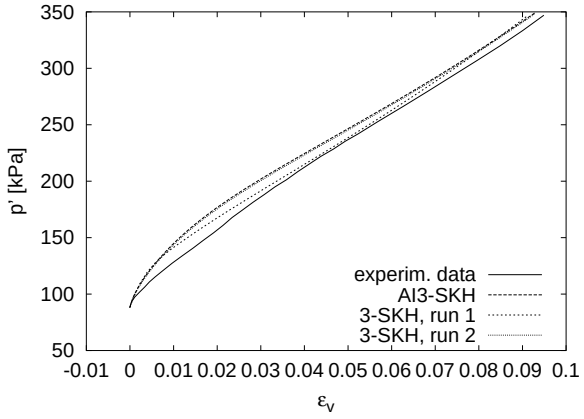

Figure 4.12: p'/ϵ_v *results of the test R0. (3-SKH, run 1 after Baudet, 2001)*

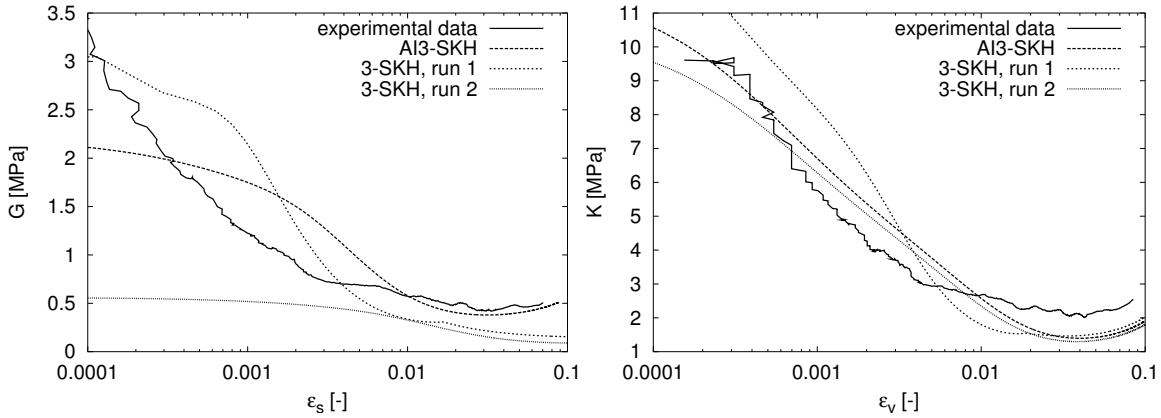

Figure 4.13: *Simulation of the test R30 (exp. data after Callisto, 1996). 3-SKH, run 1, after Baudet (2001)*

finite element simulations of tests on Speswhite kaolin and for evaluation of the model in 3D stress space.

4.4 Modelling the general stress state laboratory tests on Kaolin

This section has been included in order to evaluate the generalisation of the flow rule, defined in triaxial stress space, into 3D stress space.

Two ways of generalisation have been studied:

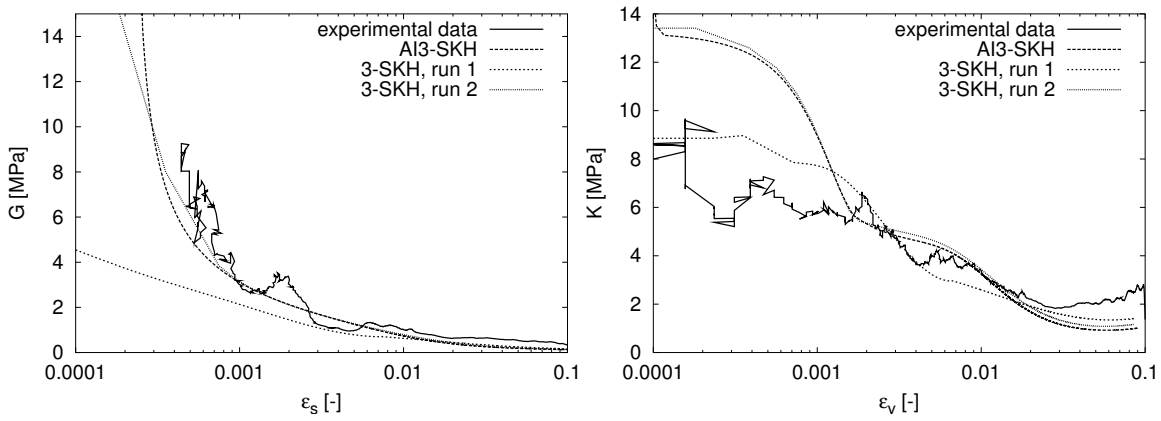

Figure 4.14: *Simulation of the test R315 (exp. data after Callisto, 1996). 3-SKH, run 1, after Baudet (2001)*

1. Isotropic shape with octahedral cross section through the plastic potential surface similar to the cross–section of the yield surface, with different values of M_{fl} in triaxial compression and extension. Direction of the plastic strain increment vector $\boldsymbol{m}$ is calculated by:

$$\boldsymbol{m} = \boldsymbol{g}_{,\boldsymbol{\sigma}} = g_{,\overline{J}_b}\overline{\boldsymbol{J}}_{b,\overline{\boldsymbol{\sigma}}_b} + g_{,\overline{I}_b}\overline{\boldsymbol{I}}_{b,\overline{\boldsymbol{\sigma}}_b} + g_{,\rho_{\left(\overline{\theta}_b,\xi\right)}}\rho_{\left(\overline{\theta}_b,\xi\right),\overline{\theta}_b}\overline{\boldsymbol{\theta}}_{b,\overline{\boldsymbol{\sigma}}_b} \tag{4.1}$$

2. Flow rule which predicts radial plastic strain increment in octahedral plane:

$$\boldsymbol{m} = g_{,\overline{J}_b}\overline{\boldsymbol{J}}_{b,\overline{\boldsymbol{\sigma}}_b} + g_{,\overline{I}_b}\overline{\boldsymbol{I}}_{b,\overline{\boldsymbol{\sigma}}_b} \tag{4.2}$$

Note that in this case it is not possible to define explicitly the plastic potential surface, as the direction of the plastic strain increment vector $\boldsymbol{m}$ is not equal to $\boldsymbol{g}_{,\boldsymbol{\sigma}}$ (the term with the lode dependence is omitted). The type 2 flow rule is in agreement with experiment (ie., predicts radial direction of the plastic strain increments in the octahedral plane) (Sec. 2.2) and has been used in the formulation of the AI3-SKH model.

4.4.1 Description of tests simulated

The tests simulated were p' constant tests with a circular stress path in the octahedral plane (test J6) and a cyclic p' constant test with an increased value of the angular octahedral parameter θ_{oct} in each cycle (I10) performed by Wood (1974) in a computer controlled true triaxial apparatus on isotropically normally consolidated Spesstone kaolin. The value of p'

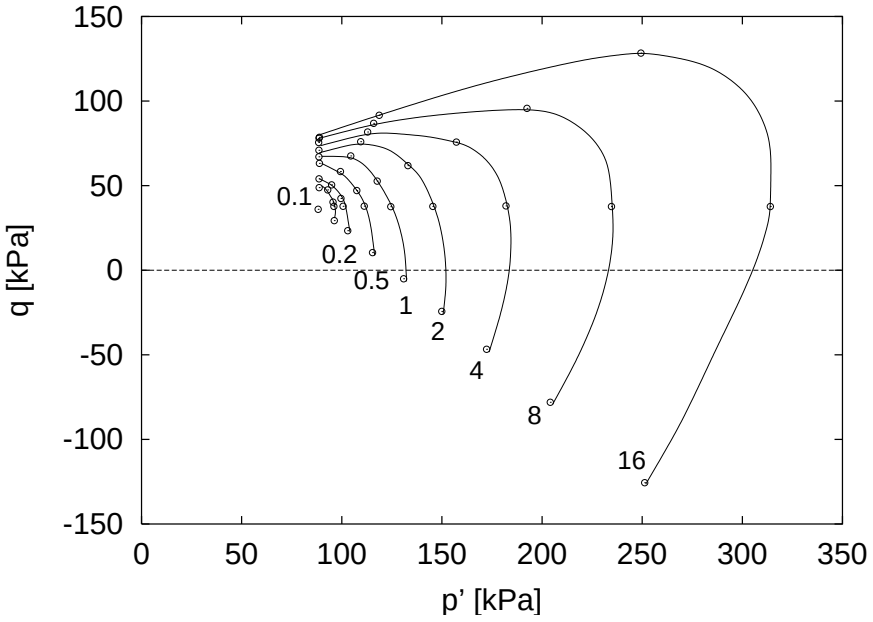

Figure 4.15: *Contours of the equal specific strain energy (in kJ/m^3), experimental data (after after Callisto, 1996)*

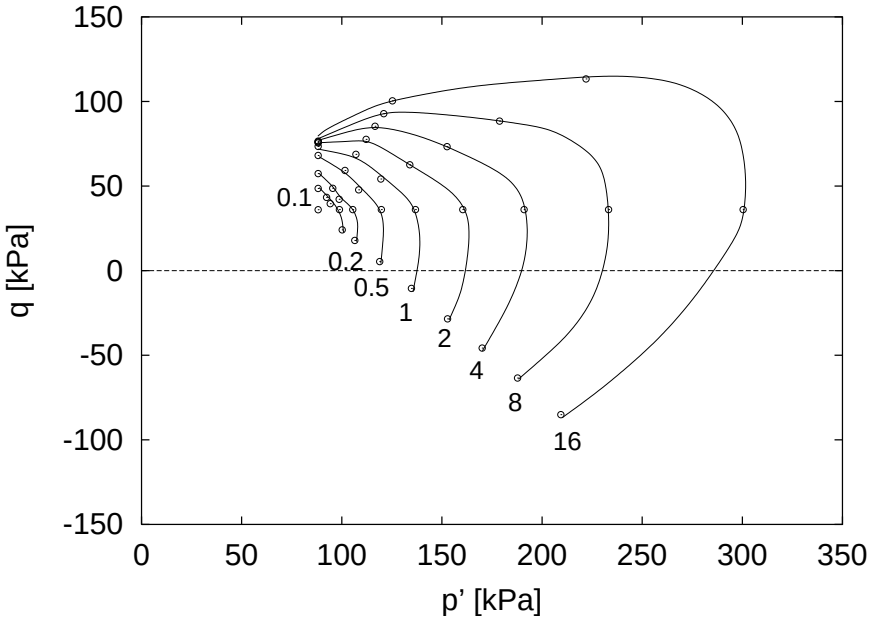

Figure 4.16: *Contours of the equal specific strain energy (in kJ/m^3), simulation by the AI3-SKH model*

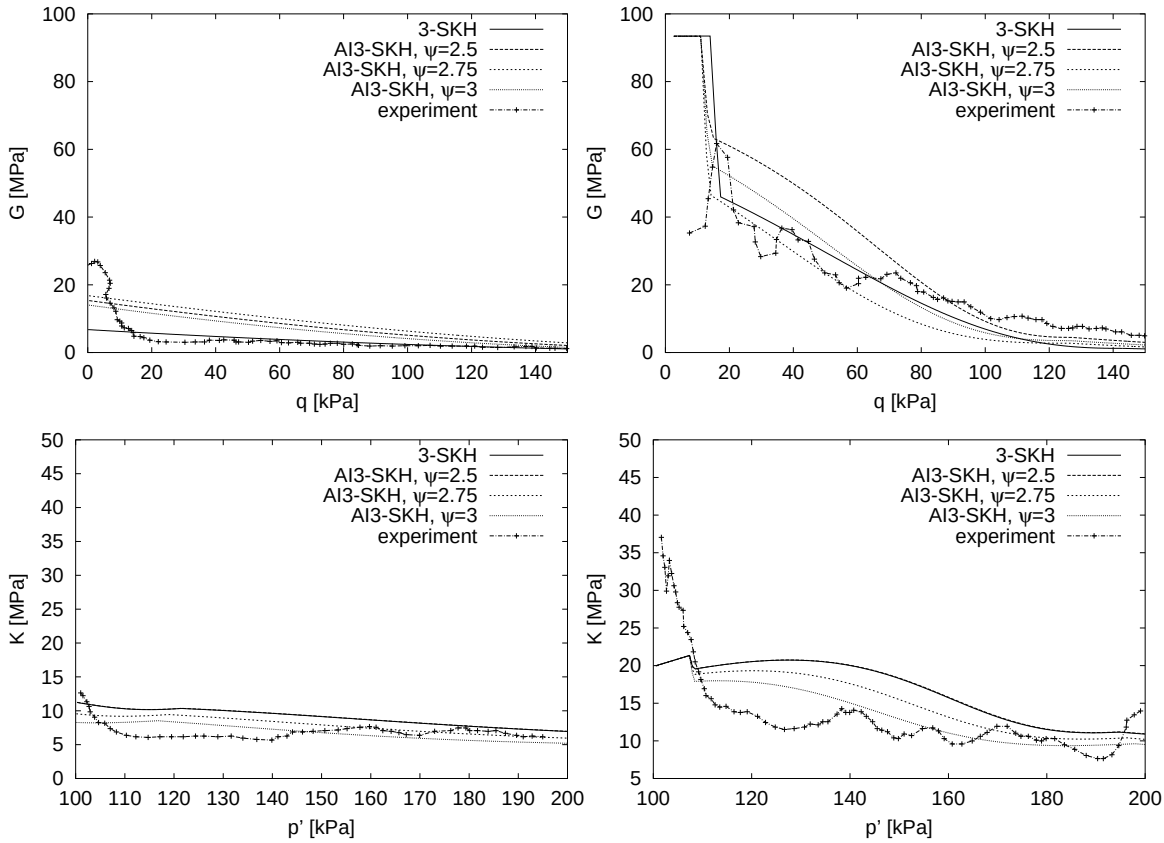

Figure 4.17: *Test data on Speswhite kaolin after Stallebrass, 1990, simulated by the AI3-SKH model. Constant p' test with* 0° *stress path rotation (top left), constant p' test with* 180° *stress path rotation (top right), isotropic compression test with* 0° *stress path rotation (bottom left) and isotropic compression test with* 180° *stress path rotation (bottom right)*

for both tests is 200 kPa.

For true triaxial stress states, where

$$\sigma_{ij} = 0, \quad i \neq j \tag{4.3}$$

The angular octahedral parameter θ_{oct} is defined as

$$\theta_{oct} = \begin{cases} tan^{-1}\frac{\sqrt{3}(\sigma_{33}-\sigma_{22})}{2\sigma_{11}-\sigma_{22}-\sigma_{33}} & \text{for} \quad \sigma_{22} < \sigma_{33} \\ -tan^{-1}\frac{\sqrt{3}(\sigma_{33}-\sigma_{22})}{2\sigma_{11}-\sigma_{22}-\sigma_{33}} & \text{for} \quad \sigma_{22} > \sigma_{33} \end{cases} \tag{4.4}$$

The geometrical interpretation of the parameter θ_{oct}, as well as the stress path of the test

J6 is shown in Fig. 4.18. η is the octahedral stress ratio defined as

$$\eta = 3\sqrt{3}\frac{J}{I} \tag{4.5}$$

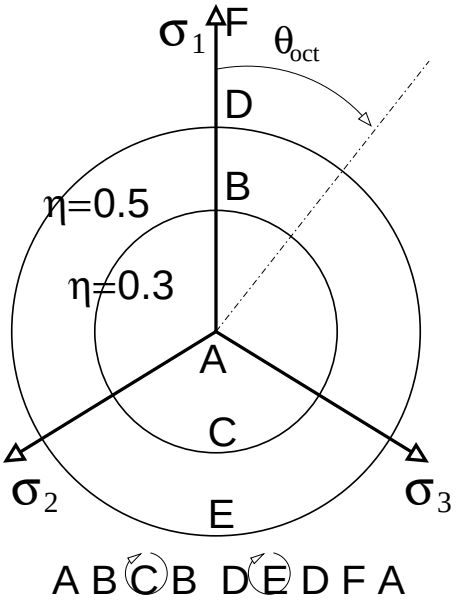

Figure 4.18: *The octahedral stress path of test J6 (after Wood, 1974)*

The octahedral stress path followed in test I10 is shown in figure 4.19.

The parameters used are equal to the parameters of the Speswhite kaolin and are summarised in Table 5.1.

4.4.2 Results of simulations

The stress path for the first circuit ($\eta = 0.3$) and the second circuit ($\eta = 0.5$) carried out during the test J6 with the position of the kinematic surfaces at different stages of the calculation are shown in Figures 4.20 and 4.21 respectively.

The strain path in the octahedral cross-section of the principal strain space for the two flow rules studied is shown in Figure 4.22 (the first circuit of the test J6) and in Figure 4.23 (the second circuit of the test J6).

The stress path of a simulated test I10 with the position of surfaces at different stages of calculation is shown in Figure 4.24.

The octahedral strain path for the part of the test I10, which begins at point C and ends

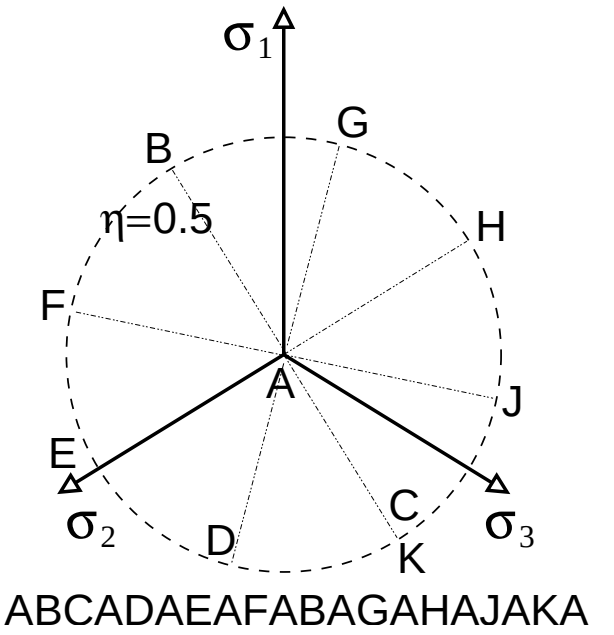

Figure 4.19: *The octahedral stress path of the test I10 (after Wood, 1974)*

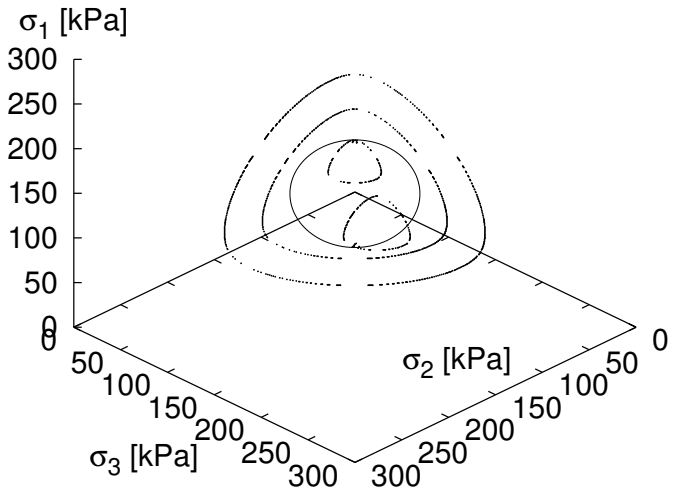

Figure 4.20: *The stress path of the first circuit of the test J6*

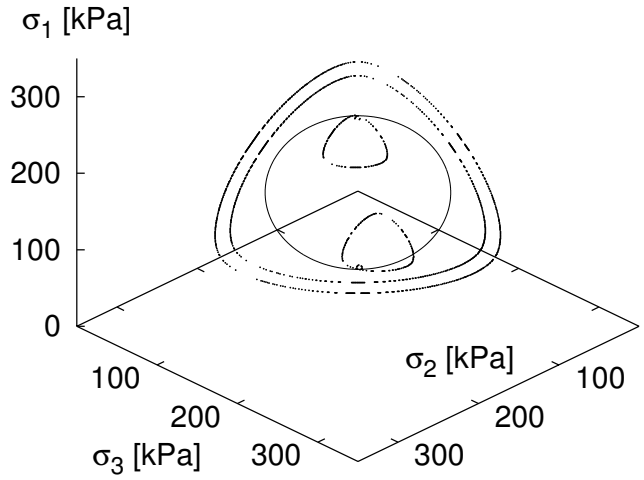

Figure 4.21: *The stress path of the second circuit of the test J6*

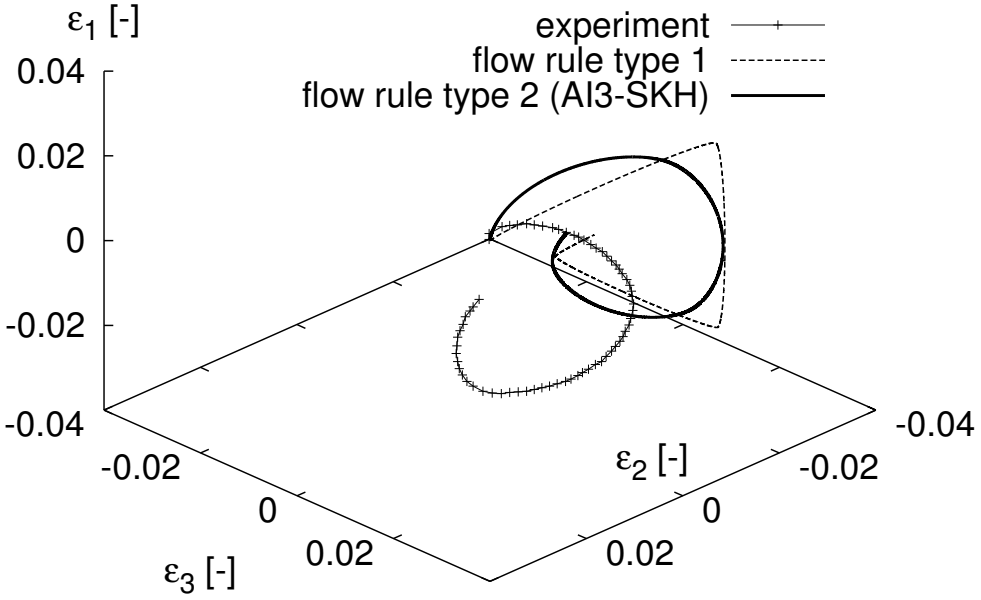

Figure 4.22: *The octahedral strain path of the first circuit of the test J6 (test data after Wood, 1974)*

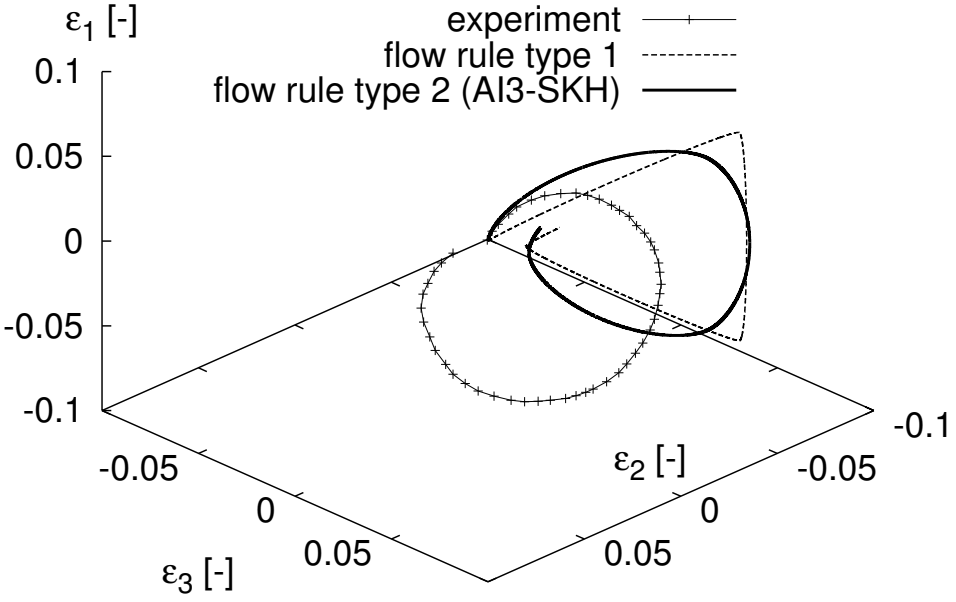

Figure 4.23: *The octahedral strain path of the second circuit of the test J6 (test data after Wood, 1974)*

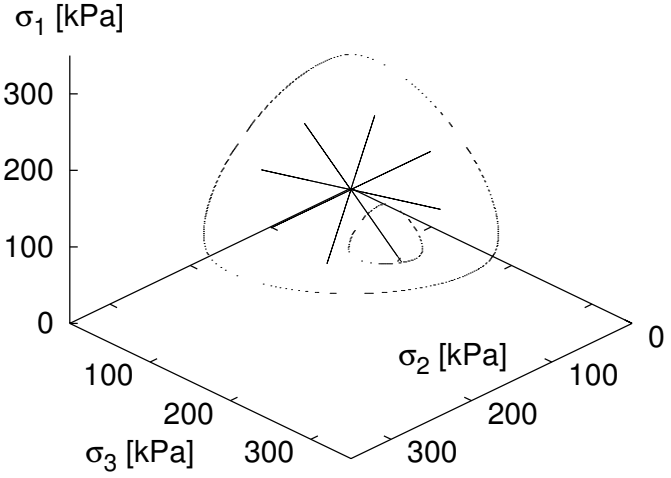

Figure 4.24: *The octahedral stress path of the test I10*

at point K, is shown together with the experimental data in Figure 4.25.

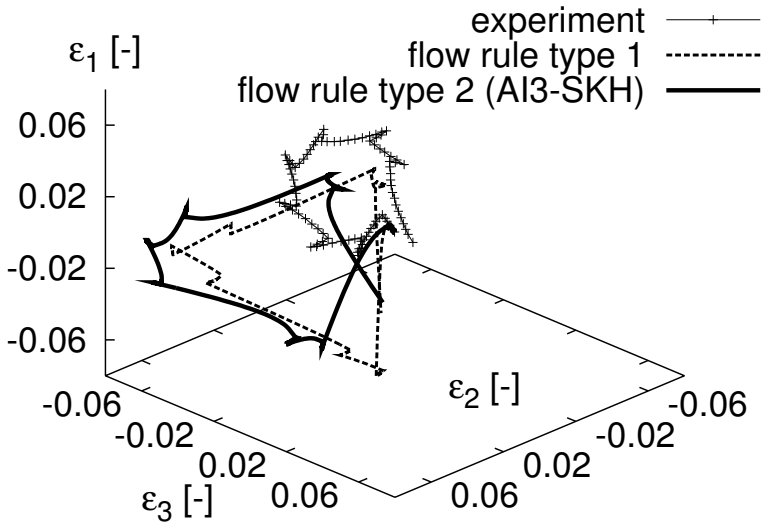

Figure 4.25: *The octahedral strain path of the part of the test I10 (test data after Wood, 1974)*

From simulations of tests J6 and I10 it is clear that the predictions of the model with a radial flow rule in the octahedral plane are closer to experimental data, than the predictions with the flow rule, type 1.

4.5 Summary of evaluation of the AI3-SKH model

- The kinematic hardening approach together with non–associated plasticity allows the use of an experimentally based non–rotated shape for the state boundary surface defined as a boundary of all possible states of clay to predict a 'rotated' shape for the 'yield' surface defined by the bi–linear method or contours of the equal specific strain energy.
- The AI3-SKH model predits the K_{0NC} states in accordance with Jáky's formula. According to experimental evidence given by Richardson (1988) and presented in Section

2, the flow rule of the AI3-SKH is suitable for modelling anisotropic consolidation with any stress ratio.

- The consequence of using the non–associated flow rule is that in accordance with experimental data (Callisto and Rampello, 2002) the large strain shear stiffness in triaxial compression is increased and the stiffness in triaxial extension remains unchanged. Cross–anisotropic elasticity may be incorporated to predict a higher quasi–elastic stiffness in the horizontal direction.

- The formulation of the model does not significantly influence the amount of volumetric strains developed during drained shear (and pore pressures in undrained shear). It therefore does not change the normalised stress paths (in triaxial compression), which are predicted relatively accurately by the 3-SKH model.

- The approximatelly constant critical state friction angle, rather than a constant critical state coefficient M, is predicted by the AI3-SKH model in accordance with experimental data.

- Finally, the suitability of the flow rule assumed by the AI3–SKH model has been demonstrated on the basis of the true triaxial tests on Spesstone kaolin. The flow rule which predicts radial direction of plastic strain increments proved to perform better in comparison with experimental data than the flow rule generalised into 3D stress space in the way which allows to specify explicitly the plastic potential surface.

Chapter 5

Finite element evaluation of the AI3-SKH model

The AI3-SKH model together with the 3-SKH model has been implemented into a finite element program in order to evaluate it with respect to data from boundary value problems in anisotropically consolidated clay (centrifuge model tests). The open source finite element program *Tochnog* (Rodemann, 1998) was used for this purpose. The implementation algorithm which enables the accuracy of the solution to be controlled is first described in this chapter and then the model predictions are evaluated.

5.1 *Tochnog*

Tochnog is an explicit–implicit finite element program which was not developed solely for geotechnical purposes, but nevertheless is able to model all the features which are necessary to simulate complicated boundary value problems, including coupled material – ground water flow equations (Biot, 1941). *Tochnog* uses iterative techniques to solve global finite element equilibrium equations and an option to integrate rate equations with explicit integration schemes has been implemented by the author into a standard distribution of the program. It is also possible to perform three–dimensional simulations of complicated boundary value problems.

Results from *Tochnog* are saved in a format compatible with the pre– and post–processor program *GiD* (CIMNE, 2002).

5.2 Implementation algorithm for the 3-SKH/AI3-SKH model

Plasticity theory assumes infinitesimal load steps and analysis with finite load increments inevitably causes some load path error in the resulting displacements and stresses (Abbo and Sloan, 1996).

The simplest way to implement complicated kinematic hardening bounding surface plasticity models into a finite element program is to use a standard forward Euler scheme. As was pointed out by many authors (e.g., Potts and Gens, 1985) , it is necessary to use very small load increments in order to ensure the accuracy of the solution. Using this method the second, equally serious disadvantage, is that it is not possible to control the accuracy of the integration of the constitutive model. In the case, when the explicit forward Euler scheme is used to solve the global finite element equilibrium equations, and the same technique is adopted at the Gauss point level, global equilibrium may be satisfied at each load step, but there may be an accumulated, uncontrollable error in the integration of the constitutive equation. The finite element analysis must be repeated with increased numbers of load steps until the number of steps does not influence the results of the calculation.

A broad range of different techniques has been proposed to increase the accuracy of the integration of non–linear rate equations. According to Crisfield (Crisfield, 1997), there would appear to be three alternative procedures which can be used, either individually or in combination. They are:

1. Add a return to the yield surface to the 'forward Euler' scheme
2. Use sub–increments
3. Use some form of backward or mid–point Euler scheme

Recent work has seen increasing use of the backward–Euler scheme without sub–incrementation. This method is popular because, for simple constitutive models it has quite a simple form and it allows a 'consistent tangent modular matrix' which ensures quadratic convergence for the overall structural iterations when the full Newton–Raphson method is adopted. Nonetheless, for some complicated yield criteria when coupled with complex hardening laws, the backward–Euler procedure is difficult to implement and hence techniques such as sub–incrementation may still be relevant (Crisfield, 1997).

It has been therefore decided that the substepping technique would be used for the implementation of the AI3-SKH/3-SKH model into *Tochnog*, although it was shown by Rouiana and Wood (2001) that kinematic hardening 'bubble' models may also be integrated using

the implicit backward–Euler procedure. The advantage of the explicit integration method with the aid of substepping is that it allows the direct use of the rate formulation of the model defined in Chapter 3.

The calculation strategy is similar to that proposed by Abbo and Sloan (1996) and Jakobsen and Lade (2002). At the beginning of each step current stresses, history variables, strain increment and material parameters are input by the finite element program. The material model subroutine then produces new stresses, new history variables, an increment of plastic strain and the updated tangent stiffness matrix, the so–called Jacobian matrix.

The calculation strategy is illustrated schematically in Figure 5.1. Based on the current stress, history variables and the new strain increments, stress point B is calculated assuming the strain increment to be entirely elastic. The value of the yield function f is calculated at the stress B. IF $f_B < 0$ then the new stress point B is located inside the yield surface and the strain increment is truly elastic. The calculation for this increment has already been performed and the Jacobian matrix is elastic. On the other hand if $f_B \geq 0$ then point B is outside the current yield surface and a portion of the strain increment is plastic. In this case the program determines, whether the current stress state (point A) is located inside or on the current yield surface.

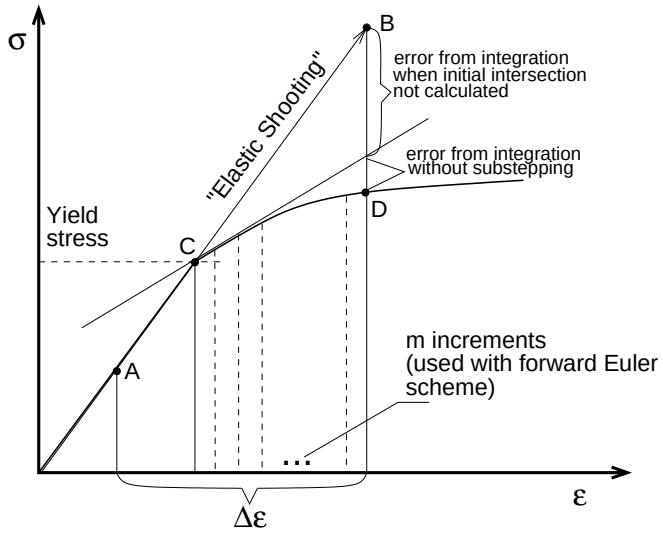

Figure 5.1: *Schematic illustration of stress–strain relation with stress states used in explanation of calculation strategy (after Jakobsen and Lade, 2002)*

If $f_A < 0$ then point A is inside the yield surface (Fig. 5.1). In this case it is necessary to determine the portion of stress path from A to B which is purely elastic (AC) by determining the ratio $\alpha = AC/AB$. If $f_A = 0$ then $\alpha = 0$.

Having calculated the elastic strains from A to C, the remaining portion of the total strain increment ($\Delta\boldsymbol{\epsilon}\,(1-\alpha)$) is used to update stresses and history variables elasto–plastically. A forward–Euler scheme with sub–incrementation and control of the number of substeps on the basis of the local curvature of the stress–strain curve is used for this purpose. At the end the tangent stiffness matrix is calculated at point D and used for the global equilibrium iterations (after Jakobsen and Lade, 2002).

5.2.1 Initial intersection with the yield surface

If $f_A < 0$ and $f_B > 0$ it is necessary to find the point C (Fig. 5.1). The 'elastic shooting' from A to B produces an elastic trial stress increment

$$\Delta\boldsymbol{\sigma}^e = \boldsymbol{D}^e_{(\boldsymbol{\sigma}_A)}\Delta\boldsymbol{\epsilon} \tag{5.1}$$

where $\boldsymbol{D}^e$ is defined in Equation 3.18. The strategy used to define the scalar multiplier α is illustrated in Figure 5.2. A first estimate may be determined by a simple linear interpolation in f:

$$\alpha_0 = -\frac{f_A}{f_B - f_A} \tag{5.2}$$

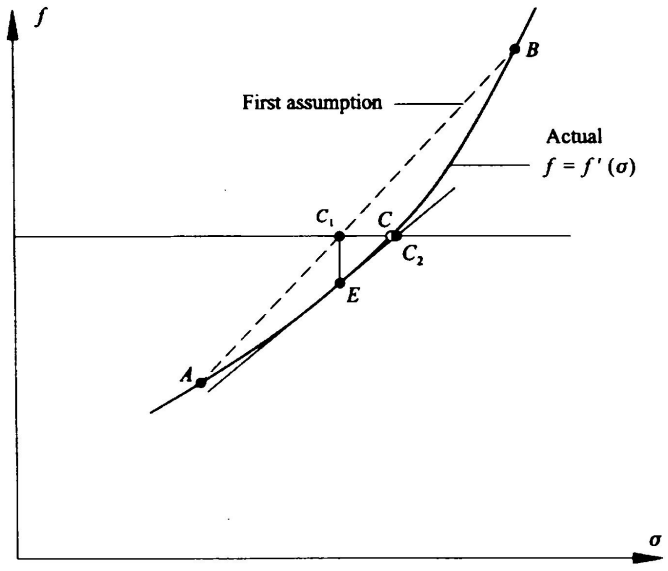

Figure 5.2: *Schematic illustration of technique for finding intersection with yield surface (Jakobsen and Lade, 2002)*

The yield function is, however, highly non–linear and the scalar estimate determined by

Egn. 5.2 will generally not satisfy the yield criterion. A more accurate estimate for α may be obtained by a Taylor series expansion around point E:

$$\alpha = \alpha_0 - \frac{f_E}{\boldsymbol{f}^T_{,(\boldsymbol{\sigma_A}+\alpha_0\Delta\boldsymbol{\sigma}^e)} : \Delta\boldsymbol{\sigma}^e} \tag{5.3}$$

This approach will be accurate for small strain increments only. In order to avoid any initial yield surface drift in the integration schemes it is advisable to apply an iterative scheme. A Newton–Raphson technique was adopted and the multiplier α and stress at point C are updated as follows:

$$\begin{aligned}
&\text{Initial state } \boldsymbol{\sigma}_A;\ \alpha_0 \\
&\text{Iterations } i = 1, 2, \ldots, i_{max} \\
&\qquad \boldsymbol{\sigma}_i = \boldsymbol{\sigma}_A + \alpha_{i-1}\Delta\boldsymbol{\sigma}^e \\
&\qquad \Delta\alpha_i = \frac{f_{(\boldsymbol{\sigma}_i)}}{\boldsymbol{f}^T_{,\boldsymbol{\sigma}_i} : \Delta\boldsymbol{\sigma}^e} \\
&\qquad \alpha_i = \alpha_{i-1} + \Delta\alpha_i \\
&\qquad \text{Stop iterations when } 0 < f_{(\boldsymbol{\sigma}_i)} < f_{limit} \\
&\text{Final state } \boldsymbol{\sigma}_C = \boldsymbol{\sigma}_i;\ \alpha = \alpha_i
\end{aligned} \tag{5.4}$$

f_{limit} is typically set to a very small number. In the case of the implementation of the AI3-SKH/3-SKH model into *Tochnog* $f_{limit} = 10^{-5}$ and $i_{max} = 40$. Preliminary analyses have shown that the condition $0 < f_{(\boldsymbol{\sigma}_i)} < f_{limit}$ is usually fulfilled after few iterations.

5.2.2 Updating stresses and history variables

As already pointed out, the forward–Euler integration scheme is only accurate for small strain increments. By subdividing the strain increment into a number of sub–increments and updating the stresses and history variables in each substep the accuracy will be improved (Sloan, 1987). In order to ensure computational efficiency, the number of sub–increments should be controlled and a larger number of sub–increments used only in 'problematic' areas.

It is therefore necessary to estimate the number of sub–increments that are required to produce a solution of specified accuracy. The key idea is to use two integration schemes, whose order of accuracy differs by one. The difference between the higher order solution and lower order solution provides an estimate of the local truncation error for the current step size (Abbo and Sloan, 1996). Probably the simplest possible technique was first proposed by Wissman and Hauck (1983). They use two forward–Euler solutions, first with

one full–size strain increment (leads to stress $\boldsymbol{\sigma}_I$) and second two half–size sub–increments ($\boldsymbol{\sigma}_{II}$). This technique, demonstrated in Figure 5.3, was adopted for the AI3-SKH/3-SKH model. The scalar norm of the difference between $\boldsymbol{\sigma}_I$ and $\boldsymbol{\sigma}_{II}$ is the measure of the local truncation error (ERR).

$$ERR = \sqrt{(\boldsymbol{\sigma}_I - \boldsymbol{\sigma}_{II}) : (\boldsymbol{\sigma}_I - \boldsymbol{\sigma}_{II})} \tag{5.5}$$

The required number of sub–increments is calculated only once at the beginning of the main step. It is assumed that the local curvature of the stress–strain curve is approximately equal throughout the whole strain increment. The strain increment is subdivided into two equal sub–increments, the value of ERR is calculated and if it is larger than the specified tolerance ($DTOL$), the first sub–increment is used as the main step for the next subdivision. This is repeated until $ERR > DTOL$ (initially, the error measure ERR is larger than the tolerance $DTOL$). When $ERR \leq DTOL$ is achieved, the rest of the strain increment is calculated using $(\Delta\boldsymbol{\epsilon}/\Delta\boldsymbol{\epsilon}_{final} - 2)$ number of subincrements ($\Delta\boldsymbol{\epsilon}_{final}$ is the size of the smallest substep). Obviously, the number of substeps obtained by this method is always an integer power of 2.

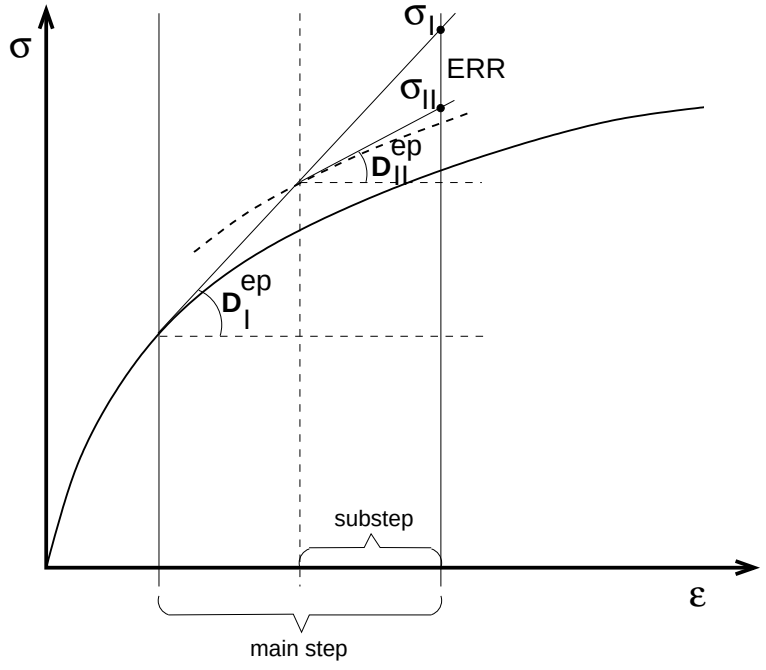

Figure 5.3: *Illustration of the control of the local truncation error*

The accuracy of the forward–Euler method may be improved by adopting one of the methods which scale the current stress back to the yield surface. Several different methods have

been described in Potts and Gens (1985). The correct methods need to take account of the change in the proportion of the plastic and elastic strain in the total strain increment and when applied with the kinematic hardening models are rather complex, because the plastic strains necessarily cause the movement of surfaces. Therefore no methods to correct the drift from the yield surface were adopted in the case of the AI3-SKH/3-SKH model implementation. Instead, only the distance of the current stress state from the yield surface is checked by plotting the value of the yield function f. Ideally $f \leq 0$, but actually very small positive values of f will be achieved. The calculation is accepted only if f does not exceed some limiting value in all elements. It is worth addressing that the value of the yield function f gives only qualitative measure of accuracy, as in addition to the distance of the current stress point from the yield surface it depends also on its size. Differences of the value of f in neighbouring elements, or its sudden increase with the course of simulation, however allow to discover problems in the time–integration of the constitutive model.

Substepping controlled by the local truncation error, together with a subsequent check of the value f, leads to accuracy of the numerical integration of the constitutive model, which can be controlled.

5.3 Simple triaxial test problem

A simple 'single element' triaxial test was simulated as a boundary value problem in order to demonstrate the advantages of the implementation of the models and to define suitable values of parameters, which are used to control the calculation (DTOL, number of global steps). This problem was chosen because the 'exact' solution to the problem can be obtained from a single–element program. The single–element program *Triax*, used in this thesis for all single–element simulations, adopts a simple Forward–Euler integration scheme with a large number of increments to achieve sufficient accuracy of the solution. The test was modelled using a simple axi–symmetric mesh (Fig. 5.4) with 8 three–noded triangles, using a gauss integration rule with one integration point per element (in the centre). Initial conditions were $p' = p_a = p_b = 100$ kPa, $q_a = q_b = 0$ kPa and $p_0 = 80$ kPa. The specimen was loaded with strain control up to an axial strain of 10 %. The AI3-SKH model was used with the values of model parameters derived for Boom Clay (Tab. 4.1). A reference solution was obtained using a single element program with 50000 forward Euler steps. 2 global iterations were used because preliminary analyses had shown that beyond this number the improvement in solution was negligible.

The influence of two parameters, which control the calculation, has been investigated: The

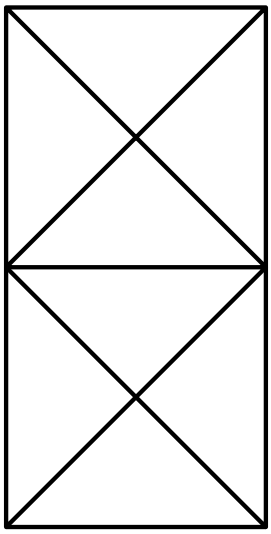

Figure 5.4: *Finite element mesh for a simple triaxial test problem*

value of prescribed maximum local truncation error $DTOL$ and number of global steps. The accuracy of the solution, CPU time, number of substeps and the value of the yield function f (which to some extent reflects the accuracy of the model integration) have been compared.

For the first set of analyses the number of global increments has been set to 500 and $DTOL$ has been varied. Stress–strain plots for different values of $DTOL$ are shown in Figure 5.5. For $DTOL < 0.005$[1] the solution was sufficiently close to the exact solution to ensure the accuracy of the finite element analysis. Further investigation has shown that the optimal value of DTOL is between between approximately 10^{-4} and 10^{-5}, since for higher values an oscillation of the number of substeps leads to an increase in the CPU time. For subsequent analyses, $DTOL$ has been fixed to 10^{-5} and the influence of the number of global increments has been examined.

Comparison of the stress–strain curves obtained for different numbers of global increments is given in Figure 5.6. Already for 50 global increments the solution is sufficiently close to the exact solution. Examination of the number of substeps shows that the program automatically decreases the number of substeps with increasing number of global increments in order to keep the prescribed accuracy of the integration of the constitutive model. For less than 50 global increments the error comes from the lack of global equilibrium.

The number of increments is controlled by the local curvature of the stress–strain curve.

[1] Units of $DTOL$ are kPa, but in the text they are omitted

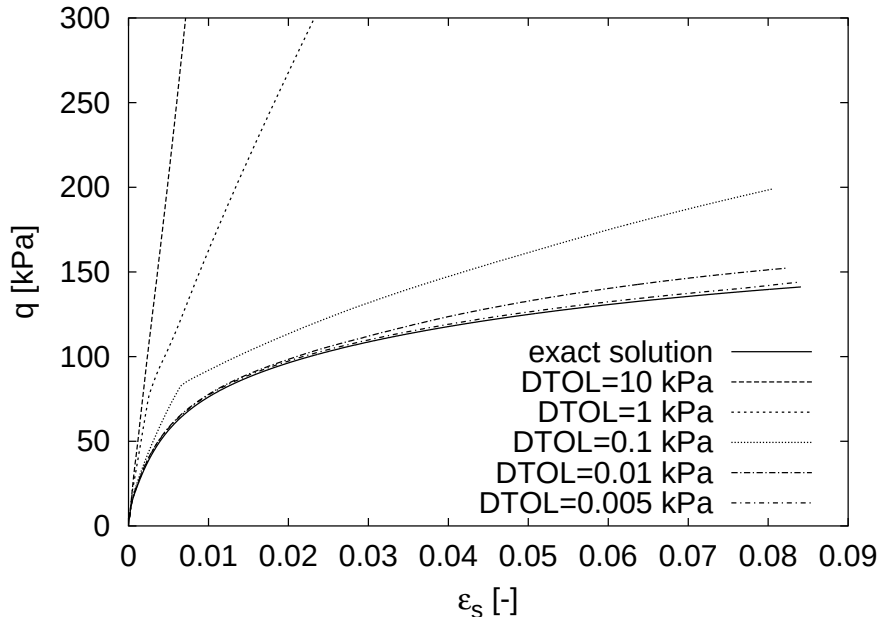

Figure 5.5: *Stress–strain curve for different values of parameter DTOL. Number of global increments fixed to 500.*

The model requires small increments also for the proper translation of kinematic surfaces and this may cause problems in the case of linear stress–strain relationship (e.g. one–dimensional loading). It is therefore advisable to check the value of f and additionally to prescribe also minimum or fixed numbers of substeps in the case when f becomes increasingly large.

5.4 Simulations of the centrifuge model test

The centrifuge model test has been simulated in order to study the suitability of the AI3-SKH model for predictions of boundary value problems. Also the control of the accuracy of the solution is demonstrated in this section.

The problem analysed is one of a series of centrifuge tests of a tunnel excavated in one-dimensionally consolidated kaolin clay performed by Grant (1998). A detailed description of the centrifuge test, as well as the analysis procedure adopted is given in Grant (1998) and Ingram (2000). In order to avoid duplication, only the analysis procedure is described here in order to ensure repeatability of the calculations.

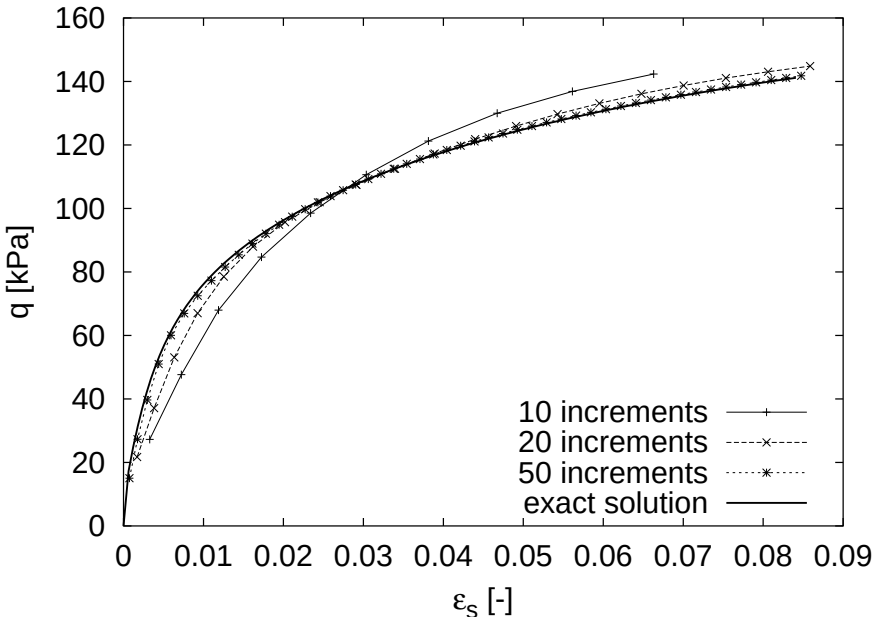

Figure 5.6: *Stress–strain curve for different number of global steps. DTOL fixed to* 10^{-5}.

5.4.1 Analysis procedure

In order to study the dependence of the solution on the finite element discretization, different finite element meshes, types of elements, integration rules, steps sizes and numbers of equilibrium iterations were used, as described in subsection 5.4.2. The initial state was in the case of simulation by the 3-SKH and AI3-SKH models calculated according to Jáky's formula $K_{0NC} = 1 - \sin\phi$. This state can be achieved by simulating K_0 loading from slurry only with the AI3-SKH model. The initial axial stress was 500 kPa and the soil was swelled in a consolidometer to $\sigma_{ax} = 250$ kPa. This stage was simulated as fully drained with an assumption of a homogeneous stress state throughout the sample. This allowed this stage to be modelled in a single element program and the results to be used to initialise the stresses and the positions of surfaces in *Tochnog*. Subsequent stages were calculated in the finite element program using a fully coupled consolidation analysis (Biot, 1941). The mesh was constrained by the following boundary conditions:

	Displacement	Pore pressure
Top	Free	Impermeable
Left	Zero horizontal	Impermeable
Right	Zero horizontal	Impermeable
Bottom	Zero horizontal and vertical	Zero excess
Tunnel	Free	Impermeable

The calculation was subdivided into three main stages:

1. Increasing the g–level in the centrifuge

This stage was modelled over a very long period of time to ensure effectively drained conditions (the calculated excess pore pressure was of the order 10^{-5} kPa). It has been assumed that the excess pore pressure, caused by the unloading in the centrifuge, dissipates gradually as the g–level is increased. Therefore, the 250 kPa surcharge (after unloading in the consolidometer) was removed gradually over the same period of time, as the g–level was increased. The final acceleration was 100g. Zero hydrostatic pore pressure was as in the experiment 25 mm below the surface. Fixed mesh coordinates and no rotation of stress axes has been assumed.

2. Modelling the tunnel excavation

Unlike in the experiment and following Grant (1998) and Ingram (2000), the tunnel was not excavated after the model was removed from the consolidometer. The soil was first accelerated in the centrifuge and then the nodal forces which acted around the circumference of the tunnel were gradually replaced by the nodal forces caused by the air pressure in the tunnel membrane (tunnel elements were deleted over a long period of time and over the same time nodal forces from the air in the membrane were gradually increased and added to the forces in the nodes around the circumference of the tunnel). The air pressure in the membrane at the end of stage 2 was 304.4 kPa. This was again performed over a long period of time with effectively drained conditions. The nodal coordinates were fixed in space, but the co–rotated part of the stress tensor was not neglected.

3. Reducing the tunnel support pressure

At this stage the tunnel support pressure was gradually decreased over the same period of time as in the experiment. The pressure was reduced at a rate of approximately 100 kPa

per minute (total time was 183 s). The position of nodal coordinates has been updated and stress axes co–rotated to take into account of rigid body rotation.

Material parameters

Material parameters used are summarised in Table 5.1. They were taken from Grant (1998) and Ingram (2000). The derivation of the parameter ψ for the AI3-SKH model is described in Section 4. Other parameters are the same for both the 3-SKH and AI3-SKH models. C_w is a product of porosity and the bulk modulus of water and is typically a very small number (water almost incompressible). The parameters, which control the calculation (step sizes, substepping tolerance $DTOL$ etc.) are summarised in Section 5.4.3.

Speswhite kaolin										
	A	n	m	M	κ^*	λ^*	T	S	ψ	N
3-SKH	1964	0.65	0.2	0.89	0.005	0.073	0.25	0.08	2.5	1.1
AI3-SKH									2.75	

Speswhite kaolin			Water		Other
k_v (m/s)	k_h (m/s)	γ (kN/m^3)	γ_w (kN/m^3)	C_w	g (m/s^2)
$0.7 * 10^{-9}$	$1.8 * 10^{-9}$	17.5	9.81	10^{-9}	9.81

Table 5.1: *Parameters for finite element simulations of the tunnel problem in Speswhite kaolin*

5.4.2 Finite element discretization

Two different finite element meshes were used for the calculations: the mesh taken from Grant (1998) and a mesh prepared in the pre–processor *GiD*. These meshes are shown in Figures 5.7 and 5.8 respectively. The width of the mesh is 27.5 cm, height 25.5 cm, the tunnel axis is 17.5 cm below the surface and the tunnel diameter is 5 cm. The aim was to use lower order elements in order to save CPU time. Theoretically even a three–noded triangle with one Gauss point in the centre is suitable for undrained analysis under plane strain conditions (Sloan and Randolph, 1982).

To study suitable element types three different analyses were performed. One reference analysis with a large number of increments (1800), six–noded elements with six integration points (Lobatto integration rule) and the mesh prepared in the pre–processor *GiD* and two other analyses with less degrees of freedom.

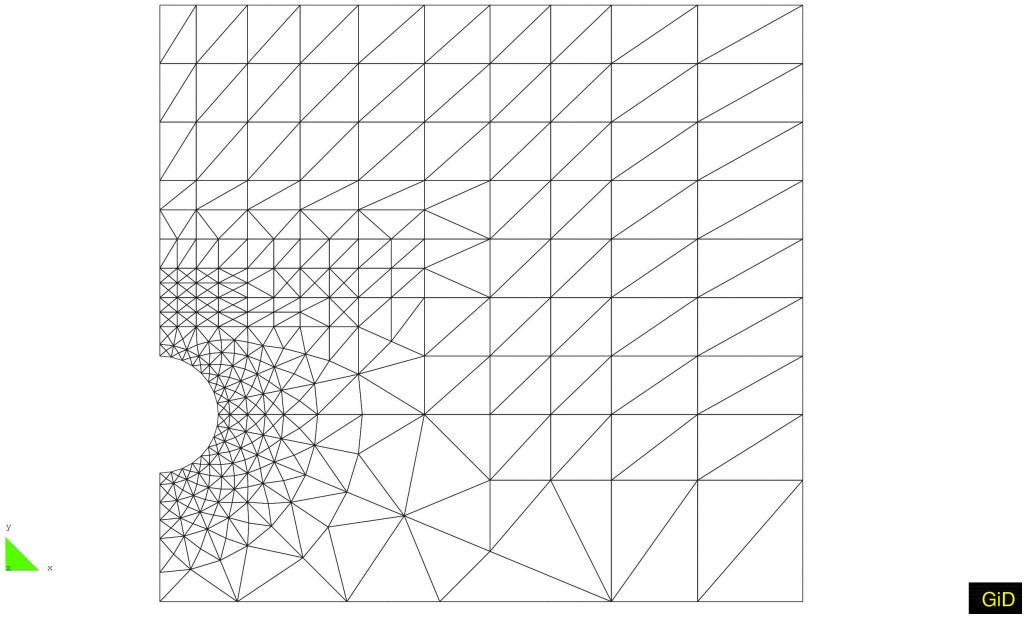

Figure 5.7: *Finite element mesh after Grant (1998)*

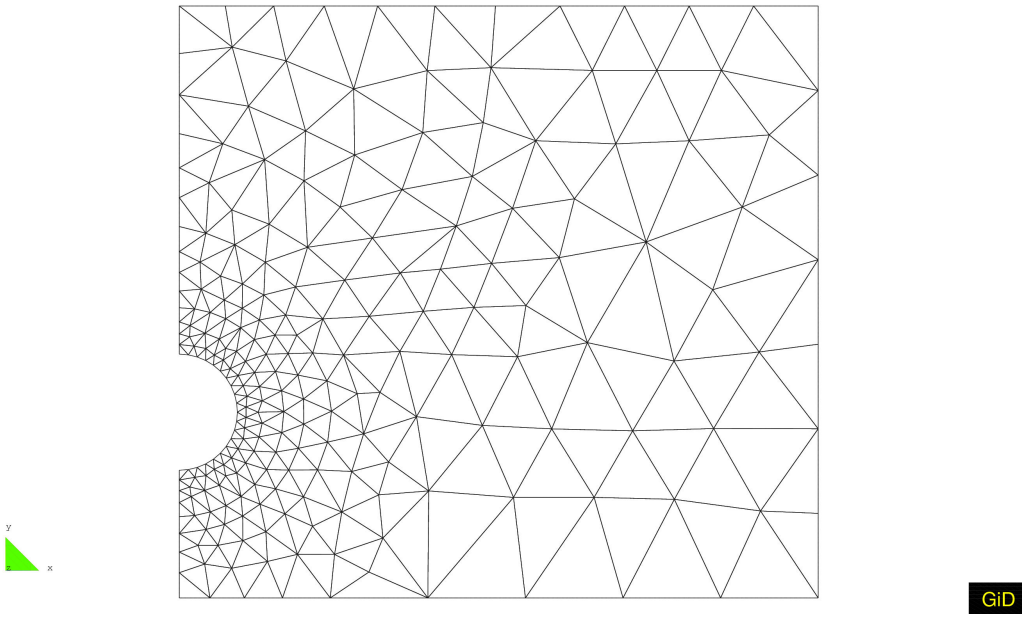

Figure 5.8: *Finite element mesh prepared in preprocessor GiD*

The resultant graphs of settlement above the tunnel axis with respect to the reduction of the tunnel support pressure is shown in Figure 5.9 (note that the analysis with six–noded triangles was stopped prematurely at 65% of the reduction of the tunnel support pressure, because the large number of increments, together with the tight tolerance $DTOL$ made the calculation very time consuming). Calculation results were very similar, therefore, the

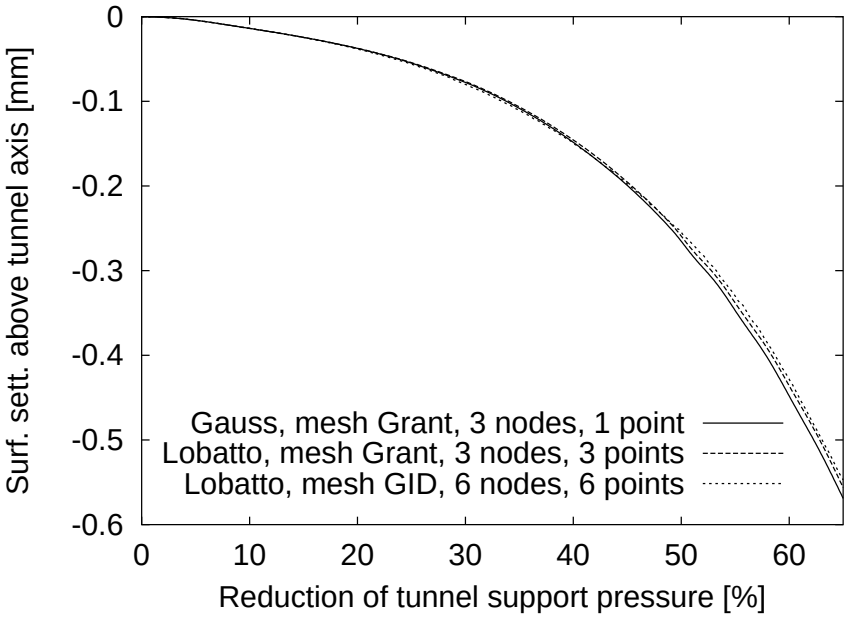

Figure 5.9: *Predictions of the settlement above the tunnel axis for three different element types*

mesh type with the least number of degrees of freedom (mesh after Grant with three–noded triangles, one integration point and Gauss integration rule) was adopted for subsequent analyses.

5.4.3 Control parameters and the accuracy of the solution

A number of preliminary analyses were performed in order to set the optimum values of control parameters. If not otherwise stated, 2 equilibrium iterations were performed at each time step.

1. Increasing the g–level in the centrifuge Pure K_0 conditions were applied to the soil at this stage, therefore this stage was calculated using a fixed number of substeps (200) for all integration points. 200 global steps were used for the calculation of this stage.

2. Modelling the tunnel excavation This stage was calculated with the number of substeps controlled by the local truncation error ($DTOL = 10^{-5}$) in 500 global increments.

3. Reducing the tunnel support pressure Parameter $DTOL$ has been set to 10^{-4} at this stage, because a tighter tolerance led to an increasingly high number of substeps close to the tunnel collapse. This tolerance is sufficient to ensure accuracy of model integration, as shown in Section 5.3. The calculation was performed over the same time as the experiment – 183 s. The first 90 s were calculated using a step of 0.5 s, the subsequent 54 s with a step of 0.2 s and the last 39 s with the step 0.1 s. In the last 39 s 3 global iterations were used at each time–step. The tunnel collapsed and small increments with larger number of iterations were necessary in order to satisfy the global equilibrium.

The measure of the unbalanced forces, `post_node_rhside_ratio`, used by the program *Tochnog*, was of the order 10^{-4} throughout the simulation, increasing to 0.005 close to the 100% reduction of the tunnel support pressure. According to the authors of the finite element program *Tochnog* (Rodemann, 1998), acceptable values of `post_node_rhside_ratio` are between 0.01 and 0.001.

The accuracy of the solution is demonstrated by plotting values of the yield function f (Fig. 5.10). The maximum achieved value of f is approximately 0.08. The yield surface for the

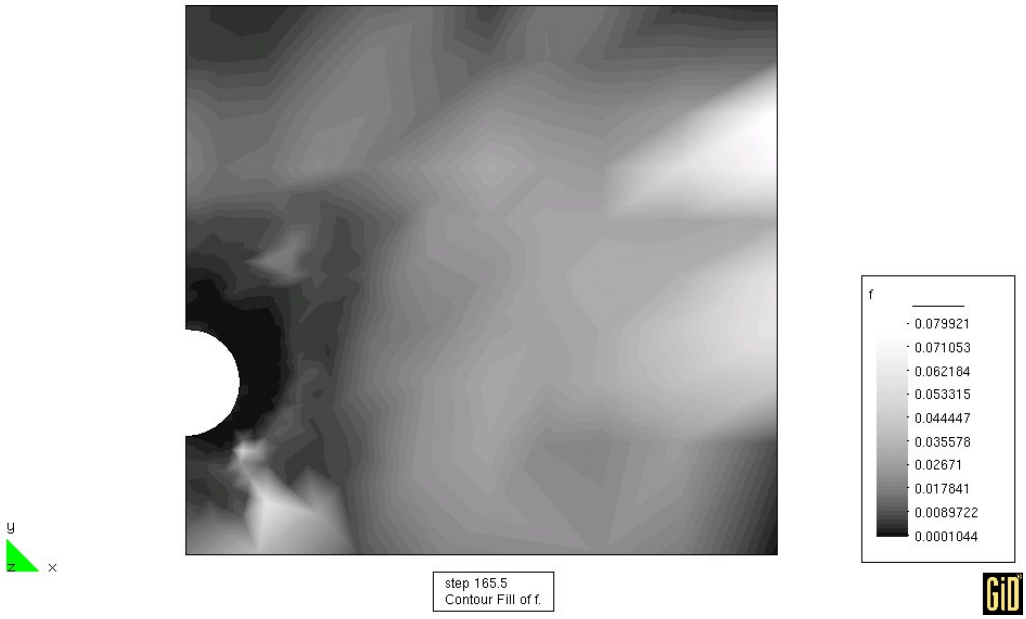

Figure 5.10: *The values of the yield function f for the typical analysis with the AI3-SKH model at 89% reduction of the tunnel support pressure*

AI3-SKH model parameters for kaolin with some stress states outside the yield surface and corresponding values of yield function f were plotted in Figure 5.11 to demonstrate the accuracy (the size of the yield surface in Fig. 5.11 represents its size in a depth of the tunnel centreline at the beginning of simulation).

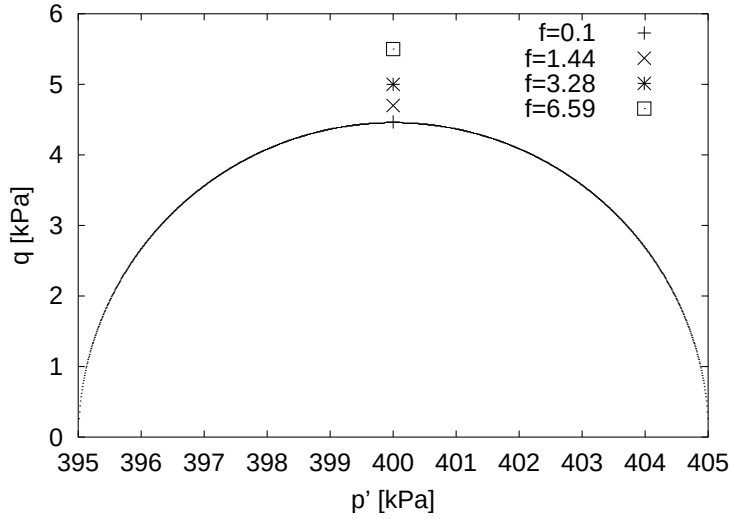

Figure 5.11: *The values of the yield function f for the AI3-SKH model parameters for several stress states outside the yield surface*

5.4.4 Comparison of two finite element programs

The same experiment by Grant (1998) as modelled here was simulated by Grant (1998) and Ingram (2000) using the 3-SKH model implemented into the version of the finite element program *CRISP* (Stallebrass, 1992). This allows the results obtained from two different finite element programs to be compared for a boundary value problem with a rather complicated stress history. Because the simulation of *CRISP* was performed using the fixed mesh and non–corotated stress axes, one additional analysis with the 3-SKH model was performed in *Tochnog* under the same conditions.

A comparison of surface settlement above the tunnel axis with respect to the reduction of the tunnel support pressure is shown in Figure 5.12 for the reduction 0%–65%. Clearly, results of both programs are very similar, if one takes into account that the calculation strategy is very different (*CRISP* is an explicit incremental finite element program, whereas *Tochnog* is an iterative program with explicit model integration with the aid of substepping techniques). Nevertheless, for the pressure reduction close to the collapse (5.13) the results

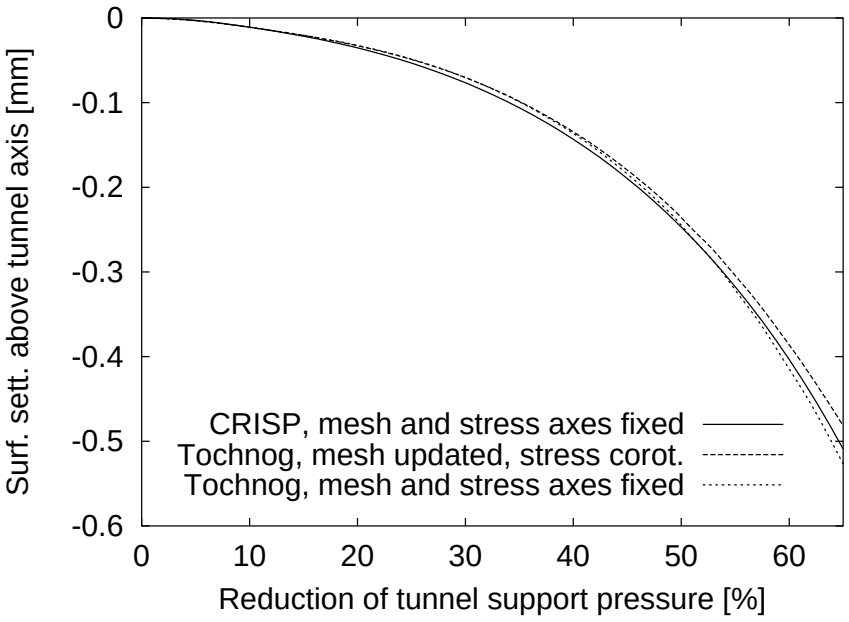

Figure 5.12: *Comparison of predictions of the finite element programs Tochnog and CRISP up to 65% of tunnel pressure reduction*

of both programs start to differ, *Tochnog* predicts larger settlements at 100% of the tunnel support pressure reduction. Close to the collapse large deformations occur in the vicinity of the tunnel and a possible reason for this discrepancy is that the model integration in *CRISP* starts to be less accurate without the aid of a substepping method (or other more advanced method for the constitutive model integration). The number of substeps required to keep the prescribed error tolerance *DTOL* is shown for an 89 % reduction of the tunnel support pressure in Figure 5.14 (the AI3-SKH model).

The calculation results with updated mesh coordinates and co–rotated stress are close to the collapse substantially different compared to the fixed ones and therefore it seems that it is not possible to neglect mesh deformation and stress rotation.

5.4.5 Comparison of the AI3-SKH/3-SKH model predictions with the experiment

Simulations with the 3-SKH model and the AI3-SKH model are compared to experimental data for the reduction of support pressure–settlement curve in Figure 5.15 (up to 75% reduction) and 5.16 (up to 100%). At the small tunnel pressure reductions the predictions of both models are very similar and both overpredict the surface settlement. This is possibly

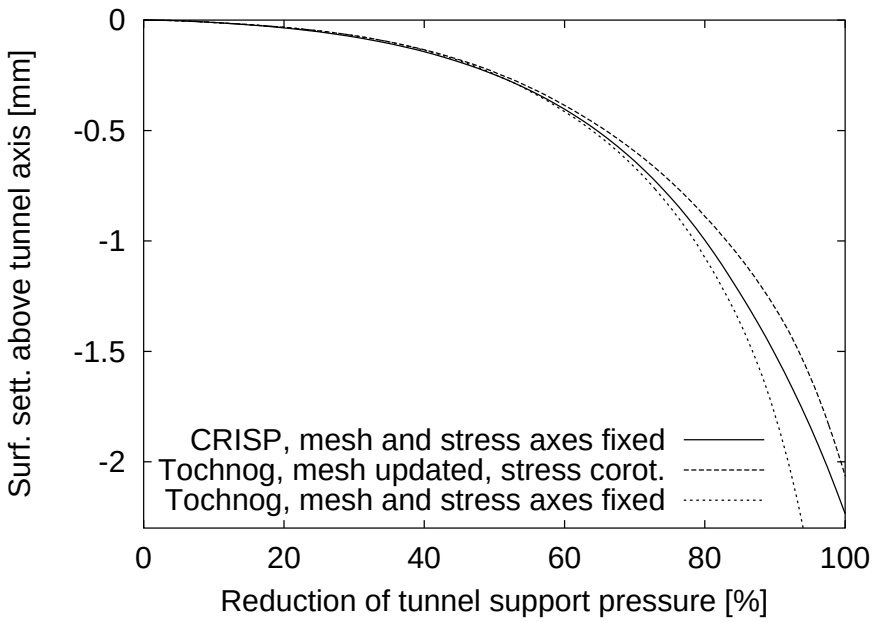

Figure 5.13: *Comparison of predictions of the finite element programs Tochnog and CRISP up to 100% of tunnel pressure reduction*

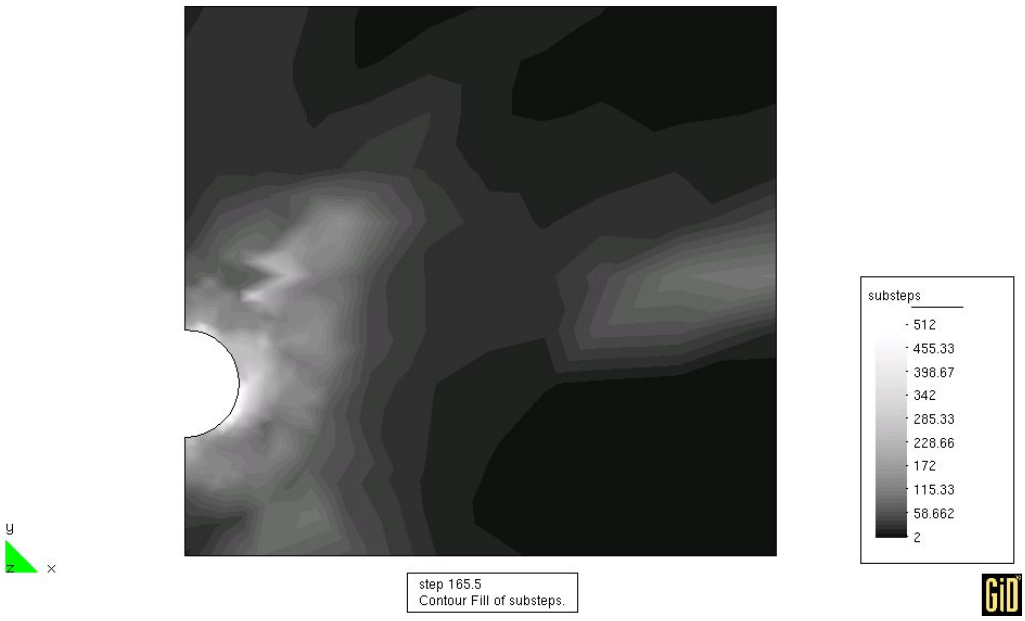

Figure 5.14: *Required number of substeps to keep the prescribed tolerance DTOL at 89% reduction of the tunnel support pressure for the AI3-SKH model*

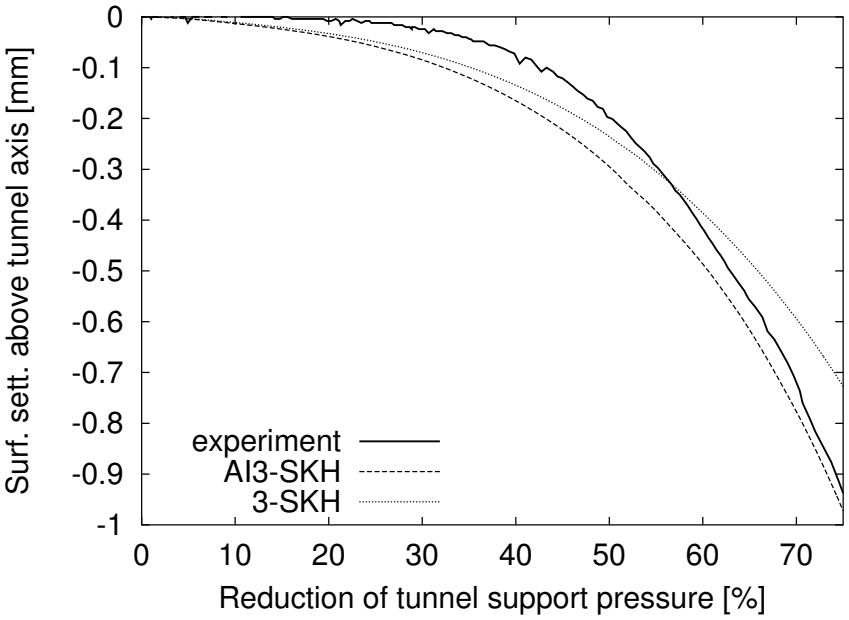

Figure 5.15: *Settlement above the tunnel axis as predicted by the AI3-SKH model, 3-SKH model in comparison with experimental data (up to 75% reduction of tunnel support pressure). Experimental data from Grant, 1998*

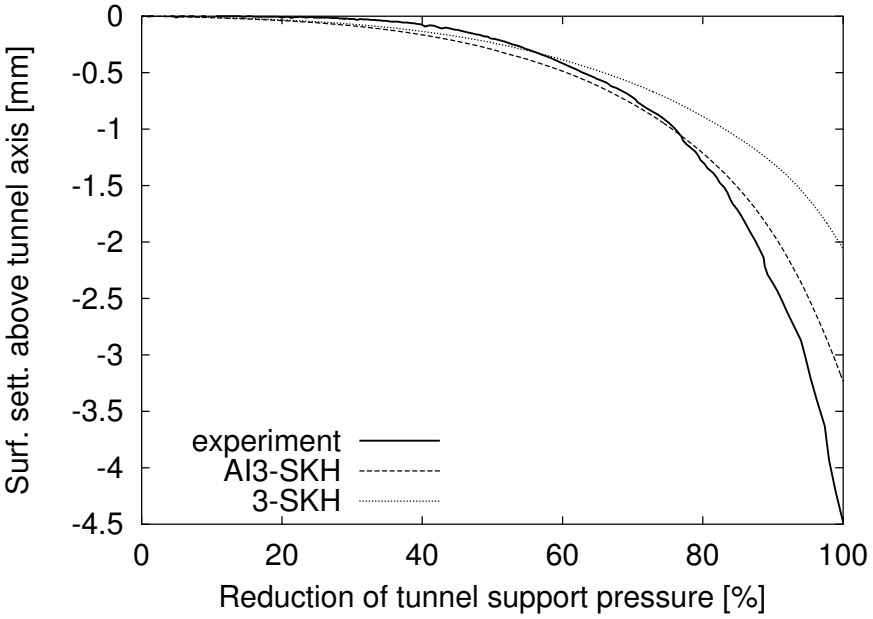

Figure 5.16: *Settlement above the tunnel axis as predicted by the AI3-SKH model, 3-SKH model in comparison with experimental data (up to 100% reduction of tunnel support pressure). Experimental data from Grant, 1998*

because the parameter ψ was in the case of both models calibrated on the basis of the same tests in the small–strain stiffness range. The AI3-SKH model leads to more accurate predictions of the collapse settlement, as seen in Figure 5.16. Here the failure criterion, rather than the small strain stiffness behaviour, influences the results significantly.

The excess pore pressure, measured in the experiment at the location of transducer b1 (Grant, 1998) is compared with that simulated by both models in Figure 5.17. The pore pressure transducer was located 42.7 mm from the tunnel axis and 20 mm below the tunnel axis vertically. Predictions by both the 3-SKH model and AI3-SKH model are relatively

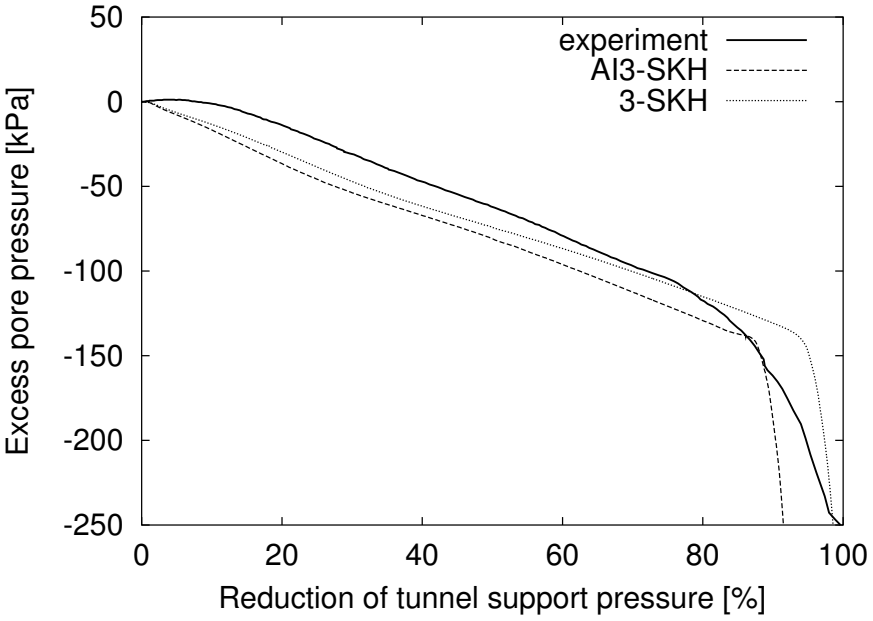

Figure 5.17: *Measured and calculated excess pore pressure in transducer b1 (experimental data from Grant, 1998)*

accurate.

The predicted and observed normalised surface settlement profiles for 60% reduction of the tunnel support pressure are given in Figure 5.18 and data for settlement troughs at 100% reduction in Figure 5.19. The normalised settlement profile at 60% shows that the predictions by both models are very similar. The predicted normalised settlement trough is wider than observed in the experiment. The overprediction of settlement trough width by the finite element analysis has been observed by many other researchers, even when constitutive models which can describe small–strain stiffness behaviour accurately are used (e.g., Addenbrooke et al., 1997; Grammatikopoulou at al., 2002; Grant et al., 1996). The

surface settlement profile after the tunnel collapse (100% pressure reduction) is predicted relatively accurately by the AI3-SKH model.

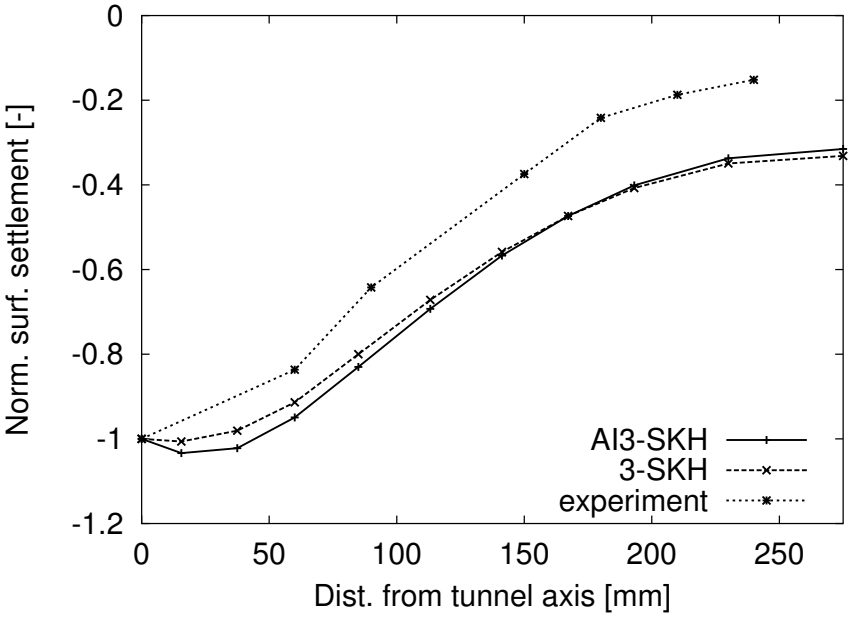

Figure 5.18: *Normalised surface settlement profile at 60% pressure reduction. Experimental data after Grant, 1998.*

5.5 Conclusions for Finite Element evaluation

- The implementation algorithm adopted enables the accuracy of the integration of a constitutive model to be controlled and increases the efficiency of analyses.
- In order to control the accuracy the user of the finite element program must check if equilibrium is satisfied on a global level. In addition, a qualitative measure of the accuracy of the model integration is provided by the value of the yield function f, which is also advisable to check.
- Comparison of predictions by the AI3-SKH model and the 3-SKH model has shown that the AI3-SKH model is capable of predicting the behaviour of geotechnical structures close to the collapse better than the 3-SKH model. Before collapse the solutions predicted by both models do not differ significantly.

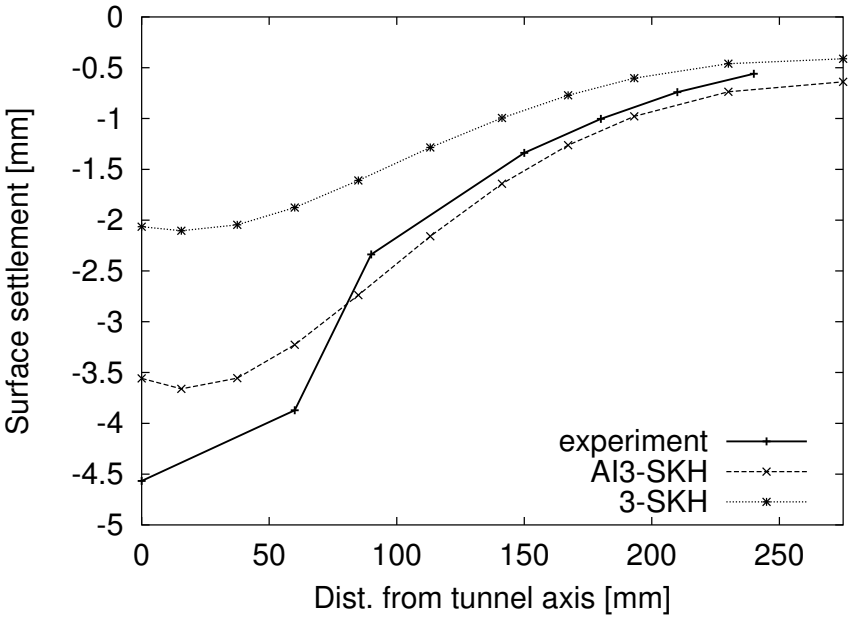

Figure 5.19: *Surface settlement profile at 100% pressure reduction. Experimental data after Grant, 1998.*

Chapter 6

Structured clays

The modified constitutive model for prediction of anisotropic states has been formulated and evaluated in previous chapters. This modification was necessary for the proper modelling of natural clays. This chapter summarises a framework for the behaviour of natural clays, because this framework is key to the approach adopted for modelling natural clay using a constitutive model developed for reconstituted clay. The experimental data on artificially sedimented clays available in the literature are reviewed in this chapter.

6.1 Sensitivity framework

Some ideas for the sensitivity framework were put forward by Burland (1990) and further work by Cotecchia (1996) and Cotecchia and Chandler (1997) led to the publishing of an integrated 'sensitivity' framework by Cotecchia and Chandler (2000). This framework, as well as the experimental evidence for it has been extensively referred to during previous research at City University on natural clays with 'stable' structure (Ingram, 2000) and 'unstable' structure (Baudet, 2001). It is not necessary to repeat this literature survey, nevertheless it is worth summarising the main conclusions:

1. Burland (1990) has demonstrated that the isotropic normal compression line (NCL) of reconstituted clay is a valuable reference line for studying the compression characteristics of natural normally consolidated and overconsolidated sedimentary clays. If this line is plotted in terms of void index I_v it forms a unique line (named intrinsic compression line, ICL) for most clays of medium sensitivity.

2. There is a direct relationship between the isotropic NCL and Atterberg limits. It is

possible, for a given clay, to estimate the position of the isotropic normal compression line on the basis of liquid limit. The intercept N (the value of $\ln v$ on the isotropic NCL at $\ln p' = 0$) is higher for a higher liquid limit.

3. Cotecchia and Chandler (2000) have demonstrated that the sensitivity ratio of the natural clay, is reasonably equal when defined either in terms of undrained shear strength for natural and equivalent reconstituted clay or stress at K_0 or isotropic yield. There is a geometric similarity between the state boundary surface for natural and the equivalent reconstituted clay. The ratio of their sizes defines *sensitivity*, S_t.

4. If data are normalised with respect to sensitivity, specific volume and critical state stress ratio M, it appears that there is a unique shape of the state boundary surface for all clays. This shape is more vertically elongated than the state boundary surface predicted by the Modified Cam–Clay model.

5. It is possible to define two main types of natural structure: 'unstable' structure, which degrades during plastic loading and compression such that sensitivity ratio S_t decreases, and 'stable' structure, for which the sensitivity S_t remains constant (or at least it is reasonable to assume that S_t remains constant over the applied stress range).

Several problems were encountered, when this framework was applied to natural clays:

1. More advanced numerical models take into account the fact that the behaviour of clays is dependent on the stress history of a soil element. The stress history of natural clay is however usually uncertain. It has been shown (Ingram, 2000) that the stress history assumed significantly influences predictions of behaviour of geotechnical structures. Additionally, time–dependent processes, such as creep, may make direct comparison between natural and reconstituted clays even more difficult, because they change the size of the state boundary surface (e.g., Ingram (2000)).

2. It is also not clear, to what extent other characteristics of the soil behaviour such as elastic, or quasi–elastic stiffness, rate of degradation of stiffness during plastic shearing and other defined on the basis of tests on reconstituted clays are applicable to natural clays.

It is possible to investigate these points if a clay with natural structure is prepared under controlled conditions in a laboratory by processes similar to these that occur in nature (sedimentation). In the case of such a clay, the stress history is known and experiments

are quick enough to ensure that time dependent processes do not influence the behaviour significantly. Previous work on this field is reviewed in section 6.2.

6.2 Preparation of artificial structure in clays

This review examines previous attempts to create a structure similar to natural structure in the laboratory. Because most of the experimental data were published before the sensitivity framework had been developed some results are re–examined in terms of the sensitivity framework outlined above. According to Leroueil et al. (1985) it is possible to define four states of structure: intact, destructured, remoulded and resedimented. Burland (1990) indicates that the fifth important state, which is used as a reference state, is reconstituted. The resedimented state is often omitted by researchers, because preparation of specimens take a considerably longer time. Nevertheless, studies on artificially sedimented clays offer an interesting insight into the development of structure in natural clays.

As discussed by Locat and Lefebvre (1985) there are many factors controlling the type of natural structure formed during deposition. Most important are temperature, chemical composition of pore fluid, initial density of a slurry, sedimentation rate and the mineralogy and organic content of the clay.

It appears that the first laboratory study on artificially sedimented clays was published by Bjerrum and Rosenqvist (1956). The clay studied was a sensitive Norwegian marine clay. Three sets of experiments were performed. In two sets the specimens were sedimented from a dilute slurry in salt water. Clay in the first set remained untouched after sedimentation and in the second case the salty water was leached by applying a hydraulic gradient. It took 18 months to reduce the pore–water salinity from the initial 35 g/l to a final 5 g/l. The overall time taken for the experiments was 2.5 years. In the third set of experiments specimens were prepared in fresh water at an initial water content of 150%.

Several interesting observations were made:

1. The addition of salt led to a significant increase of the liquid limit from 28% to 41.5% (48.8% after 2 years).

2. The initial specific volume of leached and unleached specimens was practically the same.

3. Sensitivity, defined in terms of the undrained shear strength obtained from a vane–shear test, significantly increases with leaching from 5 for the unleached specimen to

110 for the leached specimen.

4. Fresh water clay was characterised by a dense structure with a lower water content. The sensitivity of the fresh water clay was about 5–6, almost identical with the unleached salt water specimen.

5. The liquid limit of the fresh water and leached samples was the same (28%).

6. The undrained shear strength of the remoulded leached specimen is much smaller than the undrained shear strength of the remoulded salty clay and the remoulded fresh water specimen.

Because there is a direct relationship between w_L and the normal compression line (Burland, 1990), the normal compression line of the salt water specimen is shifted to the right with respect to the fresh water specimen and is the same for the leached and fresh water specimens. Leaching did not cause degradation of the flocculated open structure of the salt water specimen, but probably caused this structure to be very unstable. Some structure has developed even in the fresh water specimen (sensitivity 5). The salt content after leaching (5 g/l) is not high enough to cause flocculation of clay particles in remoulded samples, both leached and fresh water specimens have the same ICL. Sedimentation caused an increase in the specific volume (compared with the same clay remoulded), but the influence of the pore water chemistry was more pronounced.

One possible explanation of all these results using the sensitivity framework is in Fig. 6.1. For simplicity expected results of one-dimensional compression tests performed on specimens prepared by Bjerrum and Rosenqvist (1956). This picture illustrates the influence of chemical composition and sedimentation on the mechanical behaviour these artificially structured clays.

Another study on artificially sedimented clay is described in Locat and Lefebvre (1985) and Locat and Lefebvre (1986). They used Grande–Baleine marine clay from Québec, Canada, with a natural sensitivity of about 300. This clay has been geologically lifted up from marine environment and is naturally leached with an actual salinity of about 0.5 g/l. Clay has been sedimented in water with salinities of 0.2 and 35 g/l. Clay particles sedimented at 35 g/l flocculated during sedimentation, whereas at 0.2 g/l they were dispersed. Preliminary tests have shown that a salinity of about 0.5 g/l created a transition zone between flocculation and dispersion.

Locat and Lefebvre (1985) observed that the liquid limit increases with salinity. Sensitivities determined from undrained shear strength measurements on specimens consolidated

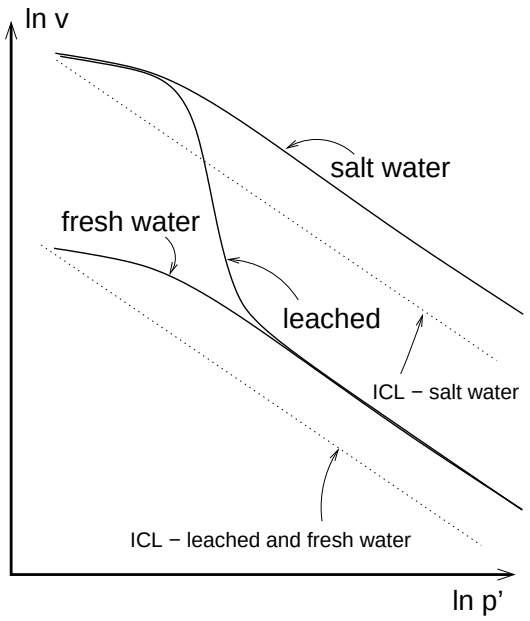

Figure 6.1: *Sketch of expected results of K_0 compression tests on specimens prepared by Bjerrum and Rosenqvist (1956)*

at an axial stress of 50 kPa which is similar to the *in situ* stress and measured by the Swedish cone, are greater for soils of low salinity. e - $\log \sigma$ curves are shown in Fig. 6.2. At $\sigma = 50$ kPa the void ratio of specimens sedimented in salt water and fresh water is similar (compared to the difference of the void ratio of the intact soil), being slightly higher for salt water. $e : \log \sigma$ curves for both specimens merge at high stresses with this curve for the intact soil. It may be seen from Fig. 6.2 that the structure of natural clay is highly unstable, whereas the structure of clay sedimented in fresh water is relatively stable, little destructuration occurs for the salt water clay. Because the ICL of the salt water salt clay is shifted to the right of the ICL of the fresh water clay and the initial void ratio (at 50 kPa) is approximately the same, sensitivity is greater for soil of low salinity.

As discussed by Locat and Lefebvre (1986), the sedimented specimen is less structured (has lower sensitivity) than the corresponding natural specimen. Processes such as creep or bonding in the natural specimen may have caused this difference.

The properties of artificially sedimented calcium illite have been studied by Olson (1962). Commercially available pure illite was chosen, because it is the dominant clay mineral in many clays (e.g. London Clay). The specimens were prepared using sedimentation from dilute suspension in 0.55 g/l $CaCl_2$ solution, which ensures flocculation, as well as reconstitution at a different water content, but with the same pore water chemistry. As

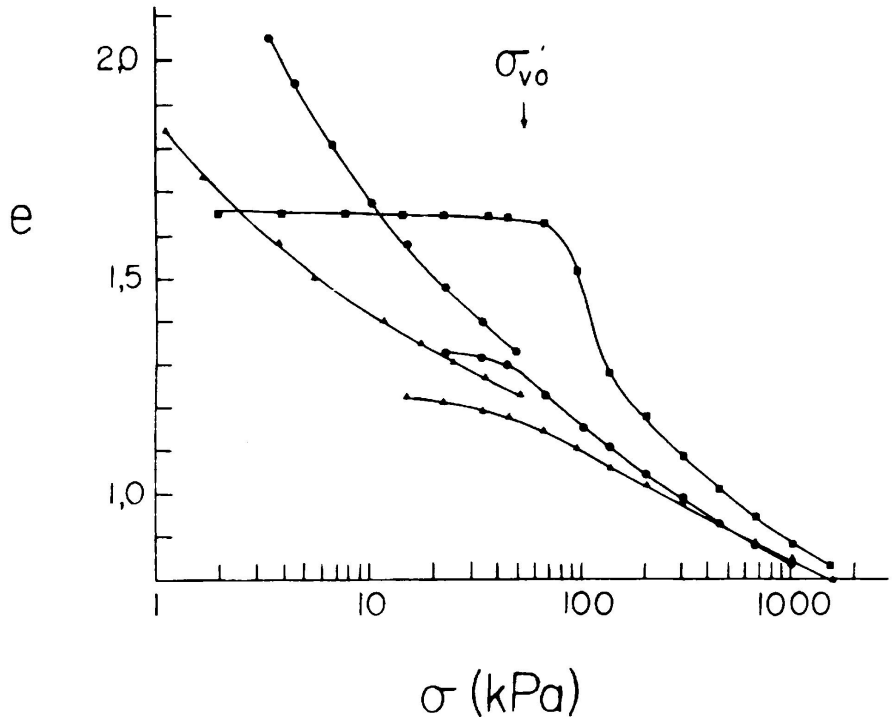

Figure 6.2: *Void ratio–pressure curves of the Grande–Baleine clay for intact soil (squares), sedimented soils at 0.2 g/l (triangles) and 35 g/l (circles) – Locat and Lefebvre, 1985*

may be seen from Fig. 6.3, higher initial water contents lead to higher initial void ratios but all curves converge at higher stresses. Shear strength properties were also studied by undrained triaxial tests. It was found that the failure envelope was unique regardless of the initial void ratio, but the pore water pressures were significantly higher for sedimented samples at all degrees of overconsolidation. As may be seen in Fig. 6.3, the structure caused by sedimentation seems to be slightly unstable and these positive pore water pressures may be explained by destructuration during shearing.

Monte and Krizek (1976) performed a sedimentation study on kaolinite slurry with an initial water content four or five times the liquid limit. Three different chemical compositions were used for the pore water in order to achieve flocculation and dispersion. Both initial and final void ratios were similar for all pore water chemistries, being highest for the weakly flocculated specimen (distilled water), smaller for the flocculated specimen (NaCl) and smallest for the strongly dispersed specimen (NaOH). These results are different from other studies, where flocculation caused an increase in the void ratio. This may be however caused by specific properties of larger, colloidally inactive particles of kaolin clay.

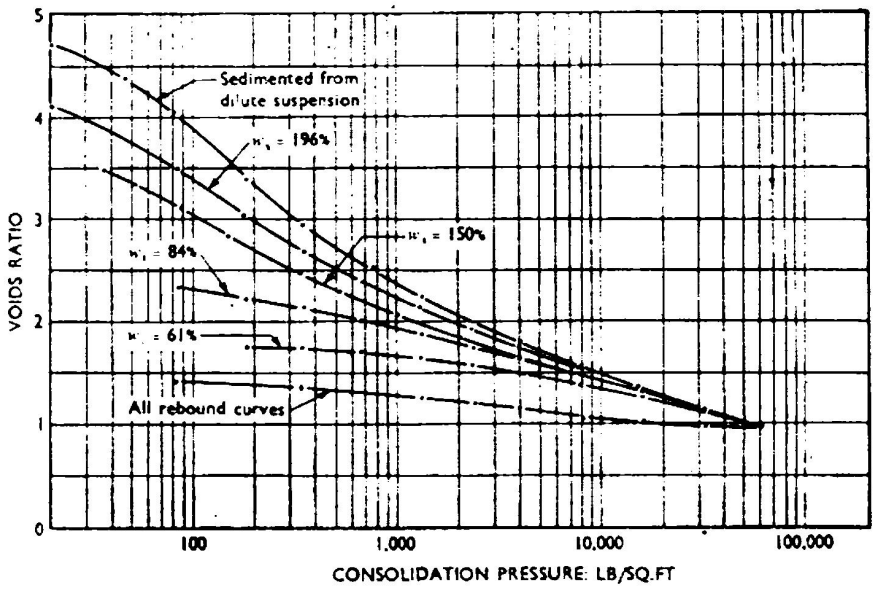

Figure 6.3: *One–dimensional compression curves for calcium illite prepared by sedimentation and reconstituted with different initial water content (Olson, 1962)*

Similar results, inconsistent with other sedimentation studies and the behaviour of natural clay, were described by Ting et al. (1994). They performed four sets of tests on Speswhite kaolin, reconstituted and sedimented in distilled and sea water. Sedimented specimens were prepared in a specially constructed 2m high sedimentation column, which allowed measurement of pore pressures and total stress at the bottom and sides of the specimen. Results are shown in Fig. 6.4. Specimens sedimented in sea water (KSS) had smaller water content than all other sets of specimens.

Two other sedimentation studies have been performed by Been and Sills (1981) and Edge and Sills (1989). Both were designed to study transition from suspension to soil, rather than the behaviour of the sedimented material. Both use a non–destructive X-ray technique to determine the density of the sedimented material. Been and Sills (1981) used estuarine mud from Somerset. Slurry flocculated in tap water and dispersed using sodium hexametaphosphate has been studied. The granulometric curves of two specimens from the top and bottom of the column are, as expected, more different for dispersed material (large fraction at the bottom of the specimen) than for flocculated material. Edge and Sills (1989) studied the possibility of creating a layered sediment in the laboratory (a sandy clayey silt from the Irish sea). A small amount of dilute slurry has been placed into the sedimentation column every day over a 42 days period, as eight hours of input followed by an overnight

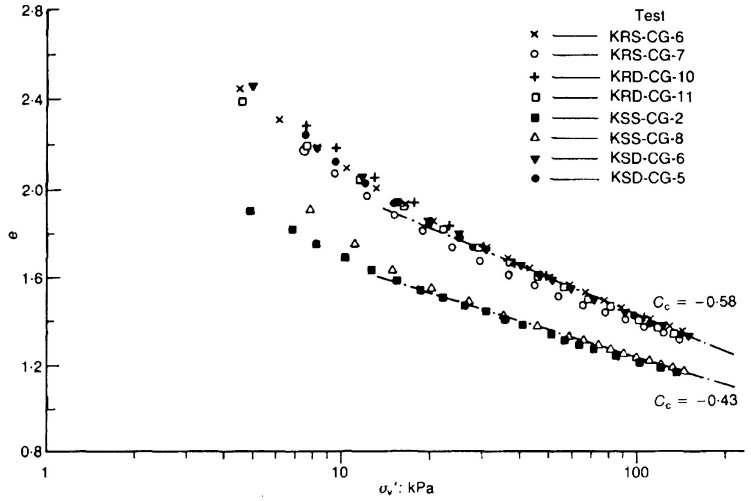

Figure 6.4: *e-log$\sigma_v^{'}$ from consolidation tests on Speswhite kaolin (Ting et al., 1994). KRS– remoulded, sea water; KRD remoulded, distilled water; KSS sedimented, sea water; KSD sedimented, distilled water*

period without addition of material. The problem to be solved was that in the natural sediment a sharp transition occurs between a clayey layer followed by a sandy layer. It would be expected that the clayey layer is so soft that grains of sand would penetrate into it and thus form a continuous transition. Accurate X-ray density measurement have shown that the creep and ageing processes caused the overnight clay layer to be stiff enough to ensure that sand particles do not penetrate through it. A sharp transition very similar to natural deposits of layered sediments has been observed.

In all the sedimentation studies described the amount of 'structure' is evaluated on the basis of void ratio – effective stress relationship. Direct comparison of structure of dispersed and flocculated (reconstituted, not sedimented) specimens of kaolinite, illite and montmorillonite was performed by Sides and Barden (1971) using a scanning electron microscope. Dispersed samples were produced by mixing the powdered clay to a slurry at twice its liquid limit, with 2% by weight solution of sodium oxalate as dispersing agent. A 2% by weight solution of calcium hydroxide was used to create a flocculated structure. A vertical section of dispersed and flocculated illite is shown in Fig. 6.5. Clearly, the structure of the flocculated specimen is far more random, with some open areas of rather loosely packed particles. Dispersed samples show a well oriented set of edges with complete preferred orientation of particles (this type of structure has been described by Smart, 1969). The authors noted that dispersing and flocculating agents have been much more effective in influencing the structure in the case of smaller collodialy active illite particles than the

larger kaolinite particles, which were presumably colloidaly inactive and hence relatively inert to the chemical additives. Moisture content after consolidation at about 30 kPa was for kaolinite 60% and 110%, illite 33% and 137% and montmorillonite 131% and 174% for dispersed and flocculated specimens respectively. The qualitative influence of flocculating agent is the same for all clay minerals, but the influence on illite is most pronounced.

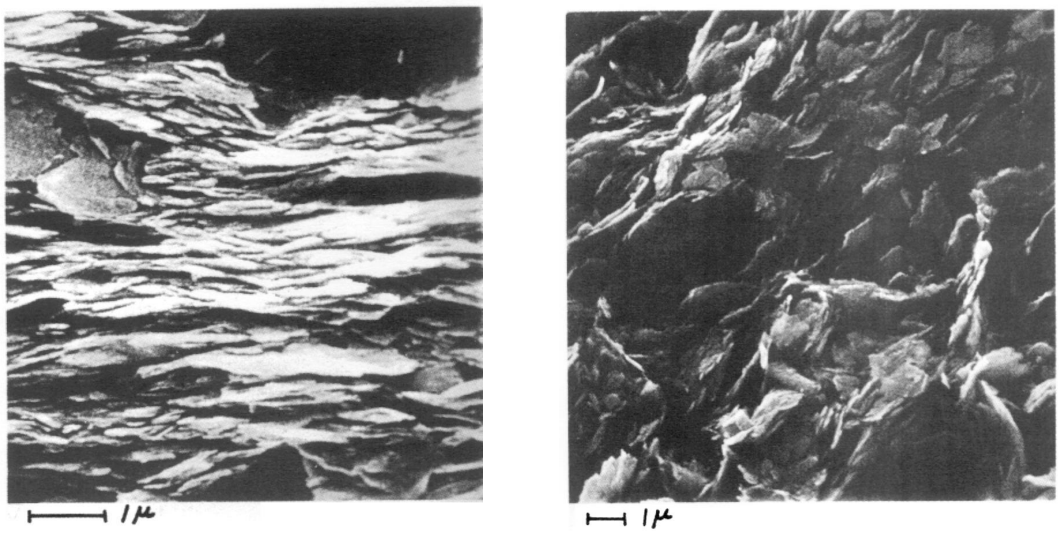

Figure 6.5: *Vertical section of dispersed illite (left) and flocculated illite (right). Sides and Barden, 1970*

These results are in agreement with findings of Bjerrum and Rosenqvist (1956), where void ratio of clay reconstituted in salty water (flocculating agent) was much higher than in fresh water.

Because, as shown by Burland (1990), the position of the ICL is directly related to the liquid limit, papers which deal with the influence of pore water chemistry on Atterberg limits are also of interest. Navaneethan and Sivakumar (2002) studied the influence of different preparation techniques on the Atterberg limits of a clay from Belfast, Ireland. The predominant clay mineral in the clay was illite. Specimens prepared in tap water (250 mg/l Ca^{2+}) had approximately the same liquid limit as in de-ionized water (about 2-3% lower for tap water). Anson and Hawkins (1998) studied residual shear strength and Atterberg limits of kaolinite and montmorillonite prepared in water with different concentration of (Ca^{2+}). The liquid limit of sodium montmorillonite decreased dramatically from 740% (0 g/l Ca^{2+}) to 245% (400 g/l Ca^{2+}). Kaolinite was shown to be much less sensitive to the concentration of Ca^{2+} in pore water. These results are not in agreement with findings of Sides and Barden (1971). As noted by Anson and Hawkins (1998), montmorillonite at low

Ca^{2+} content formed a very hydrated dispersed sol, which was progressively denser with higher amount of Ca^{2+} as the soil flocculated. In this case the final water content was influenced rather more by the degree of hydration of the collodialy active surface of the sodium montmorillonite, than by changes in the microstructure due to flocculation. The influence of the addition of different clay minerals into a typical specimen of London Clay (with 46% illite, 36% montmorillonite and 17% kaolinite from clay minerals, which form 53% of the whole soil – see section 7.1) has been performed by Burnett and Fookes (1974). They have observed that the addition of 50% kaolinite decreased the liquid limit by 25% and the addition of 50% montmorillonite increased the liquid limit by 100%.

In all the cases described the researchers tried to prepare a 'sedimentation structure' and to study how this structure is influenced by the chemistry of pore water, clay mineralogy and so on. Nevertheless, there have also been several attempts to create artificial 'postsedimentation' structure by modelling the bonding between clay particles during diagenesis. One such attempt is described in Uddin and Buensuceso (2002). They mixed soft Bangkok clay with a high organic content with different amounts of calcium oxide (CaO) powder and studied the changes in mechanical properties with different amounts of Ca0 and different curing times. They observed that lime treated clay "behaved as an overconsolidated clay", even when it was normally consolidated. This behaviour may be explained using the sensitivity framework as an enlargement of the size of the state boundary surface with subsequent destructuration (degradation of bonds) during shear. A similar study has been performed by Kainourgiaki (2002). She used Speswhite kaolin with different amounts of polyacrylamide flocculant. Some samples were then heated to create metastable polymer bridges between particles. She observed that up to some critical concentration of flocculant the void ratio and undrained shear strength increased, whereas further increases in the concentration did not have a significant effect on the shear strength and void ratio. Sensitivity increased with increased heating temperature.

6.3 Discussion and some conclusions

It is possible to draw some conclusions about the influence of different factors on the structure of sedimented clay.

- Clay mineralogy – Mineralogy influences soil structure very significantly. Clearly, Speswhite kaolin is much less sensitive to the sedimentation environment and in some cases (Ting et al., 1994) results are even qualitatively different compared to other clay minerals. The specific properties of sodium montmorillonite (susceptibility to

hydration) also had a significant influence on its behaviour (Anson and Hawkins, 1998), which caused results inconsistent with studies on natural clays (Bjerrum and Rosenqvist, 1956; Locat and Lefebvre, 1985). On the other hand sedimentation of pure illite (Olson, 1962) led to behaviour consistent with natural clays (in which illite is often a major mineral). It may be concluded at this point that natural clay should be used in order to study the development of natural structure. Speswhite kaolin is not suitable for this purpose, although it is convenient from the experimental point of view.

- The chemical composition of the pore fluid – also has a significant effect on soil structure. It influences the attractive and repulsive forces on the surface layer of clay minerals. According to the relative magnitude of these forces, clay particles are either flocculated or dispersed. Flocculated particles tend to create 'macro–particles' with 'macro–voids' in between and generally a more open structure. Although flocculation is influenced also by other factors (such as initial density of slurry), there seems to be threshold concentration of cations in pore water, below which particles tend to be dispersed and above flocculated (Locat and Lefebvre, 1985). The influence of pore water chemistry on the resultant structure is significant not only in the case of sedimented specimens (Bjerrum and Rosenqvist, 1956; Locat and Lefebvre, 1985), but also reconstituted (Bjerrum and Rosenqvist, 1956; Olson, 1962). The mechanical behaviour of the clay and the stability of the structure is also influenced significantly by the difference between the actual pore water chemistry and the chemistry when the soil was created (Bjerrum and Rosenqvist, 1956).

- Sedimentation – In all studies on natural clays and illite, sedimentation caused the structure to be more open than the structure of the equivalent clay reconstituted in water of the same chemistry. However, results relating to the stability of structure and sensitivity are contradictory and are probably specific for a clay of given a mineralogy. Olson (1962) reported sedimented structure to be unstable (normal compression lines of sedimented and reconstituted specimens merge at higher stresses). Locat and Lefebvre (1985) observed that sedimentation structure is relatively stable, being slightly unstable for specimen sedimented in salt water. Unlike Bjerrum and Rosenqvist (1956), they reported that normal compression lines of specimens sedimented in salt and fresh water merge at higher stresses and that the sensitivity of clay sedimented in fresh water is higher than the sensitivity of clay sedimented in salt water. No conclusions may be drawn about the stability of structure of sedimented specimens prepared by Bjerrum and Rosenqvist (1956).

Not enough experimental evidence has been studied to evaluate the influence of other factors, such as temperature, rate of sedimentation and initial density of slurry. However, these factors may also influence the resultant structure very significantly (Sills, 2002).

Chapter 7

Experimental investigation

In the previous chapter it was concluded that natural soil (e.g. soil with mixture of different minerals of specific granulometry) should be used to study the development of artificial structure. London Clay was chosen for laboratory experiments, as it is a typical stiff clay with a mineralogy similar to many other clays. As also pointed out in Chapter 6, the sedimentation environment and mineralogy of the clay have a significant influence on the 'sedimentation' structure developed. Therefore, some description of the properties of London Clay which are important for this research (granulometry, mineralogical composition, geological history, stability of structure) is given in this chapter. Next, experimental devices used in the laboratory investigations are described, with the special attention to the equipment devised specifically for the present research. Experimental procedures followed and results obtained are presented in detail further in the chapter.

7.1 Soil tested

London Clay may be described as a very stiff, fissured, silty clay, with occasional lenses and dustings of black silts (Chandler et al., 1998). The top 7 to 10 metres of London Clay are oxidised, showing a typical brown colour, whilst at greater depth the clay has its characteristic dark blue–grey colour (Skempton and LaRochelle, 1965). London Clay is laminated, with silty layers, sometimes obvious to the eye, followed by thicker layers with a higher percentage clay fraction (Ward et al., 1959). Geologically it represents an Eocene transgressive marine phase, which took place over much of Northern Europe. Sedimentation ceased when the London Clay Sea slowly became silted up and shallower. Clay deposits were eventually overlain by partially freshwater sand sediments and then

deposits of glauconitic sands of subsequent marine transgression (Burnett and Fookes, 1974). In mid–Tertiary the area was lifted up and much of the overlying sediments were removed by erosion in the late Tertiary and Pleistocene. The thickness of the overlying sediments removed was between 165 m in Essex to 330 m in Wraysbury district (Skempton et al., 1969) and and this resulted in a pre–consolidation pressure of about 1500 kPa and even higher (Skempton and LaRochelle, 1965). The salt pore–water has been leached from the London Clay over the time since the uplift.

London clay exhibits a remarkably uniform lithology in the London area (Skempton et al., 1969). Atterberg limits presented by various authors (Chandler et al., 1998; Ward et al., 1965; Ward et al., 1959; Skempton et al., 1969 and Bromhead, 1978) lie within the range 60 – 80% for the liquid limit and 20 – 30% for the plastic limit, therefore the plasticity index is about 40%. The clay fraction ($< 2\mu$m) is 50 to 70% and the activity is about 0.75. Due to the high degree of overconsolidation, the natural water content is generally slightly below the plastic limit.

The mineralogy has been studied extensively by Burnett and Fookes (1974). A typical mineral size distribution diagram for a sandy London Clay is given in Fig. 7.1. The most common clay mineral is illite (46%), then montmorillonite (36%) and kaolinite (17%). The percentages are as a proportion of the clay minerals, which form 53% of the whole soil. Quartz dominates the coarser fractions (40% of soil). Burnett and Fookes (1974) compared the properties and mineralogical composition of the fresh and weathered London Clay and found that they were remarkably similar.

The sensitivity of London clay has been deduced by Cotecchia (1996) by reviewing data from Ashford Common (Webb, 1964). She reported $S_t = 2$ but pointed out that the actual yield stress was not achieved and that the actual value of S_t is probably higher. Available laboratory data do not allow any statement about the stability of the structure, since compression tests have not been performed significantly beyond the yield stress and the study of de–structuration during shear is problematic due to localisation of deformation. Nevertheless it is possible to expect that the structure is stable, because experimental data on other overconsolidated stiff clays with similar mineralogical properties and stress history (e.g. Todi Clay) suggest that it is reasonable to assume a constant sensitivity ratio S_t.

The clay sample used for the research comes from the excavation at the Knightsbridge Crown Court site. The clay, which comes from a depth of approximately 12 m below the surface, is an example of the unweathered blue London Clay.

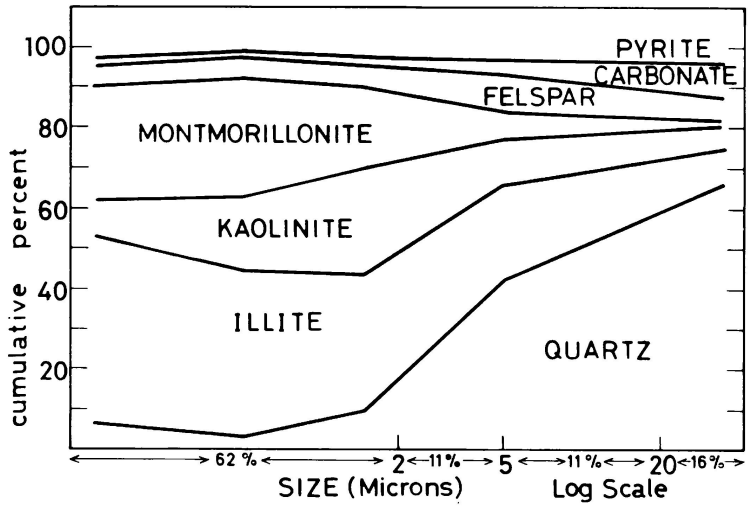

Figure 7.1: *Mineral distribution by size fractions within a typical London Clay sample (Burnett and Fookes, 1974)*

7.2 Sedimentation device

Special equipment has been developed in order to prepare sedimented specimens of the clay. This equipment is shown in Fig. 7.2. It consists of a 2 metres high and 10 cm diameter perspex cylinder. The tube may be split into two parts, which allows better access to the soil during consolidation. A buoyant perspex piston is used to load the slurry. The sedimentation tube is provided with bottom and top drainage to enable quicker consolidation. The bottom part may be opened to remove the consolidated soil. The sedimentation device and other laboratory equipment are placed in a room with a constant controlled temperature in order to exclude the effects of temperature fluctuation on experimental results.

7.3 Triaxial apparatus

7.3.1 Instrumentation and control system

Two standard hydraulic stress path cells (Bishop and Wesley, 1975) designed to test 38 mm diameter specimens were used for the research. The apparatuses have been described in detail elsewhere, for example in Jovičić (1997) and Stallebrass (1990). The setup of the apparatus is shown in Fig. 7.3 (from Jovičić, 1997), except that in these tests additional

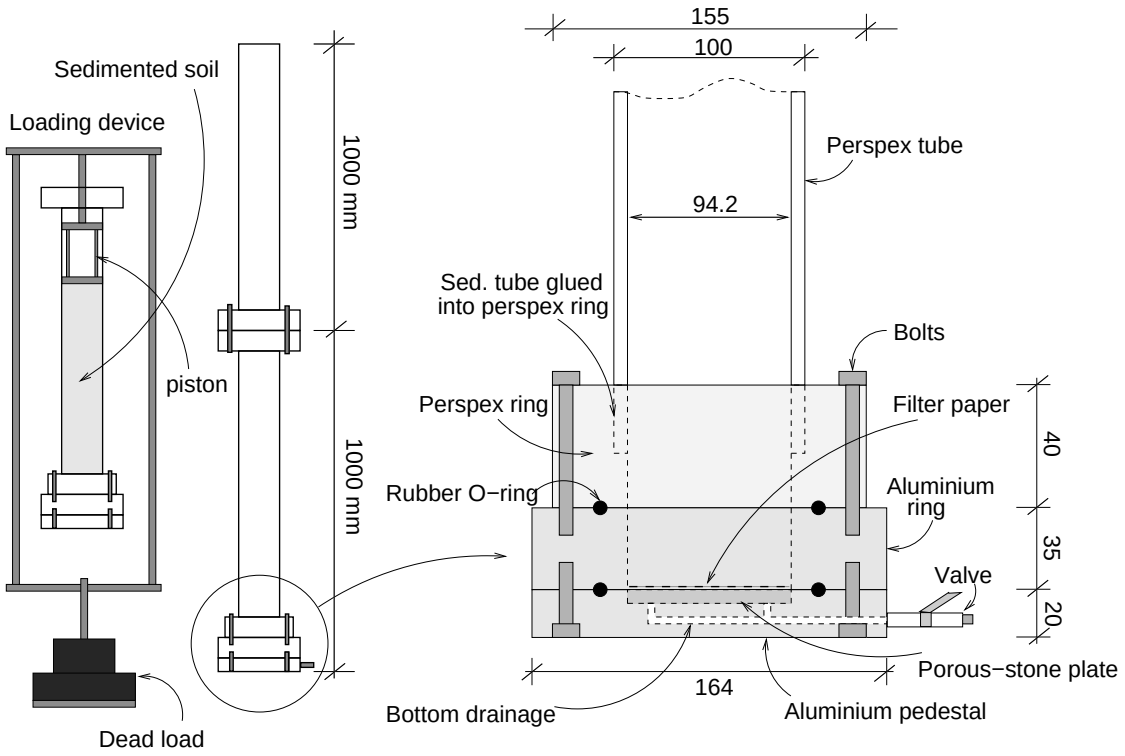

Figure 7.2: *Sketch of the sedimentation column*

local radial strain LVDT was used. Conventional instrumentation for a Bishop and Wesley hydraulic stress path cell was used. Both the stress path cells were fitted with the internal Wykeham Farrance load cells of capacity 5 kN made to the Surrey University design. The signal from the load cell was amplified using a RDP S7DC amplifier. Cell and pore pressures were measured by Druck pressure transducers with a range 0–980 kPa.

The axial displacement was measured externally and internally. The external measurement was performed using a linear variable differential transducer (LVDT) which was attached to the top of the cell and measured the movement of the pedestal. Volumetric strains were measured using a standard 50cc volume gauge of the Imperial College type. The gauge was fitted with an LVDT of the same type as that used for the external measurement of the axial displacement. Each cell was equipped with three small water–submersible LVDTs RDP D5/200 (Cuccovillo and Coop, 1997), which were used for the local measurement of axial strains (2 LVDTs) and radial strains (1 LVDT). For the AC to DC signal conditioning RDP S7DC amplifiers were used. A pair of City University piezoelectric bender elements was incorporated into each of the cells using a system developed by Jovičić (1997) in order

to reduce the electronic noise and improve the clarity of the signal.

The cells were controlled by a Spectra Micro–ms analogue to digital converter connected to a standard IBM compatible personal computer. These communicated using an interface incorporated into a Quick Basic program for triaxial testing developed by Coop (2002). The Spectra Micro–ms analogue to digital converter proved to have higher resolution than a standard 16 bit CIL Electronics data logging card.

7.3.2 Accuracy of measurements

The accuracy is given as a value of the measured physical quantity and corresponds to a 38 mm diameter and 76 mm high specimen. The characteristics of the transducers used are given in Table 7.1. Since the same type of transducers and control system was used for both triaxial apparatuses, the accuracy of measurement from both is assumed to be the same. An error due to hysteresis and non–linearity has been evaluated on the basis of the standard deviation of measured data from the best–fit least square method line during calibration. The pressure transducers were calibrated over the expected pressure range during tests, strain transducers were calibrated over their linear range. The drift of the stress transducers has been evaluated on the basis of the difference between the zero readings before and after tests. Although the duration of the tests was approximately 2 months the drift of the stress transducers was relatively small. A test to establish the drift of strain transducer was not performed over a time period comparable with the duration of the experiments and data (Tab. 7.1) were taken from Stallebrass (1990). The calibration constants have been checked and adjusted every few months.

The resolution of the pressure transducers has been taken from Jovičić (1997), since this is higher than the prescribed accuracy of the output from the computer control program. The resolution is significantly higher than other sources of errors. Although the same type of transducers has been used for measurement of pore and cell pressures the accuracy differs because they were calibrated over different pressure ranges.

The relatively high inaccuracies caused by the hysteresis and non–linearity shown by the local LVDT transducers do not have a significant influence on the overall accuracy of the measurement of strains during the shearing stages, since the figures given reflect the accuracy over the whole linear range of the transducer. Also the effect of drift is not significant, because a relative difference between adjacent readings is important. In this case resolution and noise govern accuracy. The local radial strain transducer was set to its electrical zero before the test. The axial local strain transducers had to be mounted outside

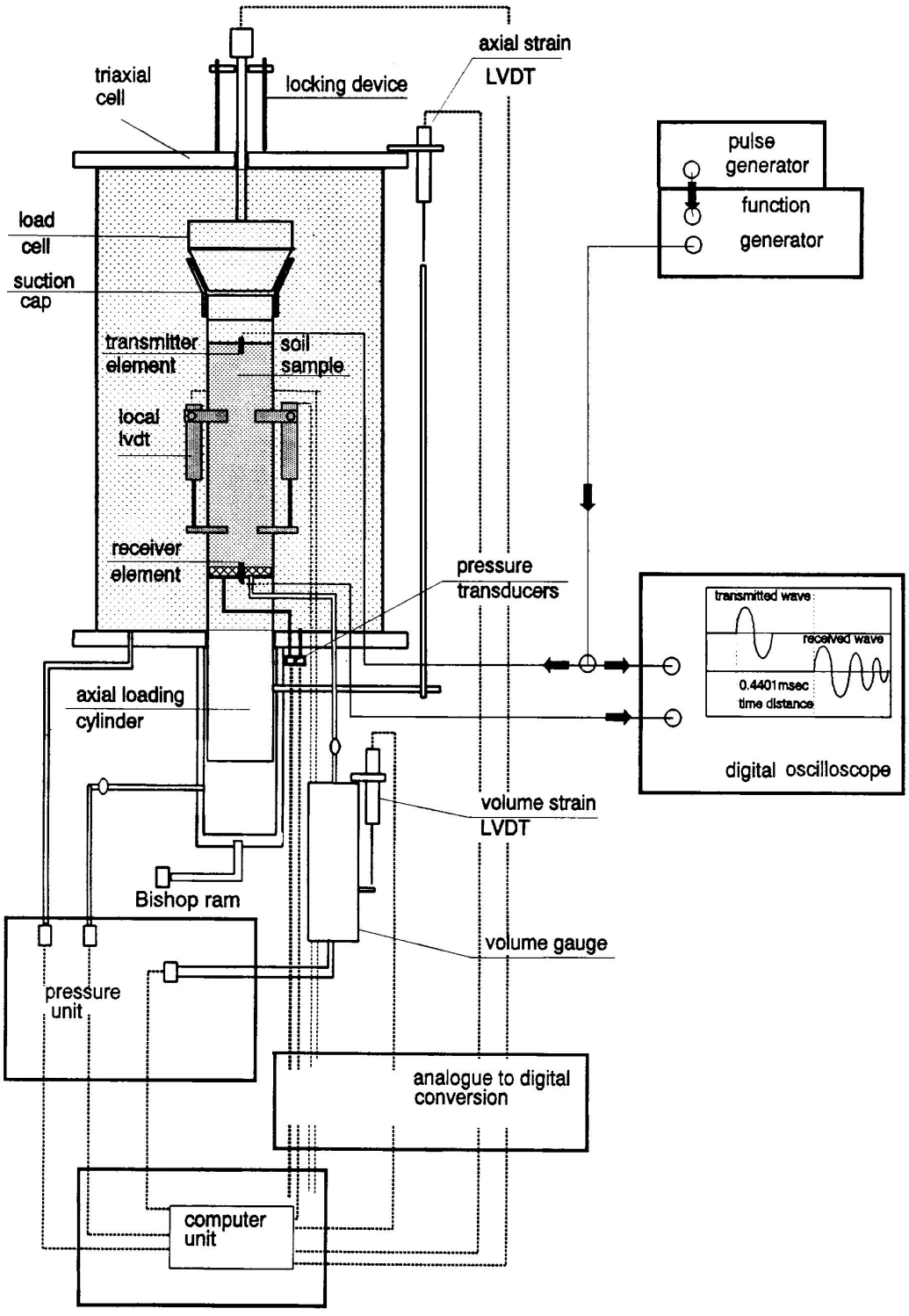

Figure 7.3: *A sketch of the triaxial apparatus used for the research (from Jovičić, 1997)*

their linear range in order to ensure that they will get in this range at the beginning of the shearing stage (due to the large axial strains during K_0 compression). No adjusting of the axial LVDT with respect to its electrical zero has been done using the zero potentiometer on the amplifier before shearing.

transducer	resolution	hyst. and non–lin.	noise	drift
load cell	0.1 kPa	±1 kPa	±1 kPa	1.5 kPa
pore pressure	0.03 kPa[1]	±0.2 kPa	±0.1 kPa	±1 kPa
cell pressure	0.03 kPa[1]	±0.3 kPa	±0.1 kPa	±1 kPa
volume strain	0.0002%	±0.004%	±0.001%	±0.02%[2]
ext. axial str.	0.001%	±0.0015%	∼ resolution	±0.03%[2]
int. axial str.	0.0004%	±0.02%	∼ resolution	±0.02%[1]
int. radial str.	0.0001%	±0.05%	∼ resolution	±0.02%[1]

Table 7.1: *Accuracy of stress and strain transducers (∗[1] from Jovičić, 1997; ∗[2] from Stallebrass, 1990)*

7.4 Experimental procedure

The results from two sets of experiments are presented in this report: Tests on reconstituted London Clay samples and tests on London Clay sedimented in salt water, representing similar conditions to those when London Clay is sedimented in nature. Most experimental procedures were similar to those described by Jovičić (1997).

7.4.1 Preparation of reconstituted samples

The reconstituted samples of London Clay were prepared from clay at its natural water content without previous oven–drying. The material was first left submerged in distilled water and then thoroughly mixed in a mechanical mixer (usually for 36 hours) until a homogeneous slurry was obtained. The initial water content of the slurry was 125%, therefore approximately 1.5 times higher than the liquid limit of the clay, as suggested by Burland (1990) for preparation of reconstituted samples. The slurry was liquid enough to ensure that no air–bubbles were introduced into it when it was poured into a consolidometer.

The slurry was poured into a perspex consolidometer of 38 mm diameter with a bottom piston, porous stone and filter paper. In order to ensure uniform one–dimensional deformations in the consolidometer the internal surface of the consolidometer was covered with

silicon grease to reduce the side friction. Samples were loaded in discrete increments up to the exact total axial stress 70 kPa. The consolidometer tube was floating.

The axial settlement was measured and the samples were tested after vertical settlement ceased. Because of the length of the tests samples have been used within two month of preparation.

The samples reconstituted in salt water were prepared in the same way as samples reconstituted in distilled water, with the pore water chemistry same as chemistry of water used for preparation of sedimented soil (Sec. 7.4.2).

7.4.2 Preparation of sedimented samples

The sedimented samples were prepared in a salt water of the same salinity as the current average salinity for the North Atlantic Ocean – 3.509%. The salt water was prepared by mixing commercially available sea salt (SAXA fine sea salt) with distilled water.

The preparation of samples consisted of reconstituting of 300 g of London Clay, at its natural water content, in 3 l of salt water in a similar way to reconstituted samples. This dilute slurry was pumped into a sedimentation column, which had previously been filled with salt water. This resulted in an initial water content for the slurry of approximately 5800%. Although the initial water content was very high the salt water acted as flocculating agent (Locat and Lefebvre, 1985) and the sedimentation was relatively quick. The slurry was left to sediment until no change in the position of the slurry–water interface could be measured (usually after three days). This cycle was repeated four times which ensured that a sufficient amount of slurry had been introduced into the sedimentation tube to produce a 76 mm high triaxial sample after K_0 consolidation (see later). Although the particles flocculated they also separated according their size during sedimentation (Been and Sills, 1981). This process led to development of a layered sediment with four layers. In each layer the silty particles were at the bottom and finer particles uppermost similar to sediment prepared by Edge and Sills (1989). This segregation reflects the layered nature of the natural London Clay (Ward et al., 1959) and therefore is desirable.

After sedimentation the slurry was loaded by a submersible piston. A floating piston had to be used in order to ensure that the actual load was very small at the beginning of loading. As the slurry consolidated, the lower drainage was opened and the sedimentation tube split. Each sample was loaded with discrete increments up to total axial stress applied to the reconstituted samples (70 kPa). The actual height of the sample after consolidation was about 140 mm.

When no vertical settlement could be measured, the bottom part of the sedimentation tube was opened and three 38 mm diameter triaxial specimens were extracted by carefully pushing thin–walled tubes into the sedimented soil. The size and weight of the specimens was measured. The material surrounding the specimens from the sedimentation tube was divided into twelve parts and weighed before and after oven–drying at 105° in order to calculate the initial water content of the specimens. Two samples were placed immediately into the triaxial apparatus, the third was waxed in the trimming tube and used after two months.

7.4.3 Setting up the samples

The procedure described from here onwards was the same for reconstituted and sedimented samples. Before setting up the samples the water in the drainage system (pore pressure leads, volume gauge and volume gauge leads) was replaced by distilled water using a Bishop ram. The base pedestal was greased with a silicon grease around its perimeter to ensure a good seal between the membrane and the metal. The porous–stone was de–aired in a vacuum chamber.

The samples were extruded onto a brass cradle with a paper on to prevent the sample sticking. The sample ends were carefully trimmed using a wire saw. The height of the samples was calculated in order to have a height:diameter ratio of about 2:1 after consolidation. In the case of K_0 consolidated samples the required initial height was about 91 mm. The actual height of the sample was measured using a vernier calliper. Three readings were taken and averaged. The diameter of the sample was assumed to be the same as the internal diameter of the consolidometer or a thin–walled tube.

At this stage the porous stone was placed onto the pedestal with a previously damped filter paper on top of it. The sample was placed with careful alignment directly onto the base pedestal. A previously dampened filter paper for radial drainage was then placed on the sample. The membrane was first placed over the sample and pedestal and the bottom O–rings placed. The divideable stretcher was then placed with top O–rings prepared and the top platen was inserted assuring both bender elements are parallel. The membrane was then released from the stretcher to grip the top platen and the top O–rings were positioned. The rubber suction cap was then placed on the top platen.

At this stage three miniature submersible LVDTs were mounted onto the sample in order to measure local axial and radial strain. They were glued directly to the membrane using a cyanoacrylate instant cement. The distance between the mounts for the axial strain

transducers was about half the height of the specimen. This ensured that the restraint caused by the rough end platens will not influence the measurements. The distance between the adjacent edges of the mounts was measured using the vernier callipers.

Once the sample had been placed in the triaxial apparatus the cell body was fixed in place and the cell was filled with water up to the middle of the specimen height. At this point the pore water leads were left open and the pore pressure, cell pressure and axial stress were re–zeroed. Then the pore pressure leads were closed and the cell was filled with water.

7.4.4 Saturation and consolidation

Using the computer control the cell pressure was increased to a value which caused the pore pressure in the sample to be 100 kPa. The effective stress was usually of the order 10-20 kPa. At this point strains were rezeroed. The pore pressure valve was then opened and the sample was left to stabilise volume changes. The saturation of samples was monitored using Skempton's (1954) 'B' value. Ideally a 'B' value of 1 should be obtained indicating full saturation of the sample. A 'B' value of 97% was considered satisfactory to proceed to a drained stage of the test.

In the case of K_0 consolidated tests the axial stress was increased with p' constant until the ratio of σ'_r/σ'_a was equal to the K_0 value obtained from previous tests on normally consolidated clays. At this point the sample was again left until volume changes had stabilised. This state was initial for the K_0 consolidation and the measured radial strain was kept constant.

The K_0 compression was performed with a constant rate of axial stress and radial stress adjusted in order to keep changes of radial strain zero. The radial strain calculated from the measured external axial strain and volumetric strain was used to control K_0 conditions, rather than measurements from the local radial strain transducers. This was because readings from the radial strain transducer tended to jump between two different values and this caused the resultant stress path to be scattered. The radial strain transducer was instead used to monitor the actual radial strain values. The measured and calculated radial strains at the end of the K_0 loading (more than 20% axial strain) were always within 0.5% of each other and usually closer.

The rate of loading was calculated using a method suggested by Atkinson (1984). The time for 100% consolidation t_1 was measured by an isotropic test on a reconstituted specimen (t_1=17h). Using this method, this value of t_1 indicated an approximate calculated rate of loading of 0.5 kPa/hour. In order to finish the tests in a reasonable time (two months) the

actual rate of loading was 1.5 kPa/hour. The volumetric strains after K_0 compression were left to stabilise and always relatively small. Typically $\Delta\epsilon_v = 0.35\%$ and total $\epsilon_v = 21.4\%$ (test PhM17).

7.4.5 Shear stages

In order to calculate stiffness at small strains it was necessary to ensure that there was a smooth increase in axial load. This was done using strain controlled loading rather than stress controlled and was achieved by means of a stepper motor attached to the Bishop ram. Drained tests were performed either with a constant cell pressure or with cell pressure controlled by computer according to prescribed stress paths. The shear stages were continued to large strains, where the specimens either achieved critical state or a constant post–rupture strength.

7.4.6 Calculation procedures

The calculation of the specific volume of the sample during the test was carried out in two ways, using the water content measured before and after the test. For the water content before the test, the rest of the specimen from the sedimentation column was divided into 12 pieces (3 horizontal layers with 4 pieces each) and weighed before and after drying at 105°. The measured water content, together with dimensions and weight of trimmed specimens, was used to calculate specific volume. For the water content measured after the test the specimens were cut horizontally into three pieces to study the homogeneity of the sample and to what extent water contents are influenced by water sucked into the sample from drainage leads after unloading. Measured water content, dimensions of the sample before test and measured volume change was used for the calculation of the specific volume. The measured initial dimensions of the specimen and volume change during the test were used for calculation of the specific volume, rather than the specific gravity of clay minerals. This was because the London Clay is a mixture of different minerals and the specific gravity of these clay minerals may vary according to their state.

In the case of specimens sedimented in salt water the amount of salt, which remained in the sample after drying was taken into account using the assumption that adding a salt to water does not change the total volume of the water and increases the water density. The specific gravity of NaCl was used (2.165), although the actual specific gravity of the sea salt may be slightly different due to presence of other minerals.

In all cases presented the strains were calculated as natural (logarithmic) strains. In

the case of shear tests local measurements of axial strains and radial strains were used for calculation of shear strains up to 3.5% shear strain, external measurement is used subsequently. Unless volumetric strains were used for the calculation of bulk modulus at small strains, external measurement was used.

The measurement of shear stiffness at small strains was smoothed using a formula (Coop, 2002)

$$G = \frac{1}{3} \frac{\sum_{1}^{n} q \sum_{1}^{n} \epsilon_s - n \sum_{1}^{n} (q\epsilon_s)}{\left(\sum_{1}^{n} \epsilon_s \right)^2 - n \sum_{1}^{n} \left(\epsilon_s^2 \right)} \tag{7.1}$$

where n is the number of readings forward from the current reading which were taken into account. n differs according to the interval between readings. The results of this smoothing process were always compared with raw (non–smoothed) measurements and n was decreased until the raw data gave the same, only more scattered, values of the shear stiffness.

No corrections were made for stiffness of membrane and side drains, volume changes of filter papers and localisation of deformation.

7.4.7 Bender elements measurement techniques

Two techniques for measurement of 'elastic' shear stiffness using bender elements were used as described below:

Using a single sine pulse

This technique is described in Jovičić (1997). The arrival time of a shear wave is assumed to be at the first deflection of detected signal. A typical output from the oscilloscope is shown in Figure 7.4.

Using a continuous sine signal with different frequencies

This method was recently developed by Greening and Nash (2003) and has been modified for the use of a continuous sine signal with constant frequency (Coop, 2002). The frequency of the input signal is tuned until the output sine wave is shifted by $n\pi$ radians relative to the input. The largest possible frequency is used for the first reading. At this point n, which is actually not known due to the near field effect at large frequencies, is a small

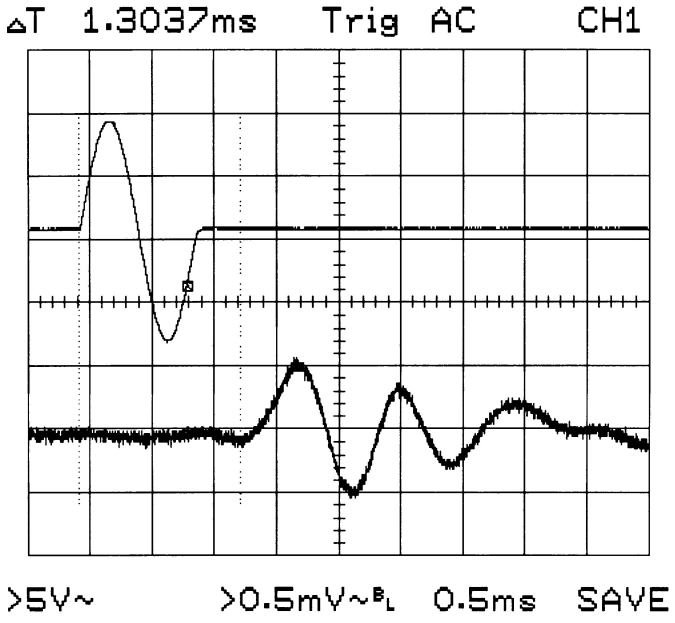

Figure 7.4: *Arrival time deduced from method with single sine pulse*

integer number. The frequency of the input wave is then increased and is registered for the phase shift $n + a$ radians. The value of a is known (1,2,3 ...). The input wave frequency is increased as long as the output signal is clear enough.

A graph of the phase shift ($a\pi$ radians) versus frequency of the input wave is plotted. The best fit line is fitted through data using the least squares method (without setting the intercept with phase shift axis to zero – n is not known). The arrival time (t_a) may be calculated from the slope (s) of the best–fit line according to

$$t_a = \frac{s}{2\pi} \tag{7.2}$$

The phase shift–frequency relationship is usually linear up to values of a between 10 and 20 according to the stiffness of the soil. For higher values of a the results are possibly influenced by 'overshooting' and are not reliable. Only smaller values of a, where dependence of frequency on phase shift is linear, are used for data processing. A typical output showing the linear range for smaller values of a is shown in Fig. 7.5.

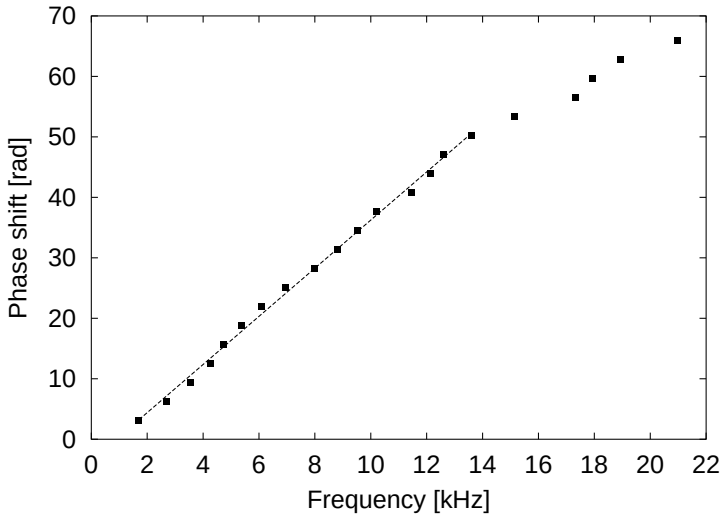

Figure 7.5: *Typical output for the method with continuous input wave*

7.5 Experimental results

A number of triaxial tests have been performed. Results from five successful tests on London Clay reconstituted in distilled water, three tests on London Clay sedimented in salt water and two tests on London Clay reconstituted in salt water are presented in this section. A summary of the triaxial tests performed is given in Table 7.2. Each test is divided into stages and the final condition for each stage is also given. For tests with a constant direction of stress path in p'/q space this direction is described by the angle in p:q space measured anti–clockwise from the p' axis.

7.5.1 Consolidation, volumetric space

The structure of the sedimented specimens is evaluated *only* on the basis of the specific volume of soil, since no study using an scanning electron microscope was performed.

The specific volume of each sedimented specimen was measured both before and after the test. Ideally both measurements should be consistent. The measurement before the test was performed using the soil remaining after trimming the specimens. The soil was divided into three horizontal layers and the specific volume was measured using four pieces from each layer. From four measurements in each layer the one which differed most from the others was not taken into account. The weighted average water content for each layer was calculated by weighting the water content of each piece by its dry weight. The standard

test number, material	stage	test type for given stage	final condition
PhM9 reconst., dist. wt.	1	isotropic compression	$\sigma'_a = 400$ kPa
	2	const. dir. shearing 108°, comp.	$\epsilon_s = 19\%$
PhM10 reconst., dist. wt.	1	K_0 loading	$\sigma'_a = 400$ kPa
	2	K_0 unloading	$\sigma'_a = 150$ kPa
	3	undrained shear, comp.	$\epsilon_s = 14\%$
PhM12 reconst., dist. wt.	1	K_0 loading	$\sigma'_a = 300$ kPa
	2	K_0 unloading	$\sigma'_a = 100$ kPa
	3	K_0 loading	$\sigma'_a = 400$ kPa
	4	p' const. shear, comp.	$\epsilon_s = 21\%$
PhM13 reconst., dist. wt.	1	isotropic loading	$p' = 250$ kPa
	2	isotropic unloading	$p' = 50$ kPa
	3	isotropic loading	$p' = 150$ kPa
	4	isotropic unloading	$p' = 50$ kPa
PhM14 reconst., dist. wt.	1	K_0 loading	$\sigma'_a = 400$ kPa
	2	K_0 unloading	$\sigma'_a = 100$ kPa
	3	K_0 loading	$\sigma'_a = 266$ kPa
	4	const. p' shear, ext.	$\epsilon_s = -14$ %
PhM17 sedim., salt. wt.	1	K_0 loading	$\sigma'_a = 400$ kPa
	2	K_0 unloading	$\sigma'_a = 100$ kPa
	3	K_0 loading	$\sigma'_a = 266$ kPa
	4	const. p' shear, ext.	$\epsilon_s = -14$ %
PhM18 sedim., salt. wt.	1	K_0 loading	$\sigma'_a = 400$ kPa
	2	const. stress dir.	$p' = 450$ kPa, $q = 0$ kPa
	3	undrained shear, comp.	$\epsilon_s = 21\%$
PhM19 sedim., salt. wt.	1	K_0 loading	$\sigma'_a = 400$ kPa
	2	K_0 unloading	$\sigma'_a = 100$ kPa
	3	const. p' shear, comp.	$\epsilon_s = 17\%$
PhM21 reconst., salt. wt.	1	K_0 loading	$\sigma'_a = 400$ kPa
	2	const. stress dir.	$p' = 450$ kPa, $q = 0$ kPa
	3	undrained shear, comp.	$\epsilon_s = 22\%$
PhM22 reconst., salt. wt.	1	K_0 loading	$\sigma'_a = 400$ kPa

Table 7.2: *Summary of performed triaxial tests*

deviation of the water contents of the pieces from each layer was also calculated.

The water content of each layer was used for the calculation of the specific volume of each layer using the dimensions and wet weight of one of the trimmed specimens (PhM18). Note that a simplification has been made here, because the trimmed specimen could not be divided into three layers to find wet weight for each layer. The amount of salt in the pore water has been taken into account. The standard deviation of the water contents from each layer has been used to calculate uncertainty in the specific volume.

The results are shown in Table 7.3. This measurement revealed that the soil in the sedimentation column is not consolidated homogeneously, the top layer which is in contact with loading piston being consolidated the most. This is probably caused by the side friction on the sedimentation column, which is not floating in the sense of floating consolidometer tubes. Because of this inhomogeneity, the specific volume was calculated from the measurement of water content at the end of the triaxial test.

layer	average specific volume	±
top	2.70	0.03
middle	2.86	0.03
bottom	2.93	0.12

Table 7.3: *Specific volumes measured before the test on sedimented specimens*

After the test the specimen was divided horizontally into three layers and the water content was measured for each layer. It should be noted that the triaxial specimen was only made up of the top and middle layers from the sedimentation column. For two specimens tested the results from the three layers were fairly consistent, the water content of the bottom layer being slightly higher. This difference may be caused by water being sucked into the sample from the drainage leads or by the horizontal inhomogeneity of the sedimented specimen (due to its layered nature). Because horizontal layering may play a significant role, all three layers were taken into account when the specific volume was calculated. The initial specific volumes back–calculated from samples PhM17 and PhM18 were 2.705 and 2.707 respectively. The results are fairly consistent with each other and also with the water content calculated from the upper layers of the sedimented sample before the test (Tab. 7.3).

The specific volume of the reconstituted specimens was back–calculated from the samples after the tests. The specimens were also divided into three layers to check the distribution of water content throughout the specimen. Water contents from the three layers were

usually similar (38.7% (bottom), 38.3% (middle) and 38.8% (top) for PhM14). All three layers were taken into account in the calculation of the specific volume, in order to be consistent with the sedimented specimens. An error at the end of tests PhM10 and PhM12 meant that the specific volume could not be measured correctly, it was therefore adjusted in order that the normal compression lines of these tests matched those of other successful tests.

Isotropic and K_0 normal compression lines for reconstituted specimens are shown in Figure 7.6. Results of these tests were used for the derivation of parameter $\lambda^* = 0.11$ and the intercept of the isotropic normal compression line $N = 1.37$ and the K_{0NC} line $N_{K_0} = 1.335$. The position of the critical state line may be calculated assuming the Modified Cam–Clay shape of the state boundary surface, which gives $\Gamma = 1.294$.

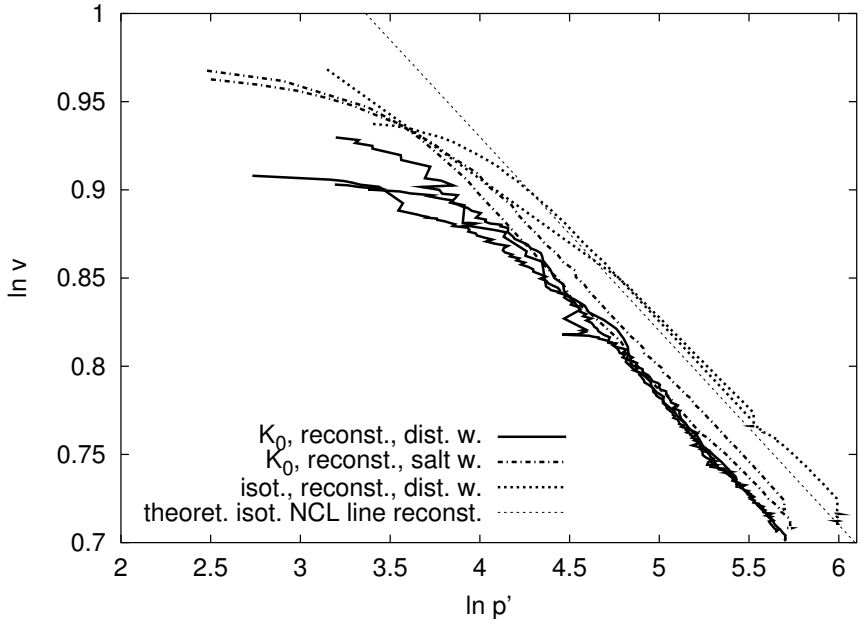

Figure 7.6: *Normal compression lines for reconstituted specimens with fitted isotropic normal compression line*

Figure 7.7 shows K_0 normal compression lines for reconstituted and sedimented specimens. It may be seen that specimens sedimented in salt water have a significantly higher specific volume at the same value of p', leading to a computed sensitivity $S_t = 1.69$. Both K_{0NC} lines for sedimented and reconstituted specimens are parallel and this suggests that the structure of the sedimented specimen is stable over the stress range applied. The intercept N_{K_0} for the sedimented specimen is 1.393. Because K_{0NC} conditions and the shape of the

state boundary surface of reconstituted and sedimented specimens are similar (discussed later) the position of the critical state line for sedimented specimen may be calculated ($\Gamma = 1.352$). Critical state lines of reconstituted and sedimented specimens are plotted by dashed lines and it is clear that the experimental points lie close to these lines, suggesting the structure is stable even when the soil reaches the critical state.

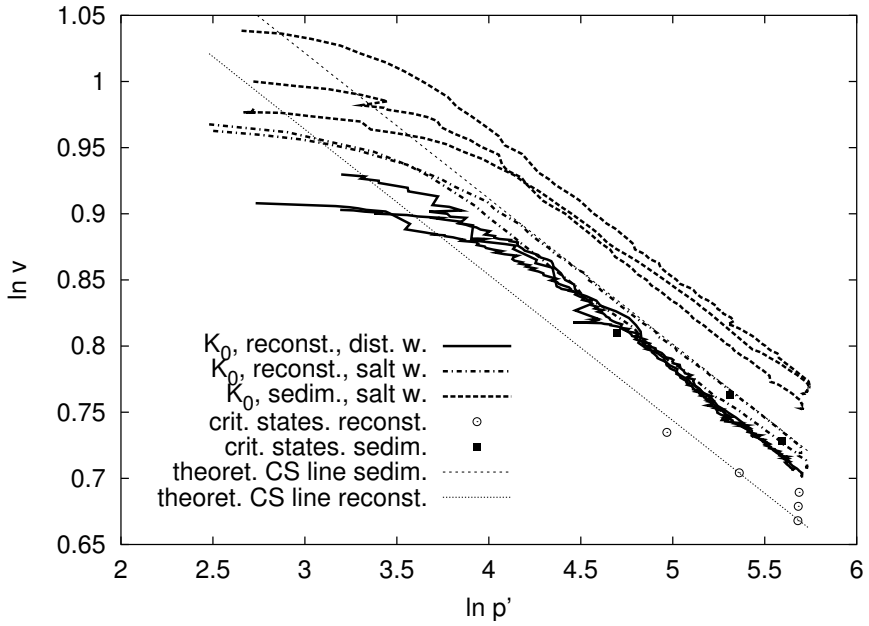

Figure 7.7: *K_0 normal compression lines for reconstituted and sedimented specimens with calculated critical state lines (dashed)*

7.5.2 K_0 conditions

The stress paths for K_0 loading and unloading tests are shown in Figure 7.8 for sedimented (left) and reconstituted (right) specimens. There is no significant difference between K_0 stress state of reconstituted and sedimented specimens. A line for $K_{0NC} = 0.62$ is also included in the figure. The variation of $K_{0NC} = \sigma'_r/\sigma'_a$ with p' is shown in Figure 7.9.

Curves showing the variation of K_0 with respect to overconsolidation ratio ($OCR = \sigma'_a/\sigma'_{aMAX}$) for first unloading are shown in Figure 7.10. There is no apparent difference between K_{0OCR} state for sedimented and reconstituted specimens. Values for K_0 calculated from the formula proposed by Mayne and Kulhawy (1982) are also included in the figure. The formula fits the experimental data reasonably well, although it slightly underestimates the K_0 state.

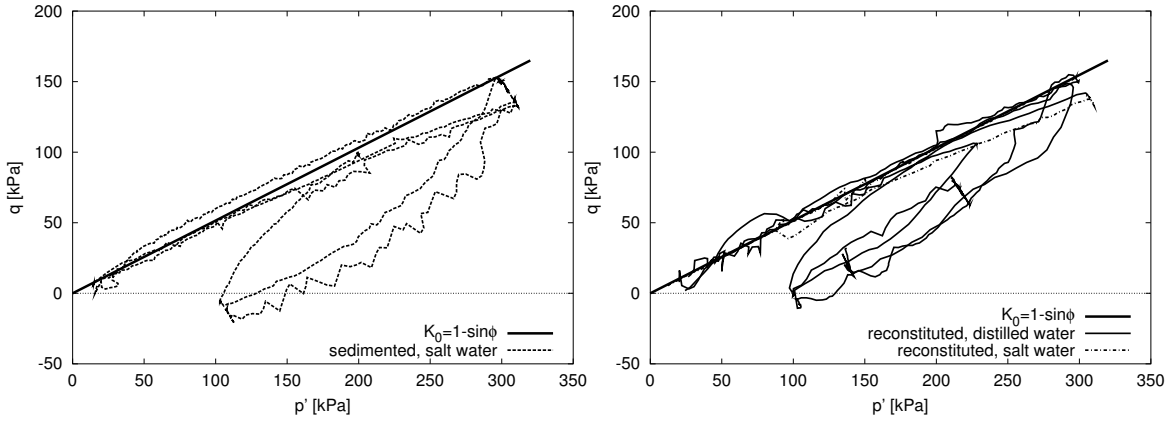

Figure 7.8: *Stress paths of K_0 tests for specimens reconstituted in salt and distilled water and sedimented specimens (with line for $K_0 = 0.62$)*

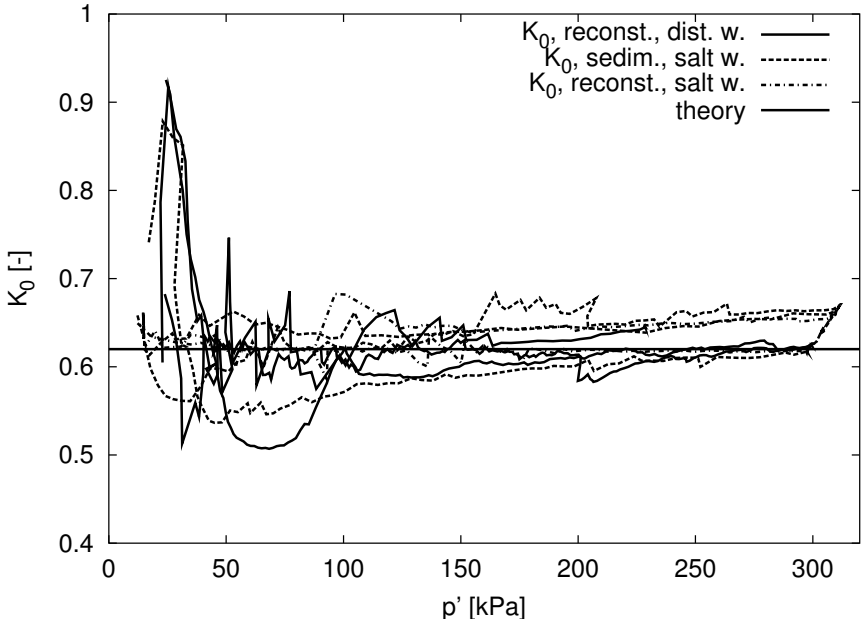

Figure 7.9: *K_{0NC} conditions for reconstituted and sedimented specimens (with line for $K_0 = 0.62$)*

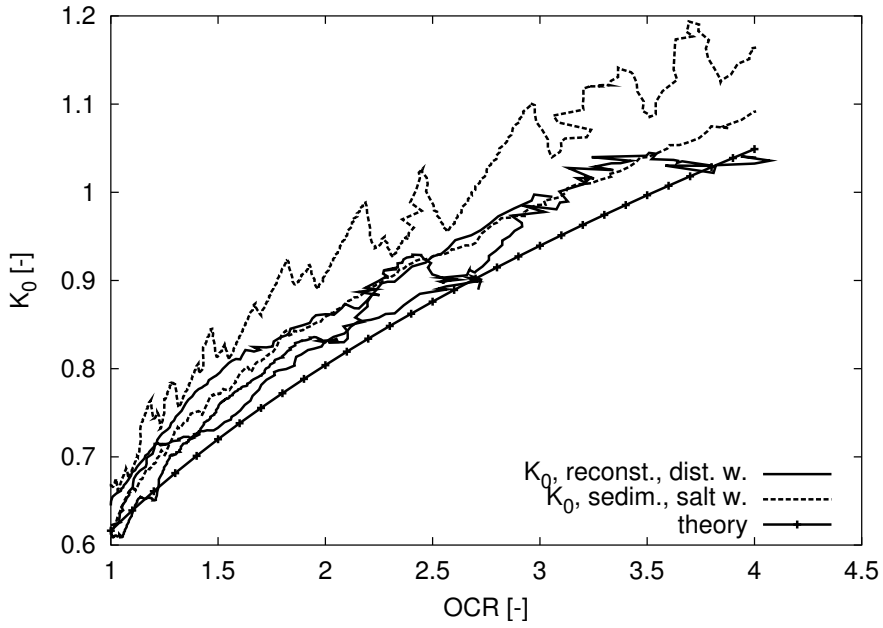

Figure 7.10: *K_0 conditions for first unloading for reconstituted and sedimented specimens with curve defined by equation of Mayne and Kulhawy (1982)*

7.5.3 Stiffness at very small strains

Stiffness at very small strain has been determined using bender elements during K_0 loading and unloading. Comparison of shear modulus G determined by the single sine pulse method for tests on sedimented and reconstituted specimens is shown in Figure 7.11. There is no apparent difference in G for sedimented and reconstituted specimen. Figure 7.12 shows very small strain shear modulus for a sedimented and reconstituted specimens determined using the continuous sine signal method. The shear stiffness measured by the continuous methods is significantly smaller than with a single sine pulse method. G measured by the continuous methods is about 55% of G measured by single pulse method. This is consistent with the findings of Greening and Nash (2003), but inconsistent with Coop (2002), who reports that results of both methods are within 10% of each other. A continuous method seems to be more reliable (Coop, 2002) because it does not suffer from the uncertainty of determination of the first arrival time and is in agreement with stiffness measured by local transducers (see Sec. 7.5.6). Therefore, parameters A, n and m (defined in Equation 3.17) were derived from results of this method A=457, n=0.71 and m=0.27. Very small strain shear modulus computed using these parameters is also shown in Figure 7.12.

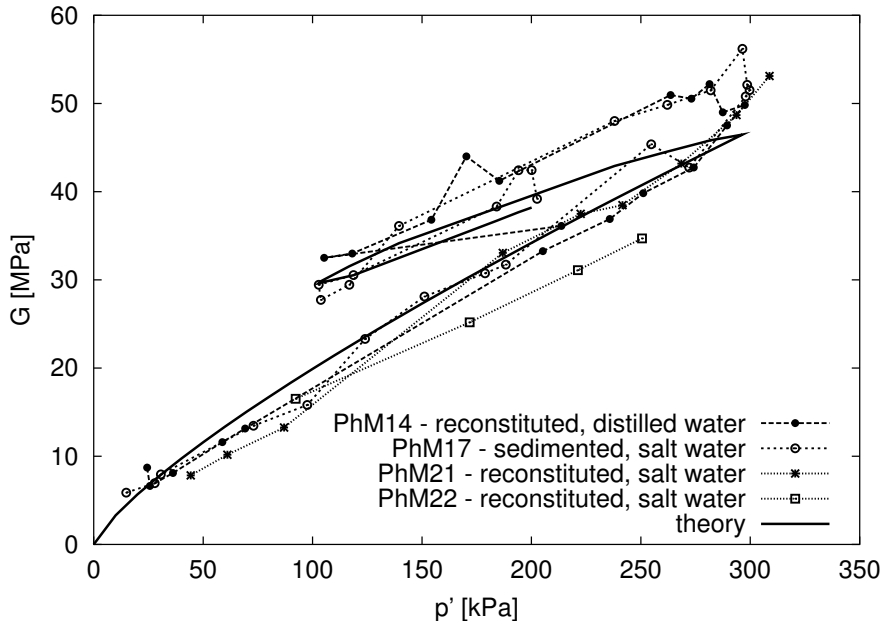

Figure 7.11: *Very small strains shear modulus determined by bender elements using a single sine pulse method for reconstituted and sedimented specimens*

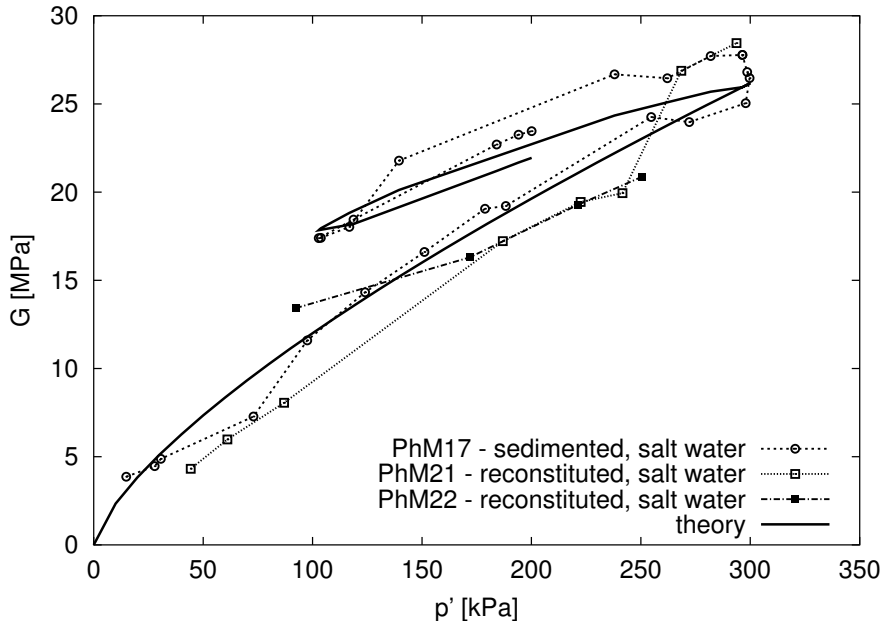

Figure 7.12: *Very small strain shear modulus determined by bender elements using a continuous sine signal method for reconstituted and sedimented specimens compared with theoretical curve (note different scale than in Fig. 7.11)*

7.5.4 Shear stages–stress paths

Stress paths followed during shearing stages of the tests performed are shown in p'/q stress space in Figure 7.13. Critical state points and a critical state envelope for a friction angle $\phi = 22.6°$ are also plotted in the figure. This critical state friction angle correspond to a critical state friction coefficient M in triaxial compression of 0.88 and to $K_{0NC} = 0.62$ using Jáky's (1948) formula (Eqn. 3.28). The critical state line fits the experimental data relatively well. Jáky's (1948) relationship seems to provide a good estimate for the K_{0NC} stress state.

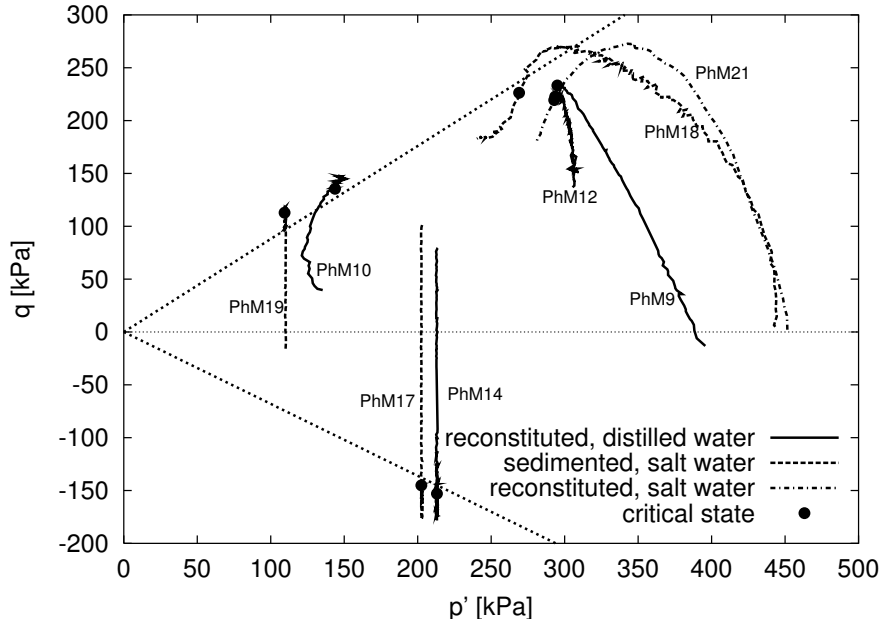

Figure 7.13: *Stress paths of performed tests with critical state friction envelope ($\phi = 22.6°$)*

Figure 7.14 shows the stress paths of the shearing stages of the tests performed normalised with respect to $S_t p_e^*$ (p_e^* defined in subsection 2.1.1, S_t being sensitivity) together with the state boundary surface defined by the AI3-SKH model. The value $S_t = 1.69$, calculated from K_{0NC} lines of reconstituted and sedimented specimens (Sec. 7.5.1), was used for normalisation.

Stress paths normalised with respect to p_e^* are shown in Figure 7.15. The difference between the size of the state boundary surfaces of the reconstituted and sedimented specimens is demonstrated.

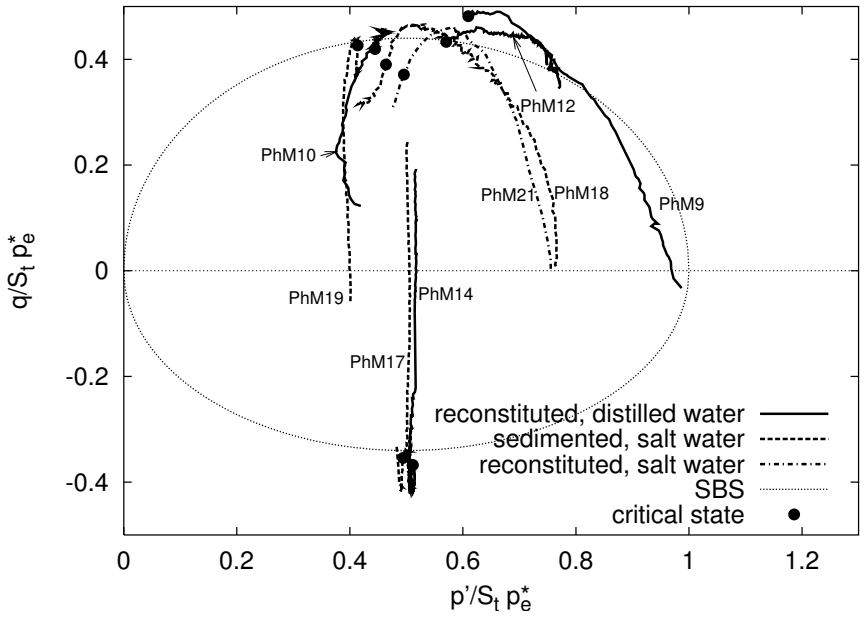

Figure 7.14: *Stress paths normalised with respect to $S_t p_e^*$ with the state boundary surface predicted by the AI3-SKH model*

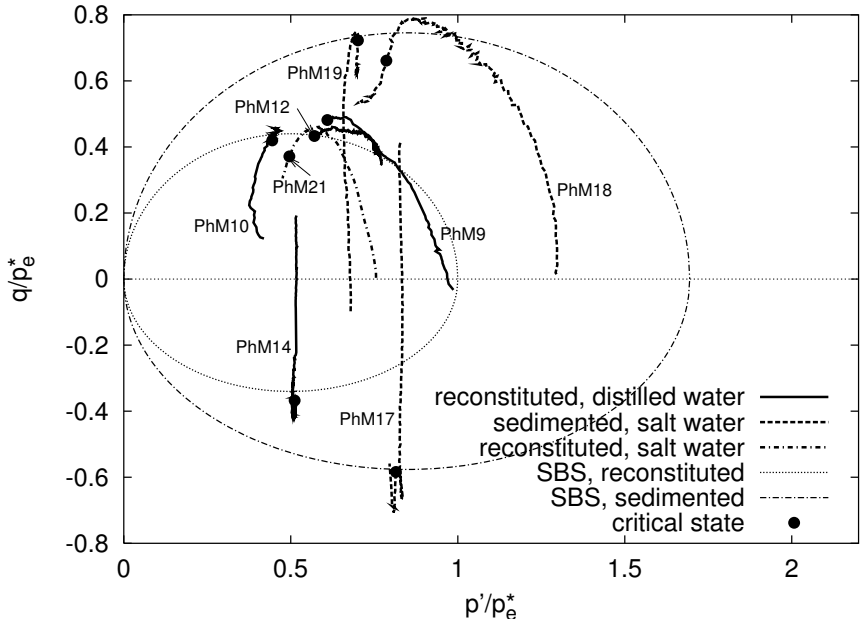

Figure 7.15: *Stress paths normalised with respect to p_e^* with the state boundary surface predicted by the AI3-SKH model*

7.5.5 Stress–strain behaviour

Graphs of stress ratio q/p' versus shear strain together with a line representing critical state stress ratio q/p' for $\phi = 22.6°$ are shown in Figure 7.16. It is interesting to point

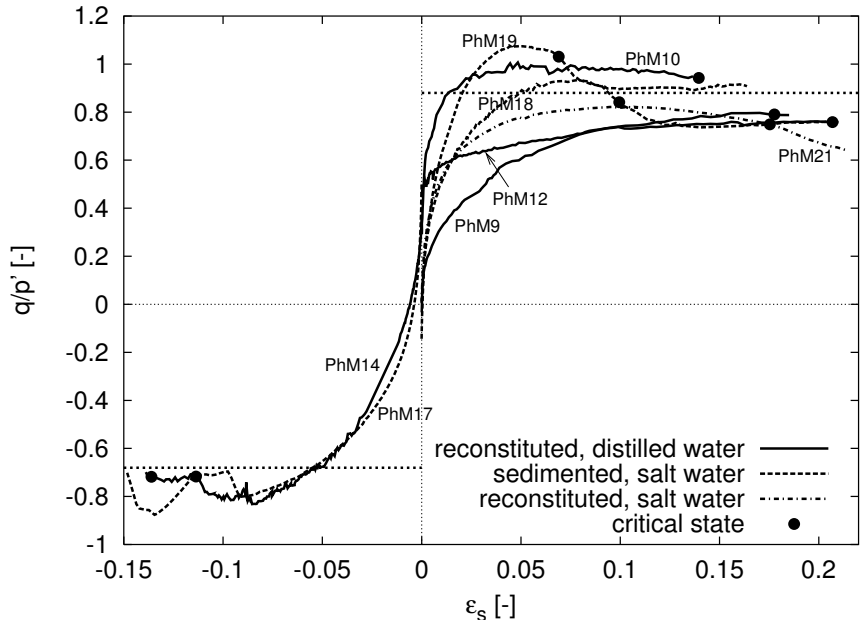

Figure 7.16: *Stress ratio q/p versus ϵ_s graphs for all performed shear tests with critical state q/p related to the $\phi = 22.6°$*

out the following observation: Tests PhM14 and PhM17 followed exactly the same stress history, PhM14 being on a reconstituted specimen, PhM17 on a sedimented. It is clear that the large strain behaviour of both specimens is very similar. Both also follow the same stress paths normalised by $S_t p_e^*$ (Fig. 7.14). The same applies for tests PhM18 and PhM21.

A localisation of deformation occurred in the tests PhM18 and PhM19, which caused rapid post–peak decrease of deviatoric stress. In these cases a critical state was *assumed* following the work of Cotecchia (1996), who performed corrections for localisation using a formula proposed by Chandler (1966). The resulting critical state was approximately half way between the peak and the post–rupture strength.

7.5.6 Small strain stiffness

Tangent shear modulus measured by local strain transducers is shown in Figure 7.17. As with large strain stiffness, corresponding experiments with the same stress history, one being on reconstituted specimen and one being on sedimented specimen (PhM14 and PhM17; PhM18 and PhM21) are compared. Shear modulus is normalised with respect to $p^n R_0^m$. In this normalised space shear modulus measured by bender elements is represented by the value of parameter A on the vertical axis. The value of A derived from the method using a continuous sine signal is also shown in Figure 7.17. There is a relatively good agreement between small–strain modulus measured by bender elements and by local strain transducers. Bender element measurements provide an upper boundary for shear moduli measured by local transducers. No obvious trend can be seen from comparison of G of corresponding tests PhM14+PhM17 and PhM18+PhM21. Smaller initial stiffness measured in the tests PhM18 and PhM19 may be possibly attributed to incorrect local LVDT measurements in the very small strain range.

7.5.7 Quasi–elastic and recent stress history boundaries

One test (PhM13) which was performed on a reconstituted specimen was designed to study the extent of the region with negligible or no plastic strains and the region in which recent stress history influences soil behaviour. Using the 3SKH/AI3-SKH model these regions are represented by the yield and history surfaces. The stress path followed is summarised in Table 7.2. The variation in bulk modulus during isotropic unloading with an initial p'=150 kPa and two different stress path rotations is shown in Figure 7.18.

Values of parameters T and S of the AI3-SKH/3-SKH model calculated from results of the test PhM13 are T=0.24 and S=0.16.

7.6 Conclusions from laboratory work

Conclusions which may be drawn from results of laboratory experiments:

- Clay sedimented in salt water has a significantly higher specific volume than the equivalent reconstituted soil, leading to a sensitivity approximately $S_t = 1.69$. This sensitivity is comparable with natural London Clay, which has sensitivity of approximately 2. It may be expected that the sensitivity of natural London Clay has been increased after sedimentation by creep and ageing processes. The structure is stable

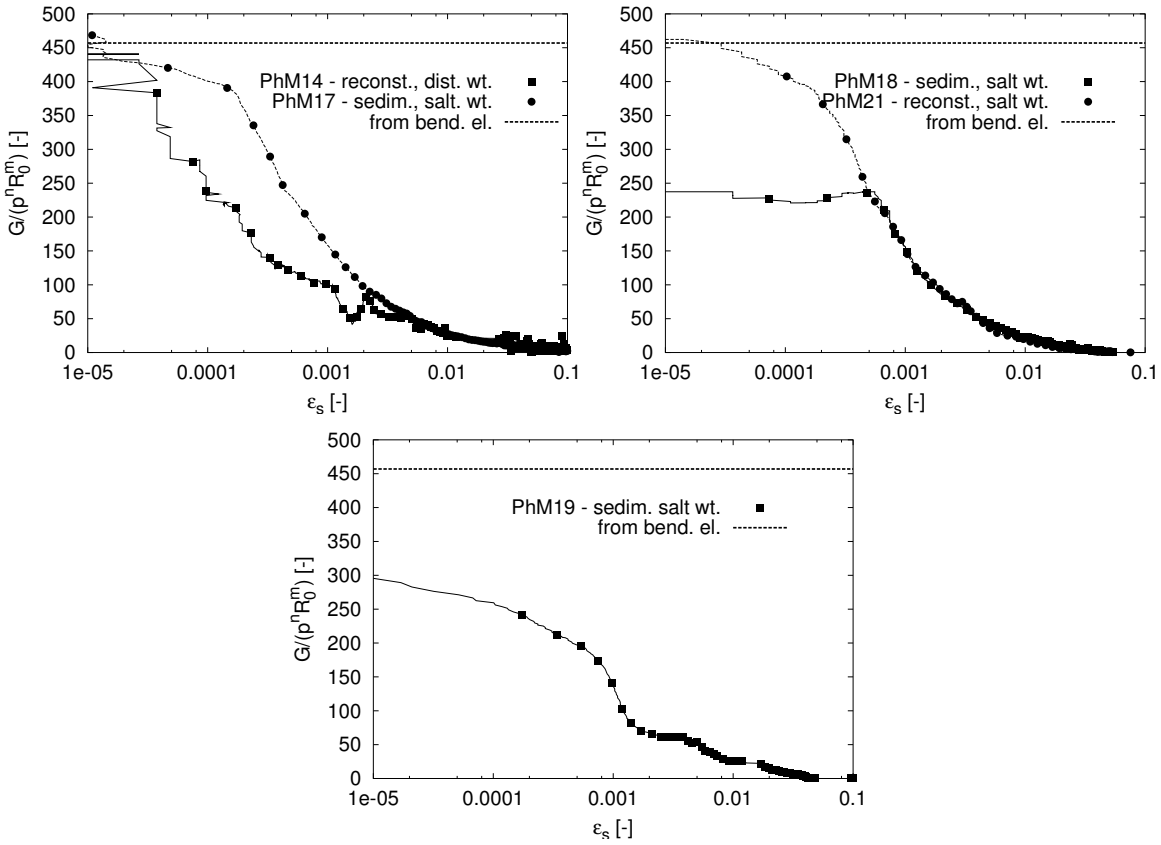

Figure 7.17: *Normalised shear stiffness at small strains measured by local strain transducers with the value of parameter A derived from measurements of bender elements*

over the applied range of stresses and remains even when the soil reaches a critical state.

- Clay specimens reconstituted in distilled and salt water have comparable specific volume. In other words, clay reconstituted in salt water has a sensitivity (related to the clay reconstituted in distilled water) approximately equal to 1. This observation is not in agreement with some previously published experimental results summarised in Section 6.2. As also discussed in Section 6.2, the influence of pore water chemistry is strongly dependent on the soil mineralogy.

- There is no apparent difference between the K_{0NC} stress state of sedimented and reconstituted specimens. This value is consistent with the critical state friction angle according to Jáky's (1944) formula. The empirical relationship reported by Mayne and Kulhawy (1982) holds for first K_0 unloading.

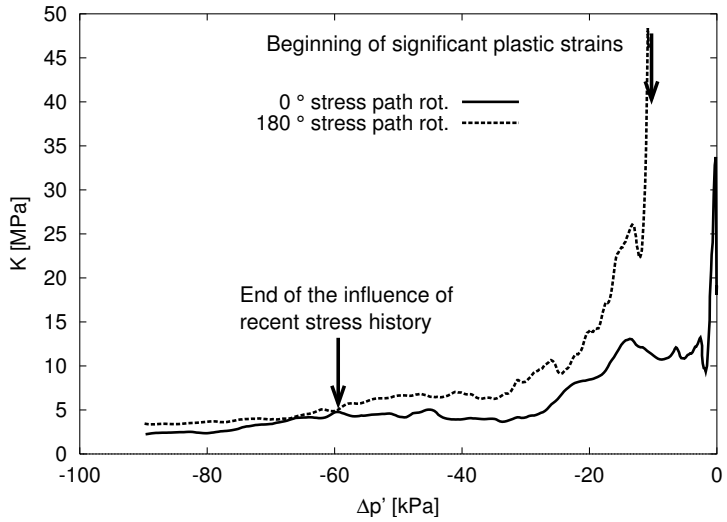

Figure 7.18: *Degradation of bulk modulus during isotropic unloading test with two different stress path rotations*

- Stiffness at very small strains measured by bender elements appears to be the same for reconstituted and sedimented specimens, compressed and swelled to the same vertical stresses at K_0 states, but not at the same specific volumes.
- The bender element measurement technique, which uses a continuous sine signal of different frequencies, leads to significantly smaller stiffness. This measurement seems to be more reliable, because it does not suffer the problem of identification of the arrival time and is consistent with measurements of local strain transducers.
- There seems to be no difference between the critical state friction angle for reconstituted and sedimented specimens.
- The shape of the state boundary surface seems to be the same for isotropically compressed reconstituted specimen and sedimented one–dimensionally compressed specimens. This shape is reasonably well described by the elliptical shape of the state boundary surface of the Modified Cam–Clay model (Modified for predicting the same friction angle in triaxial compression and extension).
- The large strain tangent stiffness seems to be the same for reconstituted and sedimented specimens with the same stress histories. No clear conclusions may be drawn for shear stiffness in the middle–strain range.
- The extent of the influence of the recent stress history has been evaluated.

Although experimental results give a comprehensive comparison of behaviour of reconstituted and sedimented soil, additional experiments could clarify some uncertain points:

- The set of laboratory experiments on K_0 compressed soil sedimented in distilled water could be included into the testing program presented. Although these experiments would be valuable, preliminary investigation has shown that they would be more time–consuming. The soil reconstituted in distilled at very high water contents is less flocculated and this leads to longer times required for sedimentation.

- The current testing program on K_0 compressed specimens could be extended by additional experiments on reconstituted isotropically compressed soil. Laboratory experiments on isotropically compressed specimens are significantly simpler to perform, natural clays are, however, K_0 compressed. The set of experiments on reconstituted isotropically compressed soil would be helpful to clarify if these tests are sufficient to provide constitutive parameters for natural soil (provided the constitutive models enhanced by the sensitivity framework are used).

- The present testing program includes 5 shear tests, where local LVDT transducers were mounted onto the specimen. Due to the uncertainty of some conclusions, mainly related to the middle–strain range, some experiments on K_0 compressed specimens could be added in order to study the difference of the rate of stiffness degradation of reconstituted and sedimented specimens.

Chapter 8

Application of the sensitivity framework and the AI3-SKH model on sedimented London Clay

In this chapter, the AI3-SKH model, together with the sensitivity framework (Cotecchia and Chandler, 2000), will be applied to reproduce the results of laboratory experiments presented in the previous chapter. From here onwards only the AI3-SKH model, which proved to be suitable for modelling reconstituted clays, will be used.

8.1 Parameters of the AI3-SKH model

The experimental results summarised in the previous Chapter allow the majority of the parameters of the AI3-SKH model to be evaluated. Only parameters κ^* and ψ were not derived. Parameter κ^* was calculated from the quasi–elastic shear modulus measured by bender elements assuming a reasonable value of Poisson ratio (0.25), which led to $\kappa^* = 0.006$.

Parameter ψ has been evaluated by means of a parametric study using the results of the test PhM19. Evaluation of this parameter is shown in Fig. 8.1. The value $\psi = 2$ has been assumed.

All parameters used in the AI3-SKH model are summarised in Table 8.1. Values of parameters for the 3–SKH model for London Clay derived by Stallebrass and Viggiani (1994) using a limited number of triaxial tests on reconstituted London Clay are given for comparison.

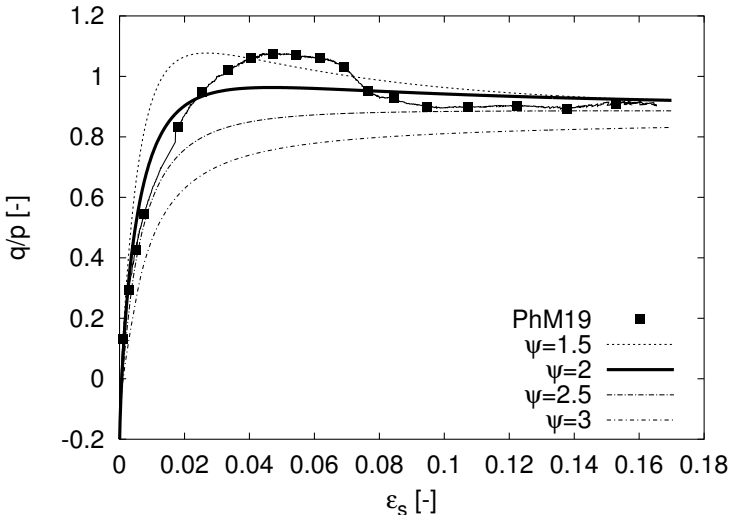

Figure 8.1: *Evaluation of the parameter ψ of the AI3-SKH model*

London Clay	A	n	m	M	κ^*	λ^*	T	S	ψ	N	S_t
reconstituted sedimented	457	0.71	0.27	0.88	0.006	0.11	0.24	0.16	2	1.37	1.69
Viggiani and Stallebrass (1994)	407	0.76	0.25	1	0.006	0.097	0.2	0.08	2.5	1.269	

Table 8.1: *3-SKH/AI3-SKH parameters derived from this study and during previous research (Stallebrass and Viggiani, 1994)*

8.2 Comparison of AI3–SKH predictions with experiment

Detailed experimental data allow the applicability of the AI3-SKH model to predict broad range of aspects of clay behaviour to be evaluated. In all the laboratory experiments examined, the whole stress histories of the specimens were simulated (including consolidation in a consolidometer). This allows the correct alignment of kinematic surfaces at all stages of simulation to be achieved. The stress history of a typical test (PhM14) is described in Table 8.2. Simulation of all other test followed the actual test procedures summarised in Table 7.2. Initial states of simulations are the same as those used in the simulations of experiments on reconstituted Boom clay (Sec. 4.1).

test number	stage	test type for given stage	final condition
PhM14	1	K_0 compression	$\sigma_{ax} = 70$ kPa
	2	undrained extension	$q = 0$ kPa
	3	isotropic swelling	$p' = 23$ kPa
	4	K_0 loading	$\sigma_{ax} = 400$ kPa
	5	K_0 unloading	$\sigma_{ax} = 100$ kPa
	6	K_0 reloading	$p' = 213$ kPa
	7	constant p' compression	$\epsilon_s = 14$ %

Table 8.2: *Simulation of the stress history of the test PhM14*

8.2.1 K_0 state

The K_0 test PhM14 has been simulated, as it is a typical test which comprises also K_0 unloading and reloading. The K_0 stress state predicted is compared with experimental data in Fig. 8.2 (left) and the K_0 volumetric state in Fig. 8.2 (right).

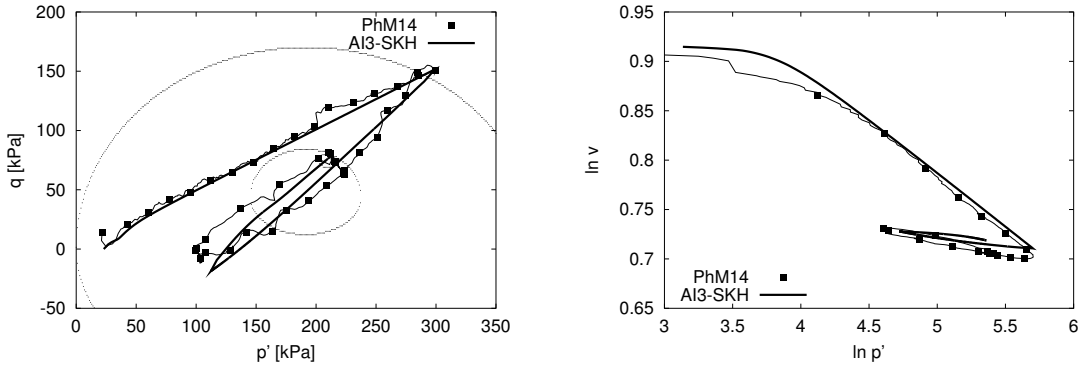

Figure 8.2: *K_0 test PhM14 simulated by the AI3-SKH model*

It may be seen that as well as K_0 loading stress state, the AI3-SKH model is capable of predicting also the K_0 unloading and reloading stress state and volumetric conditions. The predicted specific volume at the end of K_0 compression is very slightly higher than the observed one. This may be attributed to the scatter in the position of the K_{0NC} line for different tests, as indicated if Fig. 7.7, and to the fact that the position of the K_{0NC} line is in the AI3–SKH model calculated from the fitted intercept N, which specifies the position of the isotropic normal compression line (Fig. 7.6). Very close predicted and observed K_{0NC} line reveals that the elliptic shape of the state boundary surface, together with the flow rule assumed, is in this case suitable to predict the position of the K_{0NC} line.

8.2.2 Shear tests

Five shear tests, in which measurements by local strain transducers are available, have been simulated. Two of the tests were performed on specimens of sedimented soil (PhM17 and PhM18) and three on reconstituted soil (PhM14, PhM19 and PhM21). The sensitivity framework has been applied to model the sedimented specimens. All model parameters, except the value of sensitivity S_t, are equal for reconstituted and sedimented soil. Sensitivity S_t is constant (the structure is stable) since the beginning of the stress history of the sedimented specimens. In simulations sizes of *bounding surfaces*, defined as cross–sections of the state boundary surfaces and elastic walls, of sedimented and reconstituted specimens are *equal*. Predictions are however different when plotted in normalised graphs (Fig. 8.3), because reconstituted and sedimented specimens have *different* sizes of the *state boundary surfaces*, defined in $\boldsymbol{\sigma} : v$ space.

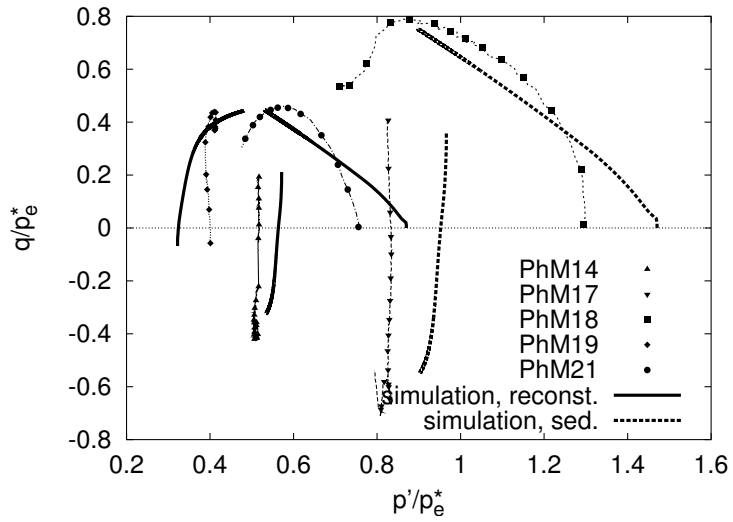

Figure 8.3: *Shear stages of tests simulated and predictions by the AI3-SKH model*

The stress paths of all tests simulated, normalized with respect to p_e^*, are shown in Fig. 8.3. It may be concluded that:

- Although the simulated state before shear does not correspond exactly to the initial state in the experiment, it is situated in the normalised graph (Fig. 8.3) close to the measured initial state. As the position of the initial point in the normalised graph is influenced by both the initial stress state and the initial specific volume, the AI3-SKH model is capable in predicting the K_0 history of reconstituted and sedimented specimens. The difference is caused by small discrepancies in the predicted K_0 stress

state (see Fig. 8.2 left) and $K_0\ p' : v$ state (Fig. 8.2 right).

- The model obviously does not predict strain–softening at the end of tests PhM18 and PhM21, caused by the strain–localisation into the shear bands, but the shape, direction and size of the normalised stress paths is in good agreement with the experimental data.

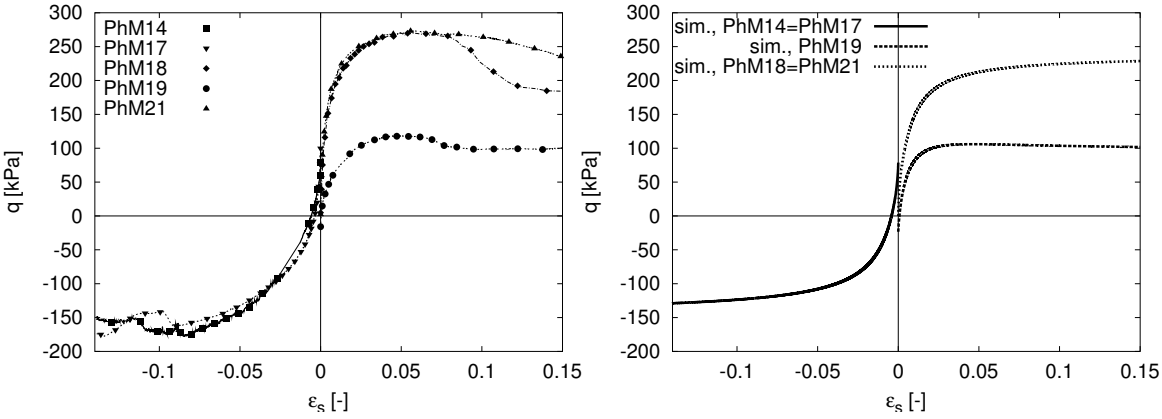

Figure 8.4: *Shear stages of tests simulated, q:ϵ_s curves*

Stress–strain curves of simulated tests are given in Figure 8.4. In the simulation of the tests PhM18 and PhM14 the maximum value of the deviatoric stress q is slightly underpredicted, the stiffness degradation is too fast. The trend in the stiffness degradation and maximum deviatoric stress of different tests is however predicted correctly.

The behaviour at small to very small strains is reproduced in Figure 8.5. For clarity, only results of tests PhM17, PhM19 and PhM21 are included (for comparison with results of the tests PhM14 and PhM21 see Fig. 7.17). Apart from the sudden decrease of the shear stiffness on the boundary of elastic nucleus, which is a common shortcoming of kinematic hardening models, the trend in the degradation of stiffness at small to very small strains is predicted correctly. The difference in the predicted and measured initial stiffness of the test PhM19 is caused by the fact that the measurements with the local LVDT strain transducers do not correspond exactly to the bender element measurements (see Fig. 7.17 bottom), which were used for the calibration of the elastic shear modulus predicted by the AI3–SKH model. The stiffness of the test PhM19 is however overpredicted also at larger strains, as may be seen from both Fig. 8.5 and Fig. 8.4.

To compare predcitions by the AI3-SKH model with experiment, simulated G has been plotted with respect to experimental G for corresponding values of ϵ_s (Fig. 8.6). This

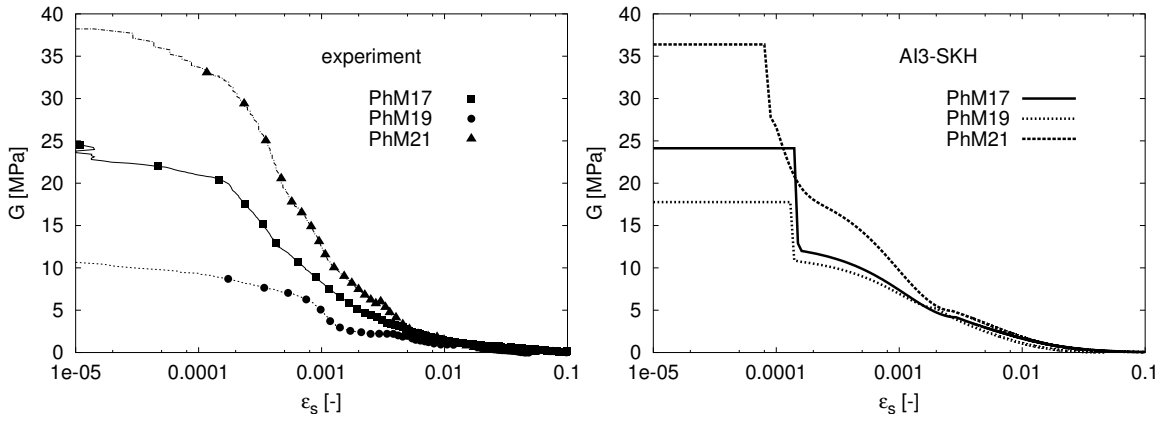

Figure 8.5: *Shear stages of tests simulated, G:ϵ_s curves*

graph emphasizes differences between the experimental data and predictions shown in Fig. 8.5.

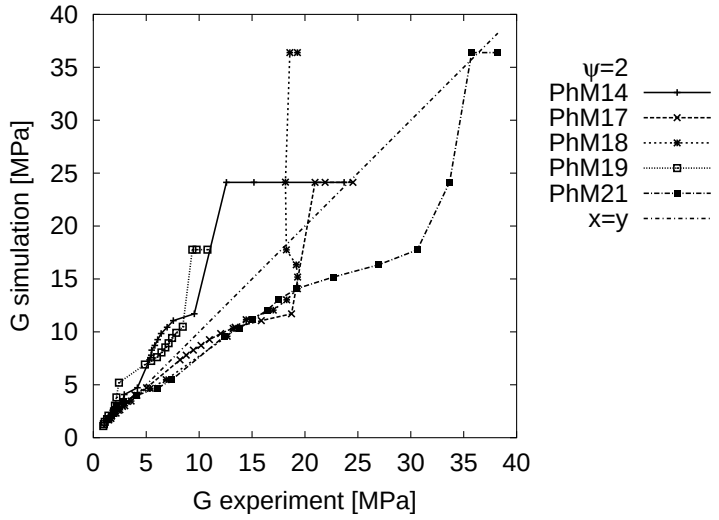

Figure 8.6: *G experimental plotted versus G simulated for corresponding values of ϵ_s*

Finally, the isotropic loading–unloading test PhM13 with two different degrees of stress paths rotation has been simulated (Fig. 8.7). Also here, the AI3-SKH model gives qualitatively and quantitatively reasonable predictions.

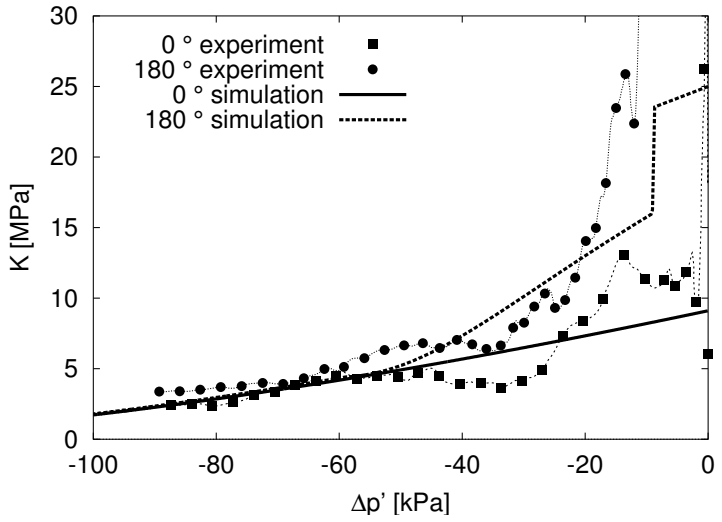

Figure 8.7: *Isotropic loading-unloading test PhM13 with two different degrees of stress paths rotation*

London Clay	G	M	κ	λ	N	S_t
reconst.	5 MPa	0.88	0.066	0.253	3.549	
sed.						1.69

Table 8.3: *Modified Cam–Clay parameters for London Clay*

8.3 Parameters of the Modified Cam–Clay model

In order to compare finite element predictions by the AI3-SKH model and by a basic critical state model (Modified Cam–Clay model), parameters for the Modified Cam–Clay model for London Clay have been evaluated. Parameters N, λ, κ and M correspond to the parameters of the AI3-SKH model (except that coefficients N, λ and κ are defined in semi–logarithmic space) and are summarised in Table 8.3. Parameter G has been identified by means of a parametric study using the large strain behaviour of the shear tests PhM14, PhM17, PhM18, PhM19 and PhM21. As may be seen from Figure 8.8, calibration is very subjective as the Modified Cam–Clay model is not capable of predicting the non–linear behaviour of overconsolidated soil. A value for G of 5MPa has been chosen.

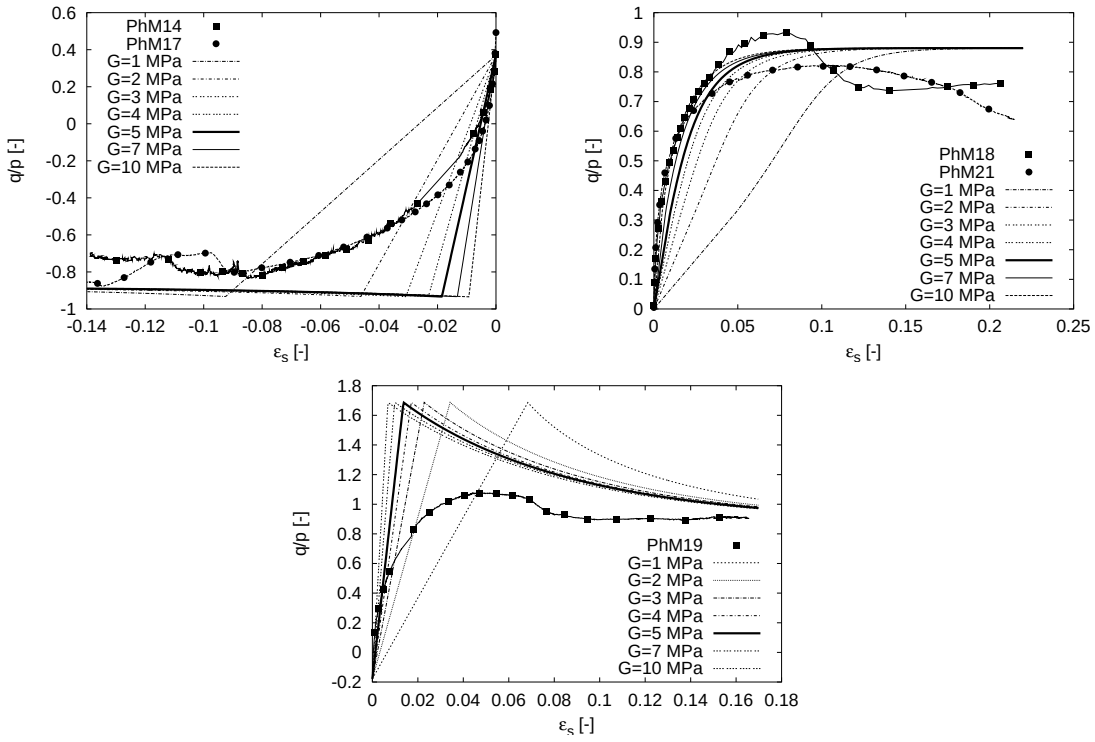

Figure 8.8: *Calibration of the parameter G of the Modified Cam–Clay model*

Chapter 9

Finite Element Modelling of geotechnical structure in natural London Clay

Based on the conclusions from the research described in the previous chapters it is possible to include a section in which the ultimate task of this dissertation is fulfilled: finite element modelling of a geotechnical structure in natural stiff clay, based only on the knowledge of sensitivity and parameters evaluated on the basis of laboratory experiments on reconstituted clays.

The most significant conclusions and achievements of the research, to be used in this chapter, are:

- A suitable constitutive model for the behaviour of *reconstituted* fine grained soil has been developed and evaluated. Particularly, this model is also capable of correctly predicting the K_0 stress state.
- The model has been implemented into a finite element program. It has been demonstrated that inspite of the complicated mathematical structure of the model, accurate time integration is possible. The model and finite element implementation have been evaluated with respect to a boundary value problem in *reconstituted* clay.
- Experimental work has demonstrated the possibility of creating stable sedimentation structure, corresponding to the structure of some natural stiff clays, in the laboratory.
- Laboratory experiments clarified the approach for modelling the geological history

and the structure development in natural clay with *sedimentation* structure.

- It has been shown that it is possible to use the proposed constitutive model, with parameters derived on the basis of experiments on reconstituted specimens, to reproduce the behaviour of clays with sedimentation structure using the sensitivity framework (Cotecchia and Chandler, 2000).

9.1 Heathrow Express trial tunnel

The Heathrow Express trial tunnel, excavated in 1992, has been chosen as a typical tunneling problem in natural London Clay, well instrumented with experimental data available (Deane and Basset, 1995).

The Heathrow Express Rail Link, which provides a 15 minute high speed rail service between Paddington Station in central London and Heathrow Airport, was the first major application of the New Austrian tunneling method (NATM) in London Clay. To study the competence of the NATM to control and limit settlement, which is particularly important when the location of an excavation is directly beneath existing terminal buildings, a trial tunnel was designed.

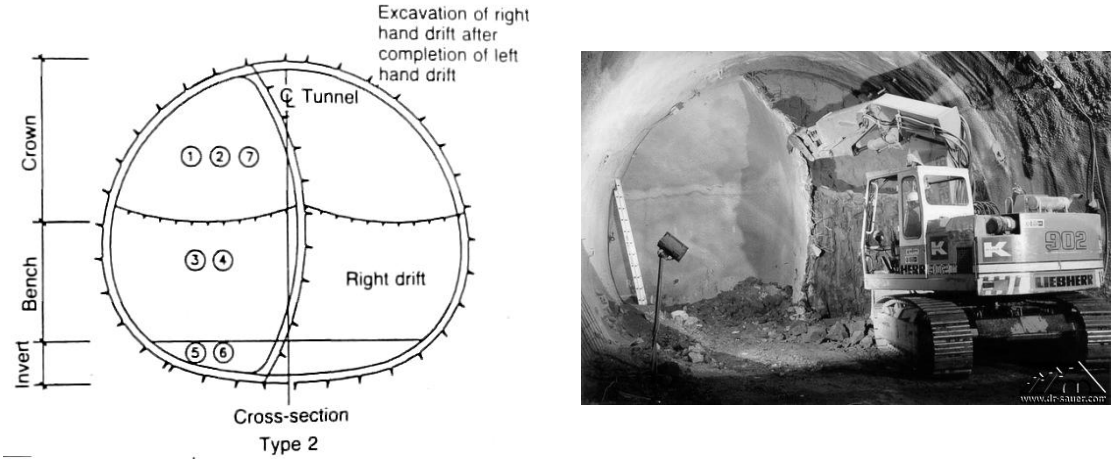

Figure 9.1: *Type 2 excavation sequence at Heathrow Express trial tunnel. Left – Deane and Basset, 1995; Right – Dr.Sauer, 2004.*

The NATM trial tunnel investigated the performance of three different excavation and support sequences. The type 2 sequence has been chosen for finite element modelling. It comprises of:

- Single sidewall drift face excavation.
- Advance per cycle limited to 1 m.
- Left sidewall drift excavated a minimum of 25 m in advance of right sidewall drift.
- Maximum 5 m distance between top heading of sidewall drift and sidewall invert.

The type 2 excavation sequence is shown in Fig. 9.1. The first side heading was excavated in 21 days, followed by the right side heading, excavated in 12 days. The length of a type 2 sequence was 30 metres.

9.2 Finite Element discretization and parameters

To achieve maximum simplicity for the finite element discretization, the tunnel has been modelled to be circular with a diameter of 8.5 m. It is expected that the simplified tunnel cross–section (compare with the actual cross-section shown in Fig. 9.1) does not influence significantly the qualitative pattern of the displacement field further from the tunnel centreline. No comparative analyses with the real cross–section have, however, been performed. The tunnel centreline is 19 m below the surface. The finite element mesh has a depth of 35 m below the surface and spreads 45 m to the right and to the left from the tunnel (due to the excavation sequence chosen, centre–line symmetry may not be applied). Left and right sidewall drifts have been modelled as half–circles.

The finite element mesh is structured and comprises 352 quadratic elements with 385 nodes and 1408 integration points (4 integration points per element). The Lobatto integration method is used. The finite element mesh is shown in Fig. 9.2.

The top 5 m of the zone of interest consists of terrace gravels. A linear elastic perfectly plastic Mohr–Coulomb model has been used to model this material. Parameters from Tang et al. (2000), Powel et al. (1997) and Higgins and Mair (1996) have been adopted. These are given in Table 9.1.

gravel	E [MPa]	ν	ϕ [°]	c [kPa]	ψ [°]	density $[kN/m^3]$
	75	0.25	35	0	17.5	19.6

Table 9.1: Mohr–Coulomb parameters for terrace gravel

Shotcrete lining has been modelled by linear elastic truss–beam elements with parameters after Tang et al. (2000) (Tab. 9.2). No time–dependency of parameters (ageing of

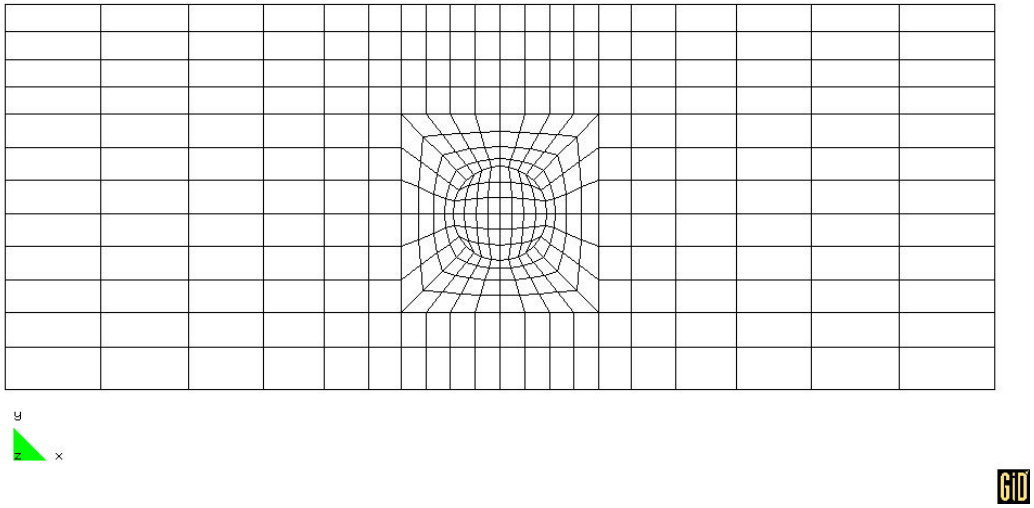

Figure 9.2: *FE mesh adopted: structured, 352 elements, 385 nodes, 1408 int. points*

shotcrete) has been adopted.

lining	E [MPa]	thickness [m]	density $[kN/m^3]$
	30000	0.25	24

Table 9.2: Parameters of shotcrete lining

The London Clay has been modelled both by the AI3-SKH model and by the Modified Cam–Clay model with parameters evaluated in Chapter 8. Isotropic permeability has been assumed (Addenbrooke and Potts, 1996; Potts et al., 1997). Additional parameters for London Clay are summarised in Tab. 9.3.

London Clay	density $[kN/m^3]$	k $[m/s^2]$
	17	10^{-10}

Table 9.3: Additional parameters of London Clay

The phreatic level has been modelled 5 m below the surface.

9.3 Modelling the geological history

To achieve the correct initial state in the ground for simulation of the tunnel excavation, the whole geological history of a London Clay stratum has been modelled. As reviewed in Section 7.1, the geological history consists of:

- K_0 loading along the K_0 normal compression line up to $\sigma_{ax} = 1500$ kPa at the current surface (corresponds to the sedimentation of a London Clay massive).
- K_0 unloading up to $\sigma_{ax} = 0$ kPa at the current surface (corresponds to the erosion of the upper layers of London Clay)
- K_0 reloading of the surface up to $\sigma_{ax} = 100$ kPa (sedimentation of a terrace gravel).

As revealed by laboratory experiments, the sensitivity of stiff clays with stable sedimentation structure is constant and present since the sedimentation of the clay in marine conditions. In other words, the virgin K_0 loading proceeds along the K_0 normal compression line defined by the parameter N and sensitivity S_t. As reviewed in Section 7.1 the sensitivity and/or stability of structure may be influenced by the chemistry of a pore water, in the case of London Clay by leaching of a salt from soil pores. The influence of pore water chemistry is however significantly dependent on the soil mineralogy. Laboratory experiments performed on London Clay show (Sec. 7) that this influence is not significant for London Clay.

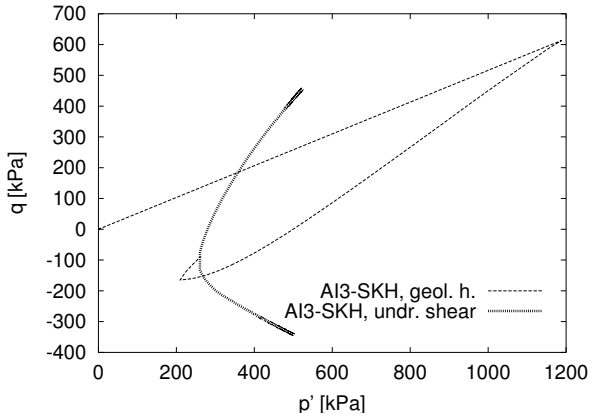

Figure 9.3: *Geological history of a London Clay massive as modelled by the AI3-SKH model*

Therefore, for the present numerical modelling, all stages of simulations (including K_0 virgin loading) have been performed with constant sensitivity S_t. The actual sensitivity of

natural London Clay has been used ($S_t = 2$, Sec. 7.1), instead of the measured sensitivity from the sedimented specimens ($S_t = 1.69$). The sensitivity could have been increased in the ground by time–dependent effects over geological periods, but this phenomenon has not been modelled.

The geological history has been modelled as drained. The stress path of the geological history modelled by the AI3-SKH model at the depth of the tunnel centreline is shown in Fig. 9.3. The stress paths of undrained compression and extension shear tests are also included in the Figure.

After the geological history, the kinematic surfaces have been centered on the current stress state. In this way, a large stiffness in all stress path directions has been regained which models the effects of a long creep period, similarly to Grammatikopoulou et al. (2002), based on experiments by Clayton and Heymann (2001).

9.4 Modelling the NATM construction sequence

The New Austrian tunneling method construction sequence has been modelled in plane–strain. The influence of a tunnel advance was simulated using the method described, e.g., in Wu and Rooney (2001). The method is based on a partial decrease of the nodal forces along the tunnel (corresponds to the state when the tunnel face advances towards the cross–section of interest), generation of lining and decrease of the nodal forces along the tunnel to zero (the tunnel face is beyond the cross–section of interest). A shortcoming of this method is that the actual nodal–force reduction when the lining is generated may be calibrated only on the basis of a full 3D finite element analysis. Such an analysis was not performed due to large CPU requirements, a typical value of a 50% reduction in nodal forces was assumed. This uncertainty may cause quantitative differences in the predicted and observed settlements, it however does not influence significantly qualitative characteristics, such as a shape of the settlement trough.

Coupled material–ground water flow analysis (Biot, 1941) was used, therefore it was necessary to ensure that the real time required for excavation of the trial tunnel was used in the simulations. The simulation sequence was as follows:

1. Decrease nodal forces along the left drift to 50 % in 15 days
2. Generate lining of the left drift
3. Finish excavation of the left drift in 6 days
4. Decrease stresses along the right drift to 50 % in 6 days

5. Generate lining of the right drift
6. Delete middle lining in 3 days
7. Finish excavation of the right drift in 3 days

This sequence is based on the actual construction sequence of the type 2 excavation described in Deane and Basset (1995). The kinematic boundary conditions consist of a fixed base of the mesh and zero displacement in the horizontal direction on the left and right boundary. Along these boundaries are also prescribed drainage conditions, specified by a zero ground water velocity in the horizontal direction on the left and right boundary and zero velocity in the vertical direction at the bottom of the mesh. The tunnel lining has been assumed to be impermeable. The phreatic level is a boundary of zero pore–water pressure.

9.5 Results of analyses

Three analyses are compared:

1. Simulation by the AI3-SKH model with a constant sensitivity for the natural London Clay ($S_t = 2$).
2. Simulation by the AI3-SKH model with $S_t = 1$.
3. Simulation by the Modified Cam–Clay model with $S_t = 2$.

Comparison of the first two simulations should clarify the importance of the application of the sensitivity framework to model the behaviour of geotechnical structures in natural clay. Comparison of the first and the third analysis demonstrates the importance of using an advanced constitutive model, which take into account non–linearity of soil behaviour, for numerical modelling of complicated boundary value problem.

For all the analyses, initial conditions simulated by the AI3-SKH model with $S_t = 2$ (Sec. 9.3) were used. In the second analysis, the size of the bounding surface was decreased by a factor S_t in all elements prior the onset of the excavation stage.

Calculation results were compared with field data at three stages:

1. When the lining of the left drift was generated in the simulation (in the field event the tunnel face of the left drift is in the middle of the type 2 sequence).
2. When the excavation of the left drift was finished.

3. The end of excavation.

9.5.1 Surface settlement against time

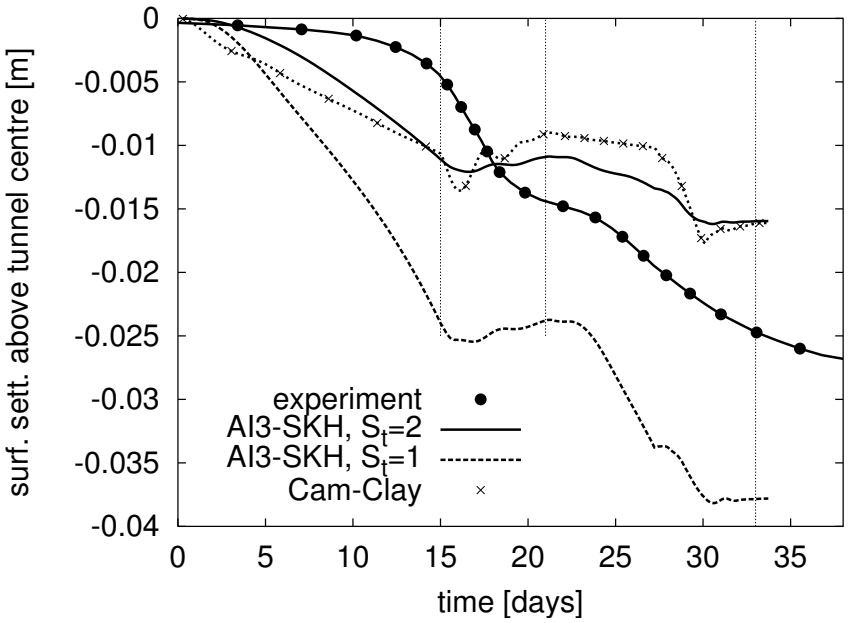

Figure 9.4: *Surface settlement against time (experimental data after Deane and Basset, 1995)*

A graph of the surface settlement above the tunnel centreline with respect to the time measured from the beginning of the type 2 excavation is shown in Figure 9.4. It may be seen that the Modified Cam–Clay model, which is not capable of predicting the non–linearity of soil behaviour and a large quasi–elastic shear stiffness, predicts settlement from the very beginning of excavation. In the field the soil at the beginning of the excavation is stiff, with only small vertical movements.

Using the AI3-SKH model with sensitivity equal to that of the natural London Clay improves the predictions in the range 0-5 days from the beginning of the excavation, although the settlement is in the range approximately 5-10 days still greater than the measured in the field. The same trend was observed when the centrifuge model test of a tunnel in reconstituted clay was simulated (Chapter 5). On the other hand, the increase in settlements predicted by the AI3–SKH model with $S_t = 2$ in the range 20-35 days, i.e. after the tunnel lining was closed, is smaller than the settlements measured in the field in this time range. As commented in section 9.4, the predicted settlements can not be compared

exactly with the field data due to the uncertainty in the plain–strain simplification of the NATM. Fig. 9.4 however clearly shows that the trend in the settlement–time graph is predicted significantly better by both analyses by the AI3–SKH model, than by the Modified Cam–Clay model. The letter predicts unrealistic surface heave in the range 15–20 days, which is attributed to the elastic unloading after the closure of lining. Although this heave is present also in both analyses by the AI3–SKH model, it is less significant when compared to the analysis by the Modified Cam–Clay model.

9.5.2 The shape of the surface settlement trough

The shape of the predicted surface settlement trough compared with the experimental data is shown for the three stages defined in the previous section in Fig. 9.5. It may be seen that:

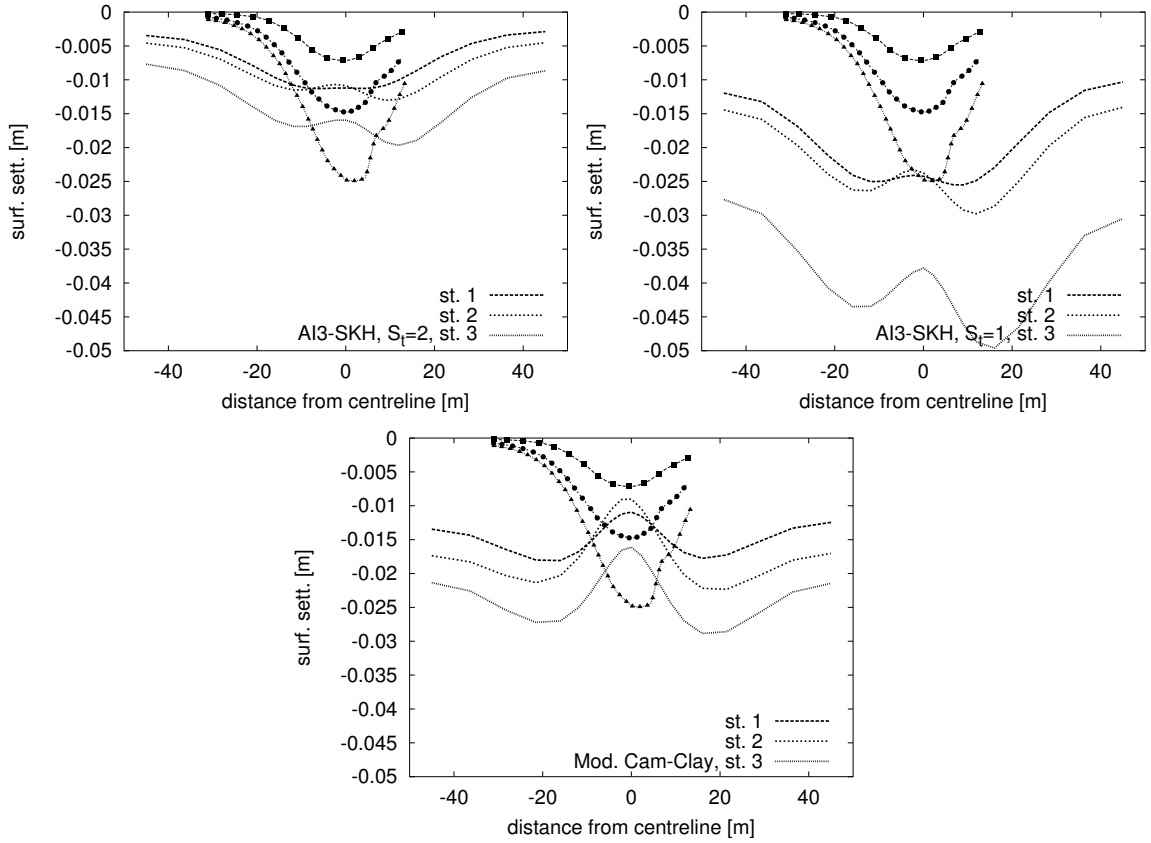

Figure 9.5: *Surface settlement trough compared with the experimental data (experimental data after Deane and Basset, 1995)*

- The shape of the settlement trough predicted by the modified Cam–Clay model is unrealistic, with the smallest settlement above the tunnel centreline! Such a shape of a predicted settlement trough has been observed also by other researchers, for constitutive models which do not take into account non–linearity of soil behaviour when $K_0 > 1$ conditions apply (e.g., Clayton et al., 2003).

- The AI3-SKH model with sensitivity of reconstituted clay ($S_t = 1$) slightly improves the shape of the surface settlement trough when compared to the Modified Cam–Clay model, but the overall magnitude of the settlement is overpredicted. A significant qualitative difference between the predicted and field data is in large vertical settlements predicted by the AI3–SKH model with $S_t = 1$ close to the two vertical boundaries of the finite element mesh.

- The AI3-SKH model with sensitivity of a natural clay ($S_t = 2$) still predicts a significantly wider settlement trough than is observed in the experiment. The trough has however more realistic shape than the trough predicted by the Modified Cam–Clay model and also by the AI3–SKH model with $S_t = 1$. It has been concluded by many authors that the finite element method predicts unrealistically wide settlement trough, even for constitutive models which take into account degradation of stiffness at small to very small strains (e.g., Addenbrooke et al., 1997; Grammatikopoulou at al., 2002; Grant et al., 1996).

9.5.3 Horizontal movements

Horizontal deformations measured 6.3 m from the tunnel centreline are compared with experimental data in Fig. 9.6. Note that the experimental data are from the type 3 excavation (horizontal division), data for type 2 excavation are not available. Data from type 3 excavation are however sufficient for qualitative comparison.

Similarly to the vertical movements, the AI3-SKH model with $S_t = 1$ significantly overpredicts horizontal movements. Unlike the vertical movements however, horizontal movements are overpredicted also by the simulation by the Modified Cam–Clay model. The AI3-SKH model with $S_t = 2$ gives predictions which are closest to the field observation.

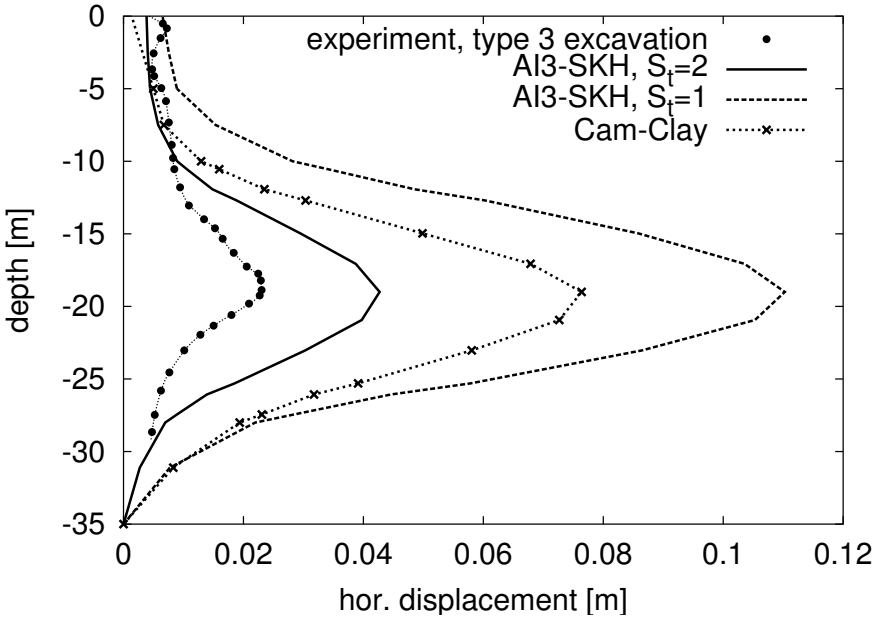

Figure 9.6: *Horizontal deformations depending on a depth measured 6.3 m from the tunnel centreline (experimental data after Deane and Basset, 1995)*

Chapter 10

Summary and conclusions

The main aim of the research presented in the dissertation is the improvement of the predictions of geotechnical structures in natural clays. Because the behaviour of natural clays is very complex, the present work is strongly based on the previous research. The dissertation deals with specific topics, which were found during previous research problematic.

It is necessary to know correctly the initial conditions in the clay stratum before simulation of a geotechnical event. Advanced constitutive model provides an opportunity to assign the initial conditions by the simulation of geological history of the clay deposit, as discussed by Ingram (2000). For this purpose, the constitutive model used must be capable of predicting the K_0 stress state correctly. As incorrect predictions of the K_0 stress state are a known shortcoming of the reference constitutive model (3–SKH model, Stallebrass (1990)), the first part of the dissertation deals with the modification of this model.

Further, the important question raised by the previous research was how the structure in natural clay, which influences significantly the clay behaviour, develops. As a direct study of this problem by means of investigation of natural clay is difficult, specimens of clay with sedimentation structure were prepared under controlled conditions in the laboratory. A detailed experimental comparison of artificial structured clay and reconstituted clay is presented in the next part of the dissertation. Critical evaluation of experimental data provides insight into the way how the sedimentation structure develops in nature, it also demonstrates that it is possible to use parameters of the constitutive model evaluated on the basis of tests on reconstituted clay for the modelling of natural structured clays, provided the constitutive model enhanced by the sensitivity framework is used.

Finally, it is demonstrated how the achievements of the present research may be used to improve predictions of a geotechnical problem in natural structured clays.

Summary and the most important conclusions from the research presented in the dissertation are as follows:

- The review of available experimental evidence has shown that the shape of the state boundary surface is similar for isotropically and K_0 consolidated clays, if it is defined by normalisation with respect to specific volume. If the state boundary surface is defined by the bilinear method then the shape is apparently rotated in the direction of the K_{0NC} line. The shape of the state boundary surface in the octahedral plane is much closer to the Mohr–Coulomb failure criterion than to the shape obtained assuming a constant coefficient of friction, M. The direction of a strain increment vector in triaxial compression is different compared to the direction predicted by the associated flow rule (experiments show a smaller ratio of shear to volumetric strains). Experimental evidence also confirms a radial strain increment in the octahedral plane.

- A new constitutive model, developed as a modification of the 3–SKH model (Stallebrass, 1990), has been proposed. The new model (AI3–SKH) does not introduce any additional model parameters. The main features of the new constitutive model are:

  - Modified flow rule, which enables accurate prediction of stress states under proportional anisotropic compression (importantly K_0 compression).
  - Modified shape of the state boundary surface, with Matsuoka–Nakai–like cross–section in octahedral plane

  The modified model has been evaluated with respect to single element tests on K_0 compressed reconstituted clays and an improvement in predictions, compared to the reference model, has been demonstrated.

- The new and reference constitutive models have been implemented into a finite element program *Tochnog*. Attention has been given to ensure and to demonstrate the accuracy of finite element simulations. A boundary value problem in reconstituted K_0 consolidated clay (centrifuge model test) has been simulated and it has been shown that the new model also improves predictions of boundary value problems.

- Available experimental data on artificially prepared structured clays has been reviewed. Significant factors which influence the structure developed have been defined and studied. The most important are clay mineralogy, chemistry of the pore water and sedimentation. In general, sedimentation causes a more open structure. The structure is more open if the pore water chemistry causes flocculation of particles than if it causes clay particles to be dispersed. In some cases the structure prepared

has been stable, in some cases unstable. The clays with a mineralogy common to most natural clays (mixture of illite, kaolinite and montmorillonite with illite being the dominant mineral) show the consistent behaviour outlined above. Nevertheless, this behaviour may be different for clays of less common mineralogical composition.

- The experimental study comprised laboratory tests on K_0 compressed specimens reconstituted in distilled and salt water and equivalent clay artificially sedimented in salt water. The structure of the sedimented clay is more open than the structure of the reconstituted clay and over the stress range applied the structure is stable. Laboratory experiments were devised to provide a comprehensive picture about the soil behaviour, both in the very small and large strain range, in order to allow detailed evaluation of the new constitutive model. The stress–strain behaviour and the shear–volumetric behaviour (demonstrated indirectly using graphs of the stress paths normalised with respect to specific volume and stress–strain curves) does not differ significantly for sedimented and reconstituted specimens. The chemistry of the pore water does not influence the behaviour and the structure of reconstituted specimens significantly.

- AI3-SKH parameters for the London Clay have been derived. The laboratory experiments have been simulated using these experiments, with the application of the sensitivity framework for sedimented specimens. Although discrepancies between the predicted and observed behaviour occured, the predictions by the AI3–SKH model were in a reasonable agreement with experimental data, for a large range of strains and different stress histories (specimens at different overconsolidation ratios).

- Finally, the achievements of the research allowed to fulfill the main aim of the project, which is modelling of the behaviour of a geotechnical structure in a natural clay using parameters evaluated on the basis of laboratory experiments on reconstituted clay. The Heathrow Express trial tunnel has been chosen as a typical and well instrumented geotechnical problem in natural London Clay. The AI3-SKH model has been used as a basic model, enhanced by the sensitivity framework. Laboratory experiments clarified the way to model the development of natural sedimentation structure and this enabled modelling of the geological history of a London Clay stratum. It has been shown that predictions by the AI3-SKH model with the sensitivity of natural London Clay are significantly closer to field observation than predictions by the Modified Cam–Clay model and the AI3-SKH model with the sensitivity of a reconstituted clay.

References

Abbo, A. J. and Sloan, S. W. (1996). An automatic load stepping algorithm with error control. *International Journal for Numerical Methods in Engineering* **39**, 1737–1759.

Addenbrooke, T., Potts, D., and Puzrin, A. (1997). The influence of pre-failure soil stiffness on the numerical analysis of tunnel construction.. *Géotechnique* **47**, No. 3, 693–712.

Addenbrooke, T. I. and Potts, D. M. (1996). Twin tunnel construction - ground movements and lining behaviour. Mair and Taylor (eds.), *Geotechnical Aspects of Underground Construction in Soft Ground*, pp 441–446. A.A.Balkema, Rotterdam.

Agah, S. (1996). The measurement of soil stiffness using bender elements. *Master's thesis*, City University, London.

Al Tabbaa, A. and Wood, D. M. (1989). An experimentally based "bubble" model for clay. *Proc. 3^{th} Int. Conf. on Numerical Models in Geomechanics*. Niagara Falls.

Anandarajah, a. and Daffalias, Y. F. (1986). Bounding surface plasticity. III: Application to anisotropic cohesive soils. *Journal of Engineering Mechanics ASCE* **112**, No. 12, 1292–1318.

Anson, R. W. W. and Hawkins, A. B. (1998). The effect of calcium ions in pore water on the residual shear strength of kaolinite and sodium montmorillonite. *Géotechnique* **48**, No. 6, 787–800.

Argyris, J. H. (1974). Recent development in the finite element analysis of pressure container reactor vessel. *Nuclear Engineering and Design* **28**, 42–75.

Argyrou, C. A. (1992). The behaviour of clay soils at high pressures. *Master's thesis*, City University, London.

Atkinson, J. H. (1973). *The deformation of undisturbed London Clay. Ph.D. thesis*, University of London.

Atkinson, J. H. (1984). *Rates of loading in drained and undrained stress path and triaxial tests*. Technical report, City University, GERC, Ref. No. GE/84/1.

Atkinson, J. H., Richardson, D., and Stallebrass, S. E. (1990). Effects of recent stress history on the stiffness of over–consolidated soil. *Géotechnique* **40**, No. 4, 531–540.

Banerjee, P. K. and Yousif, N. B. (1986). A plasticity model for the mechanical behaviour of anisotropically consolidated clays. *International Journal for Numerical and Analytical Methods in Geomechanics* **10**, 521–541.

Bardet, J. P. (1990). Lode dependences for isotropic pressure-sensitive elastoplastic materials. *Journal of Applied Mechanics* **57**, 498–506.

Baudet, B. A. (2001). *Modelling effects of structure in soft natural clays. Ph.D. thesis*, City University, London.

Baudet, B. A. and Stallebrass, S. E. (2001). Modelling the destructuration of soft natural soil. Deasi (ed.), *Computer methods and advances in geomechnics*, pp 297–301. A.A.Balkema, Rotterdam.

Baudet, B. A. and Stallebrass, S. E. (2004). A constitutive model for structured clays. *Géotechnique* **54**, No. 4, 269–278.

Been, K. and Sills, G. C. (1981). Self–weight consolidation of soft soils: an experimental and theoretical study. *Géotechnique* **31**, No. 4, 519–535.

Biot, M. A. (1941). General theory of three–dimmensional consolidation. *Journal of Applied Physics* **12**, 155–164.

Bishop, A. W. and Wesley, L. D. (1975). A hydraulic triaxial apparatus for controlled stress path testing. *Géotechnique* **25**, No. 4, 657–670.

Bjerrum, L. and Rosenqvist, I. T. (1956). Some experiments with artificially sedimented clays. *Géotechnique* **6**, 124–136.

Bromhead, E. N. (1978). Large landslides in London Clay at Herne Bay, Kent. *Quarterly Journal of Engineering Geology* **11**, No. 4, 291–304.

Brooker, E. W. and Ireland, H. O. (1965). Earth pressure at rest related to stress history. *Canadian Geotechnical Journal* **2**, No. 1, 1–15.

Burland, J. B. (1990). On the compressibility and shear strength of natural clays. *Géotechnique* **40**, No. 3, 329–378.

Burnett, A. D. and Fookes, P. G. (1974). A regional engineering geological study of the London Clay in the London and Hampshire basins. *Quarterly Journal of Engineering Geology* **7**, No. 3, 257–295.

Callisto, L. (1996). *Studio sperimentale su un'argilla naturale: il comportamento meccanico dell'argilla di Pisa. Ph.D. thesis*, Universita La Sapienza, Roma.

Callisto, L. and Calabresi, G. (1998). Mechanical behaviour of a natural soft clay. *Géotechnique* **48**, No. 4, 495–513.

Callisto, L. and Rampello, S. (2002). Shear strength and small–strain stiffness of a natural clay under general stress conditions. *Géotechnique* **52**, No. 8, 547–560.

Campanella, R. G. and Vaid, Y. P. (1972). A simple K_0 triaxial cell. *Canadian Geotechnical*

Journal **9**, No. 3, 249–260.

Chandler, R. J. (1966). The measurement of rezidual strength in triaxial compression. *Géotechnique* **16**, No. 3, 181–186.

Chandler, R. J., Willis, M. R., Hamilton, P. S., and Andreou, I. (1998). Tectonic shear zones in the London Clay Formation. *Géotechnique* **48**, No. 2, 257–270.

CIMNE (2002). *GiD, The personal pre and post processor*. International Centre for Numerical Methods in Engineering (CIMNE), http://gid.cimne.upc.es.

Clausen, C. J. F., Graham, J., and Wood, D. M. (1984). Yielding in soft clay at mastemyr, norway. *Géotechnique* **34**, No. 4, 581–600.

Clayton, C., Thomas, A., and van der Berg, P. (2003). SCL tunnel design in soft ground - insights from monitoring and numerical modelling. Kolymbas (ed.), *Rational Tunneling, Innsbruck*, pp 61–92. Logos, Berlin.

Clayton, C. R. I. and Heymann, G. (2001). Stiffness of geomaterials at very small strains. *Géotechnique* **51**, No. 3, 245–255.

Coop, M. R. (2002). *Personal communication*. University of London.

Coop, M. R., Atkinson, J. H., and Taylor, R. N. (1995). Strength and stiffness of structured and unstructured soils. *Proc.* 9^{th} *ECSMFE*, Vol. 1, pp 55–62.

Cotecchia, F. (1996). *The effects of structure on the properties of an Italian Pleistocene clay. Ph.D. thesis*, University of London.

Cotecchia, F. and Chandler, J. (1997). The influence of structure on the pre–failure behaviour of a natural clay. *Géotechnique* **47**, No. 3, 523–544.

Cotecchia, F. and Chandler, J. (2000). A general framework for the mechanical behaviour of clays. *Géotechnique* **50**, No. 4, 431–447.

Crisfield, M. A. (1997). *Non–linear Finite Element Analysis of Solids and Structures. Volume I: Essentials*. Wiley: Chichester.

Crooks, J. H. A. and Graham, J. (1976). Geotechnical properties of the belfast estuarine deposits. *Géotechnique* **26**, No. 2, 293–315.

Cuccovillo, T. and Coop, M. R. (1997). The measurement of local axial strains in tiaxial tests using LVDT's. *Géotechnique* **47**, No. 1, 167–171.

Daffalias, Y. F. and Hermann, L. R. (1986). Bounding surface plasticity. II: Application to isotropic cohesive soils. *Journal of Engineering Mechanics ASCE* **112**, No. 12, 1263–1291.

Davies, M. C. R. and Newson, T. A. (1993). A critical state constitutive model for anisotropic soil. G. T. Houlsby and A. N. Schofield (eds.), *Predictive Soil Mechanics*, pp 219–229. London: Thomas Telford.

Deane, A. P. and Basset, R. H. (1995). The heathrow express trial tunnel. *Proc. Instn.*

Civil Engineers **113**, 144–156.

Dr.Sauer (2004). *Dr.Sauer Group website*. http://dr-sauer.com.

Edge, M. J. and Sills, G. C. (1989). The development of layered sediment beds in the laboratory as an illustration of possible field processes. *Quarterly Journal of Engineering Geology* **22**, 271–279.

Eekelen, H. A. M. (1980). Isotropic yield surface in three dimensions for use in soil mechanics. *International Journal for Numerical and Analytical Methods in Geomechanics* **4**, 89–101.

Gajo, A. and Wood, M. D. (2001). A new approach to anisotropic, bounding surface plasticity: general formulation and simulations of natural and reconstituted clay behaviour. *International Journal for Numerical and Analytical Methods in Geomechanics* **25**, 207–241.

Graham, J., Crooks, J. H. A., and Lau, S. L. K. (1988). Yield envelopes: identification and geometric properties. *Géotechnique* **38**, No. 1, 125–134.

Graham, J. and Houlsby, G. T. (1983). Anisotropic elasticity of a natural clay. *Géotechnique* **33**, No. 2, 165–180.

Graham, J., Noonan, M. L., and Lew, K. V. (1983). Yield stress and strain relationship in a natural plastic clay. *Canadian Geotechnical Journal* **20**, 502–516.

Grammatikopoulou, A., Zdravković, L., and Potts, D. M. (2002). The behaviour of 'bubble' models in tunneling problems. *Proc. 2^{nd} Int. Conference on Soil Structure Interaction in Urban Civil Engineering, Zürich.*

Grant, R. J. (1998). *Movements around a tunnel in two–layer ground. Ph.D. thesis*, City University, London.

Grant, R. J., Stallebrass, S. E., and Taylor, R. N. (1996). Prediction of pre-failure ground movements: Physical and numerical techniques. *Proc. 14^{th} Int. Conf. Soil Mechanics and Foundation Engineering*, pp 663–668. Balkema Rotterdam.

Grant, R. J., Stallebrass, S. E., and Taylor, R. N. (1996). Prediction of pre-failure ground movements: Physical and numerical techniques. *Proc. 14^{th} Int. Conf. Soil Mechanics and Foundation Engineering*, pp 663–668. Balkema Rotterdam.

Greening, P. D. and Nash, D. F. T. (2003). Frequency domain determinantion of G_0 using bender elements. *Journal of Geotechnical Testing ASCE* p. submitted for publication.

Hashiguchi, K. (2002). A proposal of the simplest convex–conical surface for soils. *Soils and Foundations* **42**, No. 3, 107–113.

Herle, I. (2001). *Introduction to the mathematical modelling in geomechanics (in Czech).* Charles University, Prague.

Higgins, K. G. and Mair, R. J. (1996). Numerical modelling of the influence of the West-

minster Station excavation and tunnelling on the Big Ben clock tower. Mair and Taylor (eds.), *Geotechnical Aspects of Underground Construction in Soft Ground*, pp 525–530. A.A.Balkema, Rotterdam.

Horseman, S. T., Winter, M. G., and Entwistle, D. C. (1987). *Geotechnical characterisation of Boom Clay in relation to disposal of radioactive waste*. Technical report, Luxembourg: Office for official publications of the European communities.

Ingram, P. J. (2000). *The applicaton of numerical models to natural stiff clays. Ph.D. thesis*, City University, London.

Jakobsen, K. P. and Lade, P. V. (2002). Implementation algorithm for a single hardening constitutive model for frictional materials. *International Journal for Numerical and Analytical Methods in Geomechanics* **26**, 661–681.

Jáky, J. (1944). The coefficient of earth pressure at rest. *Journal for Society of Hungarian Architects and Engineers* pp 355–357.

Jáky, J. (1948). Pressures in silos. *Proc.* 2^{nd} *Int. Conf. Soil Mechanics*, Vol. 1, pp 103–107. Rotterdam.

Jardine, R. J., Symes, M. J., and Burland, J. B. (1984). The measurement of soil stiffness in the triaxial apparatus. *Géotechnique* **34**, No. 3, 323–340.

Jovičić, V. (1997). *The measurement and interpretation of small strain stiffness of soil. Ph.D. thesis*, City University, London.

Kainourgiaki, G. (2002). Development of artificial structure in clays. *Proc.* 7^{th} *Young Geot. Eng. Symp.* University of Dundee.

Karstunen, M., Wheeler, S., and Näätänen, A. (2001). Simulations of soft clay behaviour with S-CLAY1 and MCC. Desai et al. (ed.), *Computer Methods and Advances in Geomechnics*, pp 325–328. Balkema, Rotterdam.

Kirkgard, M. M. and Lade, P. V. (1993). Anisotropic three–dimmensional behaviour of a normally consolidated clay. *Canadian Geotechnical Journal* **30**, 848–858.

Ladd, C. C., Foott, R., Ishihara, K., Schlosser, F., and Poulos, H. G. (1977). Stress-deformation and strength characteristics. *Proc. of the* 9^{th} *Int. Conf. on Soil Mech. and Found. Eng.*, Vol. 2, pp 421–494. Tokyo, Japan.

Lade, P. V. (1977). Elasto–plastic stress–strain theory for cohesionless soil with curved yield surface. *International Journal of Solids and Structures* **13**, 1019–1035.

Lade, P. V. and Duncan, J. M. (1975). Elastoplastic stress–strain theory for cohesionless soil. *Journal of Geotechnical Engineering Division ASCE* **101**, 1037–1053.

Leroueil, S., Tavenas, F., and Locat, J. (1985). Discussion: Correlations between index tests and the properties of remoulded clays. W. D. Carrier III and J. F. Beckman. *Géotechnique* **35**, No. 2, 223–226.

Leroueil, S. and Vaugham, P. R. (1990). The important and congruent effects of structure in natural soils and weak rocks. *Géotechnique* **40**, No. 3, 467–488.

Lin, F. B. and Bažant, Z. P. (1986). Convexity of smooth yield surface of frictional material. *Journal of Engineering Mechanics ASCE* **112**, No. 11, 1259–1262.

Locat, J. and Lefebvre, G. (1985). The compressibility and sensitivity of an artificially sedimented clay soil: The Grande–Baleine marine clay, Québec, Canada. *Marine Geotechnology* **6**, No. 1, 1–28.

Locat, J. and Lefebvre, G. (1986). The origin of structuration of the Grande-Baleine marine sediments, Québec, Canada. *Quarterly Journal of Engineering Geology* **19**, 365–374.

Matsuoka, H. and Nakai, T. (1974). Stress–deformation and strength characteristics of soil under three different principal stresses. *Proc. Japanese Soc. of Civil Engineers*, Vol. 232, pp 59–70.

Mayne, P. W. and Kulhawy, F. H. (1982). K_0–OCR relationships in soil. *Proc. ASCE J. Geotech. Eng. Div.*, Vol. 108, pp 851–872.

Mitchell, R. J. (1970). On the yielding and mechanical strength of Leda clays. *Canadian Geotechnical Journal* **7**, 297–312.

Monte, J. L. and Krizek, R. J. (1976). One–dimmensional mathematical model for large–strain consolidation. *Géotechnique* **26**, No. 3, 495–510.

Mróz, Z., Norris, V. A., and Zienkiewicz, O. C. (1979). Application of an anisotropic hardening model in the analysis of elasto-plastic deformation of soil. *Géotechnique* **29**, No. 1, 1–34.

Nakai, T., Matsuoka, H., Okuno, N., and Tsuzuki, K. (1986). True triaxial tests on normally consolidated clay and analysis of the observed shear behaviour using elastoplastic constitutive models. *Soils and Foundations* **26**, 67–78.

Navaneethan, T. and Sivakumar, V. (2002). Influence of preparation techniques on the index properties of clay. *Geotechnical Engineering, Proc. Inst. Civil. Eng., London* **155**, No. 4, 253–258.

Olson, R. E. (1962). The shear strength properties of calcium illite. *Géotechnique* **12**, 23–43.

Parry, R. H. G. and Nadarajah, V. (1973). A volumetric yield locus for lightly overconsolidated clay. *Géotechnique* **23**, No. 3, 450–453.

Pearce, J. A. (1970). *The behaviour of soft clay in a new true triaxial apparatus. Ph.D. thesis*, University of Cambridge.

Pickles, A. R. (1989). *The application of critical state soil mechanics to predict ground deformations below an embankment constructed on soft alluvium. Ph.D. thesis*, City University, London.

Potts, D. M. and Gens, A. (1985). A critical assessment of methods of correcting for drift from yield surface in elasto-plastic finite element analysis. *International Journal for Numerical and Analytical Methods in Geomechanics* **9**, 149–159.

Potts, D. M., Kovacevic, N., and Vaughan, P. R. (1997). Delayed collapse of cut slopes in stiff clays. *Géotechnique* **47**, No. 5, 953–982.

Powell, D. B., Sigl, O., and Beveridge, J. P. (1997). Heathrow express: The design and performance of the platform tunnels at terminal 4. *Tunneling '97*, pp 565–593. Institution of Mining and Metalurgy, London.

Rampello, S. and Callisto, L. (1998). A study on the subsoil of the tower of pisa based on results from standard and high–quality samples. *Canadian Geotechnical Journal* **35**, No. 6, 1074–1092.

Richardson, D. (1988). *Investigation of treshold effects in soil mechanics. Ph.D. thesis*, City University, London.

Rodemann, D. (1998). *TOCHNOG user's manual.* http://tochnog.sourceforge.net.

Roscoe, K. H. and Burland, J. B. (1968). On the generalised stress-strain behaviour of wet clay. J. Heyman and F. A. Leckie (eds.), *Engineering Plasticity*, pp 535–609. Cambridge: Cambridge Univesrity Press.

Rouiana, M. and Muir Wood, D. (2001). Implicit numerical integration for a kinematic hardening soil plasticity model. *International Journal for Numerical and Analytical Methods in Geomechanics* **25**, 1305–1325.

Schmidt, B. (1966). discussion of 'Earth pressure at rest related to stress history'. *Canadian Geotechnical Journal* **3**, No. 4, 239–242.

Schofield, A. N. and Wroth, C. P. (1968). *Critical state soil mechanics.* McGraw-Hill Book Co., London.

Shibata, T. and Karube, D. (1965). Influence of the variation of the intermediate principal stress on the mechanical properties of normally consolidated clays. *Proc. of the* 6^{th} *Int. Conf. on Soil Mech. and Found. Eng., Montréal*, Vol. 1, pp 359–363. University of Toronto Press, Toronto.

Sides, G. and Barden, L. (1971). The microstructure of dispersed and flocculated samples of kaolinite, illite and montmorillonite. *Canadian Geotechnical Journal* **8**, 391–399.

Sills, G. C. (2002). *Personal communication.* University of Oxford.

Skempton, A. W. (1954). The pore–pressure coefficients A and B. *Géotechnique* **4**, 143–147.

Skempton, A. W. (1970). The consolidation of clays by gravitational compaction. *Q. J. Geological Soc.* **125**, 373–411.

Skempton, A. W. and LaRochelle, P. (1965). The Bradwell slip: A short term failure in London Clay. *Géotechnique* **15**, No. 3, 221–242.

Skempton, A. W., Schuster, R. L., and Petley, D. J. (1969). Joints and fissures in the London Clay at Wraysbury and Edgware. *Géotechnique* **19**, No. 2, 205–217.

Sloan, S. W. (1987). Substepping schemes for the numerical integration of elasto–plastic stress–strain relations. *International Journal for Numerical Methods in Engineering* **24**, 893–911.

Sloan, S. W. and Randolph, M. F. (1982). Numerical predictions of collapse loads using finite elements method. *International Journal for Numerical and Analytical Methods in Geomechanics* **6**, 47–76.

Smart, P. (1969). Soil structure in the electron microscope. *Proc. Int. Conf. Structure. Solid Mech. Eng. Des. Civil Eng. Mater.* University of Southampton, Southampton, England.

Stallebrass, S. E. (1990). *Modelling the efects of recent stress history on the behaviour of overconsolidated soils. Ph.D. thesis*, City University, London.

Stallebrass, S. E. (1992). *Final report for SERC postdoctoral fellowship.* Technical report, City University, GERC, Ref. No. B/90/RFH/8970.

Stallebrass, S. E. and Taylor, R. N. (1997). Prediction of ground movements in overconsolidated clay. *Géotechnique* **47**, No. 2, 235–253.

Tang, D. K. W., Lee, K. M., and Ng, C. W. W. (2000). Stress paths around 3-D numerically simulated NATM tunnel in stiff clay. Fujita and Miyazaki (eds.), *Geotechnical Aspects of Underground Construction in Soft Ground*, pp 443–449. A.A.Balkema, Rotterdam.

Tavenas, F., Des Rosiers, J. P., Leroueil, S., La Rochelle, P., and Roy, M. (1979). The use of strain energy as a yield and creep criterion for lightly overconsolidated clays. *Géotechnique* **29**, No. 3, 285–303.

Tavenas, F. and Leroueil, S. (1977). Effect of stresses and time on yielding of clays. *Proc. of the* 9^{th} *Int. Conf. on Soil Mech. and Found. Eng.*, Vol. 1, pp 319–326. Tokyo, Japan.

Ting, C. M. R., Sills, G. C., and Wijeyesekera, D. C. (1994). Development of K_0 in soft soils. *Géotechnique* **44**, No. 1, 101–109.

Uddin, M. K. and Buensuceso, B. R. (2002). Lime treated clay: salient engineering properties and a conceptual model. *Soils and Foundations* **42**, No. 5, 79–89.

Vaid, Y. P. and Campanella, R. G. (1974). Triaxial and plane strain behaviour of natural clay. *Journal of Geotechnical Engineering Division ASCE* **100**, No. GT3, 207–224.

Viggiani, G. (1992). *Small Strain Stiffness of Fine Grained Soil. Ph.D. thesis*, City University, London.

Viggiani, G. and Atkinson, J. H. (1995). Stiffness of fine–grained soil at very small strains. *Géotechnique* **45**, No. 2, 245–265.

Viggiani, G. and Stallebrass, S. E. (1994). *Shear test data for reconstituted London clay.*

Technical report, City University, GERC, Ref. No. GE/94/04.

Ward, W. H., Marsland, A., and Samuels, S. G. (1965). Properties of the London Clay at the Ashford Common shaft: in–situ and undrained strength tests. *Géotechnique* **15**, No. 4, 321–344.

Ward, W. H., Samuels, S. G., and Butler, M. E. (1959). Further studies of the properties of London Clay. *Géotechnique* **9**, No. 2, 33–58.

Webb, D. L. (1964). *The mechanical properties of undisturbed samples of London Clay. Ph.D. thesis*, University of London, Imperial College of Science, Technology and Medicine.

Wheeler, S. J. (1997). A rotational hardening elasto-plastic model for clays. *Proc.* 14^{th} *ICSMFE, Hamburg*, pp 431–434.

Whittle, A. J. (1993). Evaluation of a constitutive model for overconsolidated clay. *Géotechnique* **43**, No. 2, 289–313.

William, K. J. and Warnkle, E. P. (1975). Constitutive model for the triaxial behaviour of concrete. *International Association for Bridge and Structure Engineering Proceedings, Bergamo, Italy*, Vol. 19.

Wissman, J. W. and Hauck, C. (1983). Efficient elastic–plastic finite element analysis with higher order stress point algorithms. *Comp. Struct.* **17**, 89–95.

Wood, D. M. (1974). *Some aspects of the Mechanical Behaviour of Kaolin under Truly Triaxial Conditions of Stress and Strain. Ph.D. thesis*, University of Cambridge.

Wu, T. H., Loh, A. K., and Malvern, L. E. (1963). Study of failure envelope of soils. *Journal of the Soil Mechanics and Foundations Division ASCE* **89**, No. 1, 145–181.

Wu, W. and Rooney, P. O. (2001). The role of numerical analysis in tunnel design. Kolymbas (ed.), *Tunneling Mechanics, Innsbruck*, pp 88–168. Logos, Berlin.

Yong, R. N. and McKyes, E. (1967). Yielding of clay in a complex stress field. *Proc. of the* 3^{rd} *PanAmerican Conference on Soil Mechanics and Foundation Engineering, Caracas, Venezuela*, Vol. 1, pp 131–143. Sociedad Venezolana de Mecanica del suelo e Ingenieria de Fundaciones, Caracas.

Zeniou, E. A. (1993). The behaviour of boom clay under K_0 compression and shearing. *Master's thesis*, City University, London.